Schottky Nanodiodes Based on Zinc Oxide Thin Films

by

Mei Shen

A thesis submitted in partial fulfillment of the requirements for the degree of

Doctor of Philosophy

in

Solid State Electronics

Department of Electrical and Computer Engineering

University of Alberta

Abstract

The unique advantages like low temperature processing with device-level quality and high transparency give ZnO an edge over other semiconductors and extremely attractive for flexible and transparent electronic applications and hybrid circuits integration on sensors. Currently, reliable and reproducible p-type ZnO remains the most daunting obstacle strangling the development of junction devices based on this material system. To enable functional devices applications including UV photodetector, power diode in rectifier circuits like RFID, metal semiconductor field effect transistors (MESFET), source-gated thin film transistor (SGTFT), *etc.*, rectifying Schottky contacts to ZnO have been intensively studied for decades. Many considerable progresses have been achieved in producing of ZnO Schottky contacts on bulk ZnO. However, for many applications, reliable high quality Schottky contacts on ultra-thin polycrystalline ZnO active layer are required. The ultra-thin active layer is beneficial to reduce the turn-on series resistance and promote the flexibility of the devices.

Most of the reported metal/ZnO thin film Schottky diodes, particularly for those with an active layer getting down to 100 nm, suffered from large levels of extraneous traps which lead to poor rectifying behavior, low Schottky barrier height and large ideality factor. Numerous fabrication methods and interface pretreatments have been attempted to produce high performance diodes with low defects, high Schottky barrier, low ideality factor and subsequently high rectifying behavior. In the work presented in this dissertation, a novel low temperature plasma-enhanced atomic layer deposition (PEALD) technique with *in situ* plasma surface pretreatment has demonstrated its feasibility to produce high-performance vertical Schottky nanodiodes with 30 nm thick ZnO active layer grown at near room temperature (50 °C). The best

diode achieved in this work demonstrated remarkable room temperature performance with rectifying ratio of ~10^6, effective barrier height values of 0.76±0.014 eV, ideality factor values of 1.140±0.007, series resistance down to 90 Ω at 1V and breakdown field of at least 1.67 MV/cm.

To optimize the fabrication conditions, a series of devices with various ZnO deposition temperatures down to 50 °C and pretreatment and different bottom electrodes were fabricated and characterized by material study and electrical study. The material characterizations showed that the films composition, surface morphology and crystalline structure depended on the ALD recipe and substrate material. The electrical measurements evaluated the electrical performance and indicated the defects level across the Schottky barrier.

The effect of barrier inhomogeneity, which widely existed in metal-oxide semiconductor interface, on the temperature dependent behavior of the diode was observed and attributed to the nanocrystalline nature of the materials and interface defects lying in the bandgap. In addition, we demonstrate an interesting time-related improvement of the Schottky nanodiodes performance, which is potentially important for long-term usage.

Finally, analytical simulations of the diode's current-voltage characteristics were carried out taking into account the other mechanisms like image force lowering and thermionic field emission in the carrier transport. The significant roles of other mechanisms besides thermionic emission were revealed for this specific configuration. We believe the advances achieved in this dissertation are important to the development of ZnO based technology, especially in the fields requiring low synthesis temperature.

Preface

Some of the research conducted for this thesis forms part of a research collaboration between Professor Doug Barlage and Professor Ying Tsui at the Department of Electrical and Computer Engineering and Professor Ken Cadien at the Department of Chemical and Material Engineering at the University of Alberta to develop a suite of devices and circuits with metal oxide semiconductors. The device fabrication referred to chapter 2 was designed and executed by myself, with the assistance of Dr. Amir Afshar and Dr. Triratna P. Muneshwar particularly in the atomic layer deposition part referred to section 2.2. The literature review in chapter 1 and chapter 4, the material characterization in chapter 2, diode characterizations, data analysis and discussion in chapter 5, concluding analysis and discussion for future directions in chapter 5 are my original work, as well as the study with the pulsed laser deposition in Appendix I.

Part of section 5.2 and appendix I has been published as M. Shen, A. Afshar, M. Gupta, G. Shoute, K. Cadien, Y. Y. Tsui and D. Barlage, "Electrical Characteristics of TiW/ZnO Schottky contact with ALD and PLD," *MRS Proc.*, 2014, 1635, pp 127-132. I was responsible for the data collection and analysis as well as the manuscript composition. A. Afshar assisted with the ZnO thin film growth by atomic layer deposition and contributed to manuscript edits. M. Gupta involved with the developing of PLD recipe for ZnO thin film growth. G. Shoute contributed to manuscript edits. K. Cadien, Y. Y. Tsui and D. Barlage were supervisory authors and were involved in the concept formation and contributed to manuscript edits.

Part of section 5.2 has been published as M. Shen, A. Afshar, Y. Y. Tsui, K. Cadien, and D. W. Barlage, "Performance of Nanocrystal ZnO Thin Film Schottky Contacts on Cu by Atomic Layer Deposition*," IEEE Trans. NanotechnolI.*, 2017, 16(1), 135-139. I was responsible

for the data collection and analysis as well as the manuscript composition. A. Afshar assisted with the ZnO thin film growth by atomic layer deposition and contributed to manuscript edits. Y. Y. Tsui, K. Cadien, and D. W. Barlage were supervisory authors and were involved in the concept formation and contributed to manuscript edits.

Part of section 5.3 has been published as M. Shen, T. P. Muneshwar, K. Cadien, Y. Y. Tsui, and D. Barlage, "Optimization of Copper Schottky Contacts on Nanocrystalline ZnO Thin Films by Atomic Layer Deposition," *MRS Adv.*, 2016, 1(50), 3421-3427. I was responsible for the data collection and analysis as well as the manuscript composition. T. P. Muneshwar assisted with the ZnO thin film growth by atomic layer deposition and contributed to manuscript edits. K. Cadien, Y. Y. Tsui, and D. W. Barlage were supervisory authors and were involved in the concept formation and contributed to manuscript edits.

Appendix II of the thesis is part of the overall research collaboration and is included to provide the appropriate context for my work. I was responsible for materials characterizations and contributed to optimizing the Schottky contact formation for maximum device performance.

Acknowledgements

First, I would like to express my deepest appreciation to my academic advisor and co-supervisor Dr. Douglas Barlage for his continually and convincingly encouragement and impartment of a spirit of adventure in regard to research. Without his optimism, insight and in-depth understanding of solid states electronics this dissertation would not have been possible.

I would like to thank my supervisor Dr. Ying Y. Tsui for his guidance and persistent help to mold me into a researcher I am today. His spirit of perseverance and endeavor in work encouraged me throughout the course of my PhD study, especially when I was feeling down.

I would like to thank Professor Karthik Shankar as the member of the supervisory committee. I would also like to thank everyone in the research group for their support: Alex Ma, Debbie Ha, Fatema Chowdhury, Gem Shoute and Mourad Benlamri, not only for the help in study and research but also for being dear friends. I would also like to thank our collaborator Dr. Ken Cadien and his group for their contribution to my project, with special thanks to Amir Afshar, and most of all, Triratna Muneshwar for being a wise advisor and dear friend.

I would also like to thank to China Scholarship Council for their financial support granted through predoctoral fellowship and make this precious journey possible at the initial stage.

Lastly, but not least, I would like to thank my parents for their deeply support in spirit. Special thanks to my dear friends: Feng Tian, Hal Friesen, Lei Sun, etc., for their endless care and help in my life in Canada.

Table of Contents

List of Tables

List of Figures

Chapter 1

Zinc Oxide for Semiconductor Devices

1.1 HISTORIC RESEARCH AND DEVELOPMENT ON ZNO

Since the first semiconductor transistor was invented in 1947, semiconductor industry has grown to be a 312 billion US dollars in 2011 and is expected to grow 5 times larger in 2025 because of the increasing demand for smart media[1]. Si-based devices have continuously dominated the current commercial market in integrated circuits and discrete devices for power switching, computing, communication and data storage. As to optoelectronic and high-speed applications, gallium arsenide (GaAs) became the semiconductor of choice because of its superior optical characteristics and electron transport properties comparing to Si. GaAs is a direct bandgap semiconductor, whereas Si is indirect, hence GaAs is more efficient for optoelectronics application. GaAs also has higher carrier mobility than Si[2], which lead to faster devices. However, with increasing demand for greater power handling, larger frequency, and higher temperature electronics and UV/blue light emitter applications, the performances of Si-based and GaAs-based techniques have approached their theoretical limits of this material and thus they have little room for further improvement. In order to satisfy this increasing demand, it becomes urgent to search for other semiconducting materials and develop their synthesis and processing techniques. Wide bandgap semiconductors have been studied extensively in recent years, because of their inherent material advantages for electronics applications. They have larger energy bandgap, higher thermal conductivity, higher breakdown voltage, and comparable carrier mobility compared to Si and GaAs[3]. Many researchers have put efforts in finding optimum wide

bandgap compound semiconductor materials for power and optical applications[2,4,5]. SiC is expected to be superior to both Si and GaAs in electronic applications[4], and is the most common compound semiconductor material other than Si used in power electronics at the present time. In the past two decades, GaN-based technology has achieved remarkable breakthrough. The development of GaN-based devices has revolutionized many industries including lighting, biotechnology, communication, medicine and imaging[6,7]. ZnO is an emerging wide-gap compound semiconductor material rivaling with GaN and SiC.

Indeed, ZnO is an "old" material appearing since the Bronze Age. It has been used for over hundred years as paint pigment, catalysts[8], cosmetics, lubricant additives, materials in gas sensor[9], materials for transparent conductive electrode[10], materials for piezoelectric devices[11] and materials for varistors[12]. These mature areas led to a fairly large amount of the annual usage of ZnO. As early as 1957, a book entitled "Zinc Oxide Rediscovered" was published by the New Jersey Zinc Company to promote the materials' "frontier" characteristics for semiconducting, catalytic, ferrite, luminescent, photoconductive and photochemical, and other potential applications[13]. At that time, research focused mainly on polycrystalline ZnO growth, characterization and applications. Polycrystalline ZnO was developed and used in surface acoustic wave (SAW) devices owing to large electromechanical coupling, varistors and transparent conductive films (TCO). Later, with the developing of GaN-based technologies, new need for high-quality single crystal ZnO as an alternative substrate for GaN and InGaN epitaxy was proposed originally because of their lattice match. This drove ZnO growth techniques for fabricating large area wafers in both bulk and epitaxial forms to be improved economically and reproducibly[14–16]. The realization of high quality large area ZnO wafer led to potential opportunities of ZnO as a semiconductor device material for a range of applications including

power diodes, field effect transistors, UV light emitting diodes (LEDs), UV photodetectors, transparent conducting oxide (TCO), etc.

1.2 PROPERTIES OF ZINC OXIDE

ZnO has a number of superior properties for electronic and optoelectronic applications. Its electrical parameters are listed in Table 1.1 compared to those of GaN and Si. ZnO has a high melting point of 1975 ºC and an excellent thermal stability. ZnO is an II-VI compound semiconductor with a direct wide bandgap of 3.37 eV at room temperature. Compare to those of GaN, ZnO has a larger exciton binding energy of 60 meV, which will potentially enhance luminescence efficiency for light emitting devices and laser diodes utilizing excitonic transitions. ZnO has a higher saturation velocity while its electron Hall mobility in single crystal at room temperature is slightly lower, both of which are important for device performance. The effects of those intrinsic properties on the electronics devices quality are evaluated by the methods introduced in section 1.3.

Table 1.1 Comparison of electrical properties of ZnO, Si and GaN bulk materials[3,13,18,19,209–213].

Properties	**Si**	**ZnO**	**GaN**
Bandgap at 300 K (eV)	1.12	3.37	3.44
Exciton Binding Energy (meV)	/	60	25
Electron Hall Mobility (cm^2/Vs)*	1500	440	1250
Hole Hall Mobility (cm^2/Vs)*	600	5-50	850
Saturated Electron Velocity (10^7 cm/s)	1.3	3.2	3
Dielectric Constant	11.8	8.9	9
Thermal Conductivity(λ) ($W/m^{-1}K^{-1}$)	1.3	1.16 (40 for sintered ZnO)	2.3

* Carrier Hall mobility values compiled are from reported measurement at room temperature.

Furthermore, ZnO has better radiation resistance for space and harsh environments applications. ZnO is non-toxic and environmental friendly. ZnO has a relatively low-cost native substrate, which is significant for minimal lattice mismatch in developing lasers and LEDs

applications. ZnO is also attractive in quantum well engineering due to its tunable bandgap via divalent substitution on the cation site while still keeping the wurtzite structure. For example, with Mg substitution in ZnO, the bandgap has been increased to ~4.0 eV; a lower bandgap of ~3.0 eV has been achieved with Cd substitution[17].

1.2.1 Crystal Structure of ZnO

ZnO is normally formed in hexagonal (wurtzite) crystalline structure (see Figure 1.1[18]), with lattice parameters a=0.325 nm and c=0.521 nm. Zinc atom locates in the center of tetrahedron, bonding with 4 oxygen atoms on the corner. Since the electronegativity of Zn and O, 1.65 and 3.44 separately, have a large difference, chemical bonding between the atoms are highly ionic, where electrons form d orbit of Zn atoms hybridize with those from p orbit of O atoms. Ideal hexagonal structure shows c/a = 1.633 while ZnO has a ratio of 1.602 slightly off from the ideal wurtzite structure. Consequently, with alternating zinc and oxygen layers stacking on [0001] and [000 $\overline{1}$] direction separately, polar surface is induced on c-axis. This property drives ZnO nanostructure to grow preferably in c-axis orientation.

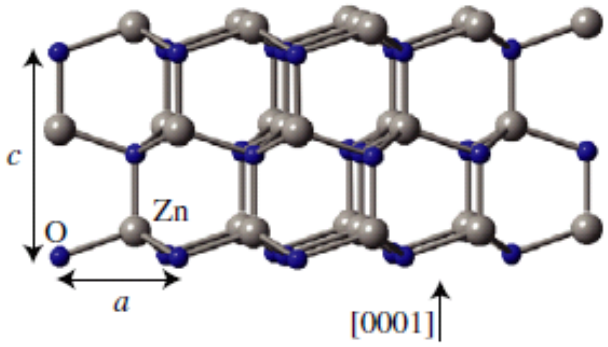

Figure 1.1. ZnO wurtzite crystal structure[18].

1.2.2 Electrical Properties of ZnO

Conductivity in ZnO is extremely defect related and ranges from metallic to insulating. Electrical conduction in unintentionally doped films of these oxides occurs because of intrinsic defects, such as interstitial metal or oxygen vacancies, which donate free electrons. These oxide semiconductors are therefore inherent n-type or electron conductors, and oxide semiconducting films can be engineered with electron carrier concentrations more than 10^{21} cm^{-3} and mobilities greater than 50 $cm^2V^{-1}s^{-1}$ even with polycrystalline or amorphous structure[19–22]. With its high conductivity and high transparency, ZnO would be an alternative to indium tin oxide (ITO) as transparent conducting oxide (TCO), especially important since ITO is facing a potential world-wide shortage with increasing demand for solar cell industry[23,24].

Similar to other wide-bandgap semiconductors, ZnO suffers from doping asymmetry issues since its valence band is relatively far from the vacuum level. Since 1970, significant efforts were made to study doping and implantation of impurities into ZnO. It was found that ZnO is inherently n-type. The p-type conductivity in ZnO is proven to be a difficult challenge till now[25,26]. The first convincing results of well characterized p-type ZnO homoepitaxial films fabricated by molecular beam epitaxy (MBE) were published by Look *et al.* and the advance can potentially lead to realization of *p-n* junction ZnO light emitting diodes (LED)[27]. Other than Look's work, the production of reproducible p-type material is still elusive. In order to controlling the conductivity in ZnO, researchers have put strong efforts to learn the role of native point defects. For a long time, Zn interstitials, O vacancies and Zn antisites have been assumed as the main causes for n-type conductivity[28]. In contrast, recent reports show that this attribution may be wrong. Zn interstitials act as shallow donors but have a high formation enthalpy in n-type

ZnO. Then it is unlikely to contribute to n-type conductivity. When Fermi level (E_f) shifts towards the valence band maximum, the formation energy of Zn interstitials decreases dramatically. This means it is very likely to compensate p-type impurities. Oxygen vacancies are a deep donor and have a low formation enthalpy in p-type material. Hence, it is not responsible for n-type conductivity but it can prevent the achievement of p-type conductivity. Zn antisites are a deep donor as well and have a high formation enthalpy in p-type. Thus it may not be account for either n-type conductivity or compensation center in p-type material[29]. Instead, for as-grow n-type conductivity, the unintentional background hydrogen at interstitial or substitutional sites act as shallow donor and can be responsible for the n-type conductivity[30]. Other impurities such as Ga, In and Al can also form shallow donor centers. On the other hand, there are only few p-type doping candidates for ZnO having been reported including nitrogen, P, As or Sb[4]. Despite a lot of efforts have been made by researchers to solve the doping asymmetry issues, The production of reproducible p-type ZnO remains a formidable challenge for the moment[31], and reproducible homogeneous junctions based on p-type and n-type dopants in ZnO have not been reported to date. The lack of reliable p-type ZnO materials prevents the development of high quality ZnO based homogeneous junction devices.

1.2.3 Optical Properties of ZnO

ZnO optical bandgap is in the range of 3.2 to 3.4 eV. It is transparent to visible light but has a sharp UV cut off at around 380nm in transmission. As a direct bandgap semiconductor, ZnO photoluminescence (PL) processes consisting of electron-hole pair generation excited by photons having energies greater than the ZnO bandgap energy and recombination of excited states to generate emissions centered about 380 nm. However, visible ZnO PL emissions with

green and orange bands centered about 500 nm and 630 nm respectively have also been observed. The visible bands emissions are found to be correlated to intrinsic defects in the grown films with strength dependence on the amount of defects. It is generally accepted that the green bands are related to oxygen depletion and the orange bands are related to excess oxygen[32]. Hence, the PL emissions can be used as indicators for defects levels in the ZnO films.

Since potential optoelectronics applications of ZnO overlap significantly with those of GaN, ZnO is usually regarded as a potential alternate to the more mature GaN material system due to their similar bandgap for device applications, large exciton binding energy, relatively low-cost native substrates, etc. It is given that GaN-based optoelectronic devices are already mature with commercial products available. For example, GaN-based light emitting diodes (LEDs) have gained a large market because they have higher efficiency than even the fluorescent bulbs, and blue lasers are already applied in high-density data storage system. For ZnO, the large exciton binding energy (60 meV) makes it promising for even brighter optical emitters than GaN (25 meV) optoelectronics.

1.3 DEVICE FIGURE OF MERITS

The important parameters including breakdown voltage (V_{BV}), *on* resistance (R_{on}), maximum current density (J_{max}), *off* leakage (I_{off}), and material reliability, are used to evaluate power devices. Since the electrical properties are all related to the fundamental material properties, figure of merits (FOMs) were generated by various researchers based on these relationships, such as Johnson's figure of merit (*JFOM*), Keyes' figure of merit (*KFOM*), Baliga's figure if merit (*BFOM*), and Baliga's high frequency figure of merit (*BHFFOM*). Those

figures of merit provide insights for the evaluation of materials from which devices could be fabricated.

In 1965, Johnson derived a figure of merit to compare the switching capability of semiconductors device which defines the power-frequency product for a low voltage transistor. The tradeoff between the cut-off frequency (f_T) and the maximum allowable voltage-ampere performance are shown to be related to the critical electric field and saturation velocity of the semiconductor as given by[33]

$$JFOM = \left(\frac{E_C v_s}{2\pi}\right)^2 \qquad (1.1)$$

Which suggests that semiconductor with wider band gap would have an edge over narrow band gap semiconductor in switching properties. In 1972, Keyes derived a figure of merit providing a thermal limitation to the switching behavior of transistors used in integrated circuits as given by[34]

$$KFOM = \lambda\left(\frac{c v_s}{4\pi\epsilon}\right)^{1/2} \qquad (1.2)$$

Where λ is the thermal conductivity, c is the velocity of light and ϵ is the dielectric constant of the semiconductor. In 1983, Baliga derived a figure of merit which defines material parameters for minimum conduction losses in high power devices as given by[35]

$$BFOM = \epsilon\mu {E_G}^3 \qquad (1.3)$$

Where μ is the mobility and E_G is the bandgap of the semiconductor. A refinement of *BFOM* taking into account the switching losses in high-frequency systems is given by[36]

$$BHFFOM = \mu {E_C}^2 \qquad (1.4)$$

known as Baliga's high frequency figure of merit (*BHFFOM*). The critical breakdown field E_C is related to the bandgap of the semiconductor as[37]

$$E_C = {E_g}^3 \qquad (1.5)$$

The final relation $BHFFOM=\mu {E_g}^6$ is obtained by substitution of eq 1.5 into eq 1.4. The FOMs for ZnO and GaN, normalized to those of Si, are tabulated in Table 1.2 based on the materials properties listed in Table 1.1.

Table 1.2. Figures of merit for power electronic devices based on material properties listed in Table 1.1.

Properties	**Si**	**ZnO**	**GaN**
$BFOM \sim \epsilon \mu {E_g}^3$	1	6	81
$BHFFOM \sim \mu {E_g}^6$	1	99	700
$JFOM \sim {v_s}^2 {E_g}^6$	1	4497	4471
$KFOM \sim \lambda v_s / \epsilon$	1	3	5

This summarized table of FOMs depicts that high quality crystalline ZnO is promising for high power, high frequency and high temperature device applications significantly outperforming Si and rivaling with GaN due to its large bandgap, high saturation velocity, and good thermal conductivity. The most detrimental property of ZnO is the relatively low mobility. However, in the case of polycrystalline or amorphous thin film based devices, the mobility of oxide semiconductor based on ZnO material has an edge over other available techniques. The mobilities of available polycrystalline and/or amorphous semiconductors are listed and compared in Table 1.3. This advantage makes ZnO extremely attractive for flexible electronics which require lower processing temperature[22,38–40].

Table 1.3. Comparison of mobilities for polycrystalline or amorphous semiconductors[22].

	Oxide semiconductors	Amorphous Si	Low-T poly-Si	Organic semiconductors
Carrier Mobility ($cm^2V^{-1}s^{-1}$)	1-100	1 max	50-100	0.1-10

1.4 ZNO SCHOTTKY CONTACT MOTIVATION

High quality rectifying Schottky contact has been studied extensively and is critical to enable many other applications like UV photodetector, power diode in rectify circuits like RFID, metal semiconductor field effect transistors (MESFET), source-gated thin film transistor, etc[41–47]. Despite the fact that ZnO Schottky contact has been studied since 1965[48], most of the reported metal/ZnO Schottky diodes were leaky leading to poor rectifying behavior and low Schottky barrier height (SBH). Researchers have found that interface states between metal and ZnO contribute tremendously to the formation of Schottky barriers. In addition, the properties of ZnO active layer affect the diode performance like series resistance, breakdown voltage, leakage current, etc[49].

Historical reports of Schottky contacts to n-type ZnO using various metallization materials including Pt, Au, Pd, Ir, conducting polymer PEDOT: PSS, etc. are listed in Table 1.4 with their identical Schottky parameters: effective Schottky barrier height $q\Phi_B$ and ideality factor n, which indicate the rectifying capability of the diode and the impact extent of non-ideal factors on the diode, respectively. The $q\Phi_B$ values were restricted to a range of 0.5-0.9 eV albeit with different metallization materials and large n values were obtained for most of the contacts reported. An ideality factor larger than unity for a diode with negligible series resistance indicates that there are other mechanisms in addition to thermionic emission contributing to the current transport across the Schottky contact.

It was also shown that metallization contacts to ZnO without surface pretreatment exhibited Fermi-level pinning and even ohmic behavior due to the presence of numbers of defects in the forbidden bandgap on ZnO surface[50–55]. In addition, surface accumulation layer induced by hydroxyl adsorbates may hinder the diode rectifying as reported by Coppa *et al*[54]. To

Table 1.4 Schottky contacts to n-type ZnO compiled from literatures.

Description	**Metal**	Φ_B **(eV)**	***n***
[47]n-ZnO single wafer	Spin-coated PEDOT:PSS (Schottky) E-beam Ti/Au (ohmic)	1.1	1.02
[64]n-ZnO single wafer	E-beam Pt, sputtered W (Schottky) E-beam Ti/Al/Pt/Au (ohmic)	0.70, 0.45	1.5, 2
[66]n-ZnO epi on Sappire	E-beam Ir (Schottky) Evaporated Ti/Al/Ti/Au (ohmic)	0.824	1.68
[51] n-ZnO single wafer	E-beam Au (Schottky)	0.5	2
[155]n-ZnO epi on Al/Si	E-beam Au (Schottky) E-beam Al (Ohmic)	0.586	1.5
[156]n-ZnO single wafer	Spin-coated PEDOT:PSS (Schottky) E-beam Ti/Au (ohmic)	0.9	1.2
[67]n-ZnO epi on p-Si Hydrothermal seed layer @ 90 °C; Annealed @ 450 °C	Evaporated Au (top Schottky) Evaporated Al (top ohmic)	0.78	1.84
[68]n-ZnO epi on n-Si	Evaporated Pd (Schottky) Evaporated Ti/Al (ohmic)	0.81	1.46
[69]n-ZnO epi on n-Si	Evaporated Au (Schottky) Evaporated Au–Sb alloy (ohmic)	0.59	1.2
[70]n-ZnO epi on Sappire	Evaporated Pd (Schottky) PLD ZnO:Al seed layer(ohmic)	1.14	1.49
[71]n-ZnO epi on Sappire	Sputtered Pt, Au, Ag and Pd (Schottky) PLD ZnO:Al seed layer(ohmic)	0.66- 0.84	1.25- 1.59
[44]n-ZnO epi on Ag	E-beam Ag (Schottky) E-beam Ti/Au (ohmic)	0.27	2.4
[54]n-ZnO ($000\overline{1}$) wafer	E-beam Au (Schottky) E-beam Ti (ohmic)	0.60- 0.67	1.03- 1.86
[49]n-ZnO epi on glass (0.5-1 um) RF sputtered; Annealed @ 1000 °C	Sputtered Mn Evaporated Au (Schottky)	\	2.7-3.5

reduce the surface defects and remove the adsorbates on the ZnO surface, many surface pretreatment techniques have been proposed, such as hydrogen peroxide treatment[52,53], oxygen plasma treatment[51,56,57], chemical etching[58], etc. The surface treatment processes

have improved the properties of Schottky contact and widely been applied to fabricate high quality Schottky contacts on top of high quality bulk ZnO.

Thermal stability is another important property for ZnO Schottky contacts operating in high temperature environment as well as their long term reliability[59–63]. ZnO Schottky contacts realized with Au and Ag had shown low thermal stability limiting their application[59]. Both Au and Ag Schottky contacts showed degrading properties by heating in vacuum as low as 365 K. Tungsten (W) has a promising thermal stability. In the study by K. Ip, *et al.*[64], W had shown a thermal stability as high as 500 °C for bulk ZnO.

Recent advances in wafer-based high quality ZnO Schottky contacts were reported with a better understanding the physical formation processes.[65] Most of the studies are focused on the formation of Schottky contacts on high quality ZnO (single crystal wafer or thick epitaxial films grown at high processing temperature)[51,62,66–71]. The promising techniques based on ZnO single wafer can rarely surpass the much advanced GaN techniques and limits their applications in the market. While the thin film technologies based on ZnO material system with the advantages of low-temperature processed films with acceptable electrical properties and compatibility with the existing Si industry may seek a path out for this material in the extremely competitive market. For example, integrated circuits applied on microelectromechanical systems (MEMS) sensors, i.e. hybrid integration, usually require low processing temperature technology, since high processing temperature is one of the major concerns to integrate the electrical circuits directly onto microelectromechanical systems (MEMS) sensors like capacitive micro-machined ultrasonic transducers (CMUT) to improve performances[72]. Applications in integrated circuits require embeddable thin film configurations. High quality ultra-thin ZnO film has been demonstrated for ZnO based circuits with high temperature (~700 °C) PLD[73–76] and low temperature ALD[77].

Furthermore, the advantage of low processing temperature expands the variety of suitable substrates and opens the feasibility of transparent ZnO-based flexible electronic applications, since the use of flexible plastic substrates precludes high manufacturing temperature which deforms such substrates[78]. ZnO based flexible electronics are regarded as an emerging technology with revolutionary potential with an enormous market[79]. Although functions relevant to flexible electronics including bending, rolling, folding, and stretching as well as device durability of ZnO-based devices have not been studied extensively. Researchers have shown that devices based on ultrathin ZnO material system have stable performance on flexible substrate and it is as good as that on rigid wafers like Si substrates[80–83].

In this thesis project, the focus is on ZnO Schottky nanodiodes based on low temperature grown polycrystalline ZnO thin films with nanometer-scaled thickness. The low temperature growth of ZnO thin films are achieved by an emerging technique, atomic layer deposition (ALD). Nanodiodes with scaled down active layer thickness principally have reduced series resistance, which is an important factor for RF applications. Devices based on such thin films are potentially feasible for flexible electronics. The unique advantage of low processing temperature is ideal for integrations on any substrates such as flexible plastic, display panel, MEMs chips, etc.

Furthermore, in this project, a bottom Schottky contact configuration is proposed to simplify the fabrication processes. As mentioned above, it has been approved that surface treatment is one of the key factors to produce high quality Schottky contacts on top of bulk ZnO. As to the case of ultrathin ZnO thin films, it is difficult to control the surface treatment process to maintain the consistency of the properties. And also subsequent damage to ZnO may be induced by the surface treatment processes. With bottom Schottky contact configuration, we can avoid surface treatment on the ZnO thin film to prevent damaging ZnO thin film.

A systematic study of various Schottky metallization for the ultrathin polycrystalline ZnO thin film is carried out to explore proper contact material which can give good rectifying behavior and also good thermal stability. The Schottky contact formation mechanisms are explored as well as the current transport mechanisms in the nanodiodes. Although we only demonstrate Schottky nanodiodes fabricated on rigid Si wafer in this thesis, the low temperature processing makes it compatible for flexible substrates like plastic and hybrid integration on sensor chips.

Chapter 2

ZnO Thin Films Synthesis and Device Processing

2.1 INTRODUCTION

The fabrication of ZnO thin film is an essential process step in the utilization of ZnO in modern electronic devices such as LEDs, UV detectors, sensors, thin film transistors (TFTs), surface acoustic wave (SAW) devices. The properties of thin film ZnO grown by a variety of deposition techniques including sputtering[49,81,84,85], sol-gel[86–88], pulsed laser deposition (PLD)[89–92], chemical vapor deposition (CVD)[93,94], molecular-beam epitaxy (MBE)[27,95], and atomic layer deposition (ALD)[23,40,96,97] have been widely investigated. One typical issue with physical vapor deposition (PVD) including PLD and sputtering is the variation of layer thickness over a large surface area which typically depends on the angle between source and substrate normal, while CVD can attain uniform thickness over a large planar surface. The disadvantages with CVD lie in: (i) the production of by-products in growth, and (ii) constricted transport of reactants within high-aspect ratio featured surface of substrate, leading to a non-conformal deposition.

For optoelectronic applications including LEDs and laser diodes, high quality ZnO epitaxial layers are required to obtain good device performance. This can be achieved by RF magnetron sputtering, PLD, MOCVD, and MBE, etc., which allows a fine control over the deposition procedure. Typically, deposition temperature above 300 ºC, postdeposition annealing and the used of substrates with only small lattice mismatch, such as single-crystal Sapphire, GaN, etc., are necessary to get high quality crystalline ZnO films.

For electrical applications including varistors, piezoelectric devices, transparent conductive electrodes for solar cells, gas sensor and TFTs, high quality crystalline ZnO single-crystal thin films are not necessary as acceptable performance can still be attained with polycrystalline ZnO thin film. Polycrystalline ZnO can be grown with low deposition temperature making it extremely attractive for devices on low cost substrates such as plastic, Si and glass. Although dominant carrier scattering at grain boundaries as well as intrinsic defects in ZnO thin film limit its carrier mobility[41], the low deposition temperature is a key advantage making it viable especially for transparent thin film transistors (TFTs) on flexible polymer substrate and hybrid integration on other devices which have low temperature tolerance.

2.2 ATOMIC LAYER DEPOSITION OF ZNO THIN FILMS

2.2.1 Introduction of Atomic Layer Deposition

Atomic layer deposition (ALD) is emerged as an approach to overcome the limitations of PVD and CVD, and provides: (i) uniform deposition of sub-nm thick films over large substrate, (ii) dense films free of defects like pinholes, particulate inclusions, etc., and (iii) uniform coverage over high-aspect ratio featured surface of substrate. It was developed as a variation of conventional CVD technique in which the chemical reactants are individually introduced into the reactor in a cyclic sequence, i.e. for a binary compound reaction,

$$A + B \rightarrow AB$$

The source of A or B element known as precursor is pulsed into the reactor with a sequence of ABABABAB… with inert gas purges between every precursor pulse.

While both CVD and ALD involve surface reactions of the precursors, one advantage of ALD is the self-limiting of the reaction by terminating it on saturation when the active sites are consumed regardless of any excess reactants. This self-limiting nature leads to a uniform deposition of layers over featured substrate surface and potentially yields good coverage for extremely large substrates with sufficient precursor flux to reach surface saturation condition. Furthermore, the inert gas purges between every precursor pulse successfully remove the excess precursor molecules and by products of the reaction, ensuring the grown films are free of contaminations from the by-products incorporated into the reaction and particulate inclusions from gas phase reaction. Furthermore, using highly reactive precursor like plasma, ALD growth can be conducted at very low temperatures[23,96–98]. Due to these excellent natures, ALD ZnO has attracted increasing attention recently[23,40,44,83,99–104].

2.2.2 ZnO Thin Film Growth

The ALD processes for ZnO thin films growth in the work were developed in collaboration with Prof. Ken Cadien's research group. The ALD-150LX reactor from Kurt J. Lesker is schematically depicted in Figure 2.1. With the support of inductively coupled plasma ICP (0.6 kW, 13.56 MHz) equipped in the system, *in-situ* substrate surface plasma treatment (SPT) is performed before deposition to clean the surface-absorbed contaminations and tune the interface chemical bonds. There are two types of ALD processes developed for ZnO thin film growth: (i) thermal ALD (TALD) using deionized water (H_2O: Optima LC/MC, Fisher Scientific, 18 MΩ) and diethylzinc (DEZ) precursors with high purity Ar (5.0 purity, Praxair) as the carrier gas, and (ii) plasma enhanced ALD (PEALD) using inductively-coupled remote oxygen plasma and DEZ precursor with high purity Argon (Ar) as the carrier gas. ZnO films were all deposited

under continuous 100 sccm Ar flow in a cylindrical ALD reactor with a controlled vacuum at 1.0 torr (133.3 Pa) during the deposition.

In the precursor half reactions of TALD, DEZ molecules were discretely pulsed through a three-port diaphragm valve 1 (Swagelok) for duration t_1 into the precursor carrier gas (100 sccm flow of Ar) stream. During reactant reaction step, H_2O molecules were pulsed through a three-port diaphragm valve 2 for duration t_3 into the reactant carrier gas (Ar) stream to introduce O source to react with the absorbed DEZ at the substrate. Between every reactant precursor pulse, the ALD reactor was purged (utilizing continuous 100 sccm Ar flow) for durations t_2 (post-DEZ purge) and t_4 (post-H_2O purge), respectively.

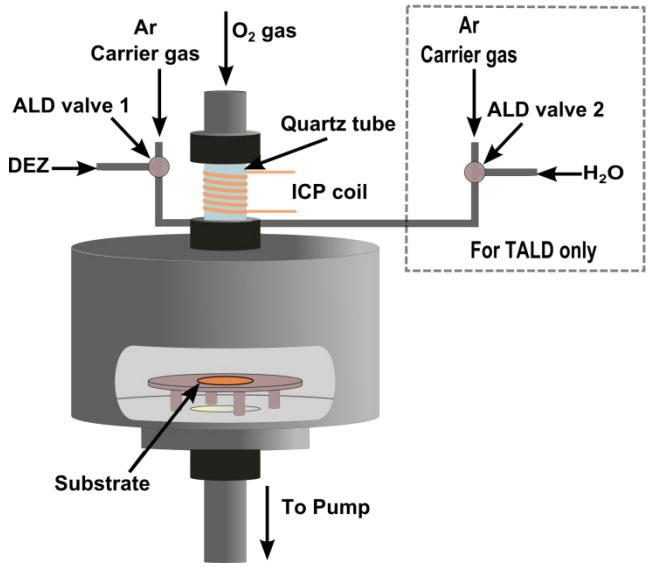

Figure 2.1. The schematic diagram of the ALD chamber. Gas lines in the dash line box are only used for TALD.

In the precursor half reactions of PEALD, DEZ molecules were discretely pulsed through a three-port diaphragm valve 1 (Swagelok) for duration t_1 into the precursor carrier gas (100 sccm flow of Ar) stream. During reactant reaction step, a 60 sccm flow of O_2 was released into the reactant carrier gas (Ar) stream flowing through ignited plasma (0.6kW, remote ICP) for

duration t_3 to introduce active plasma species at the substrate. Following every precursor and plasma exposure step, the ALD reactor was purged (utilizing continuous 100 sccm Ar flow) for durations t_2 (post-DEZ purge) and t_4 (post-plasma purge), respectively.

The cycle sequence for each recipe type is depicted in Figure 2.2 with the duration for each step t_1 — t_2 — t_3 —t_4. The deposition temperature (T_{sub}) as the fifth variable in ALD recipe was controlled by a heater underneath. The ZnO thin film thickness is monitored by an *in-situ* J.A.Woollam M-2000DI spectroscopic ellipsometer (SE). Initially, the optical constants of the ZnO thin films were found by fitting the optical model to the measured data. By assuming that the optical constants are the same during the ALD growth, the thickness of the growing oxide can then be monitored *in situ*.

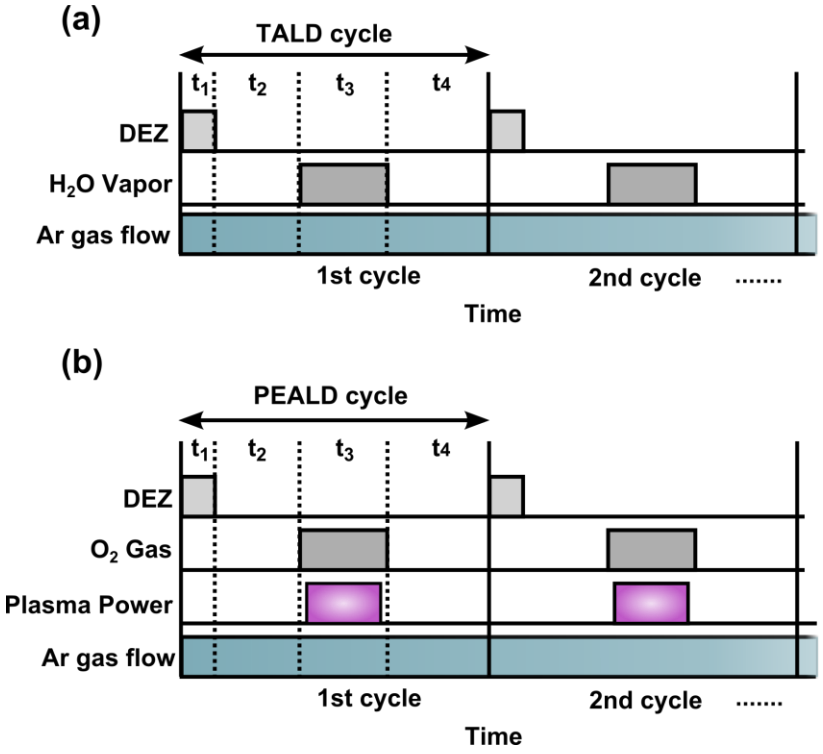

Figure 2.2. The schematic diagrams of (a) TALD cycle and (b) PEALD cycle.

The details of a series of ALD recipes and surface plasma treatments (SPT) conditions used in this work are summarized in Table 2.1. The recipe is named in a format of T (or P)-temperature in ºC, for example, P-200. T and P correspond to TALD and PEALD, respectively. A systematic study of the ALD ZnO was carried out in collaboration with Dr. Amir Afshar. The ALD recipes including T-200, P-200, P-130, P-100, P-200-2, P-200-3, and P-200-4 were determined based on the calibrated saturation curves. The saturation curves indicated: (i) the minimum dose time for saturation of growth rate per cycle (GPC) is 20 ms for DEZ, 0.1 s for H_2O, and 2.0 s for oxygen plasma, (ii) the ALD window for both type of ALD is in the range of 100-200 °C with a maximum GPC at 150 °C. Please refer to Dr. Amir Afshar's thesis in ref.[105] for more details.

Table 2.1 Summarization of ALD recipes.

Recipe	**Cycle Parameters (s)**				**GPC (Å /cycle)**	**T_{sub} (°C)**	**SPT gas Ar:O_2**	**SPT time (s)**
	t_1	t_2	t_3	t_4				
T-200	0.03	5.00	0.50	10.00	1.6	200	100:60	5
P-200	0.03	10.00*	2.00	5.00	1.5	200	100:60	5
P-100	0.03	10.00*	2.00	5.00	1.25	100	100:60	5
P-130	0.03	10.00*	2.00	5.00	1.44	130	100:60	5
P-200-2	0.04	5.00	2.00	2.00	1.444	200	100:60	5
P-200-3	0.04	5.00	2.00	2.00	1.444	200	100:60	15
P-200-4	0.04	5.00	2.00	2.00	1.444	200	100:0	305
P-50	0.06	8.00	5.00	5.00	1.15	50	100:0	10
T-50#	0.04	5.00	0.50	10.00	/	50	/	/

*The purge consists of 2 parts: first 5 s is pure Ar, next 5 s is a mixture of 100:60 Ar:O_2;
#T-50 recipe is only used as a surface treatment before the PEALD deposition, to prevent the metal surface oxidation during deposition.

The recipe of P-50 was developed in collaboration with Dr. Triratna Muneshwar. After exploring a large range of the ALD parameters[96], it showed that a self-limiting trend which is expected for ALD was found in a temperature window of ≤ 50 °C for PEALD while higher

temperature showed suspected non-ALD mode of ALD growth. The minimum dose time for saturation of growth rate per cycle (GPC) is then 60 ms for DEZ and 5.0 s for oxygen plasma.

2.3 FABRICATION OF SCHOTTKY DIODES

The fabrication of Schottky diodes started with p^+-Si <100> wafers (525±20 μm) with a resistivity ρ=10-20 ohm•cm. The Si wafer is pre-cleaned by piranha solutions (H_2SO_4:H_2O_2 3:1 mixture) for 20 min to remove any organic contaminations. After cleaning, Si wafers were put into a MiniBrute furnace which is set to 900 °C to grow 50 nm thermal oxides (SiO_2). The SiO_2/Si substrate pieces were then transferred into a planar magnetron sputter system to deposit ~50 nm thick metal electrodes. The metals include platinum (Pt), gold (Au), nickel (Ni), silver (Ag), copper (Cu) and titanium tungsten (TiW) with 5 nm Ti as the adhesion layer for all of the above metals. The chamber ambient is controlled at 7 mtorr with Ar flow backfilled from a base pressure of 10^{-6} torr. The samples were then transferred to the ALD chamber to grow ZnO thin films as described in section 2.2. During the transferring, the samples were exposed to the atmosphere. After ZnO growth, the top ohmic contacts consisting of Al/Au layer stacks (~120/10 nm thick respectively) were sputtered in a Kurt J. Lesker planar magnetron sputter system from and patterned by conventional lift-off process. Finally, the ZnO thin films, where were not covered by the Al/Au pattern, were removed by wet etching with a commercial Al etchant. The process flow for top ohmic contact fabrication is illustrated Figure 2.3. A top view microscopic image for a single diode is shown in Figure 2.4a and a schematic diagram of the diode cross section of the inside circle area was shown in Figure 2.4b. The fabricated diodes are named in a format of process type (P or T) - process temperature in ºC – and bottom metallization material throughout the thesis, for example, P-200-TiW for the diode shown in Figure 2.4. The probe

configuration for the electrical measurement is also shown in Figure 2.4. The bottom Schottky electrode is connected to the anode and the top ohmic contact is connected to the cathode which is typically set as ground. All the electrical measurements are performed with white overhead lab lights on and microscope light on since the device performance is independent on the lighting condition from observations.

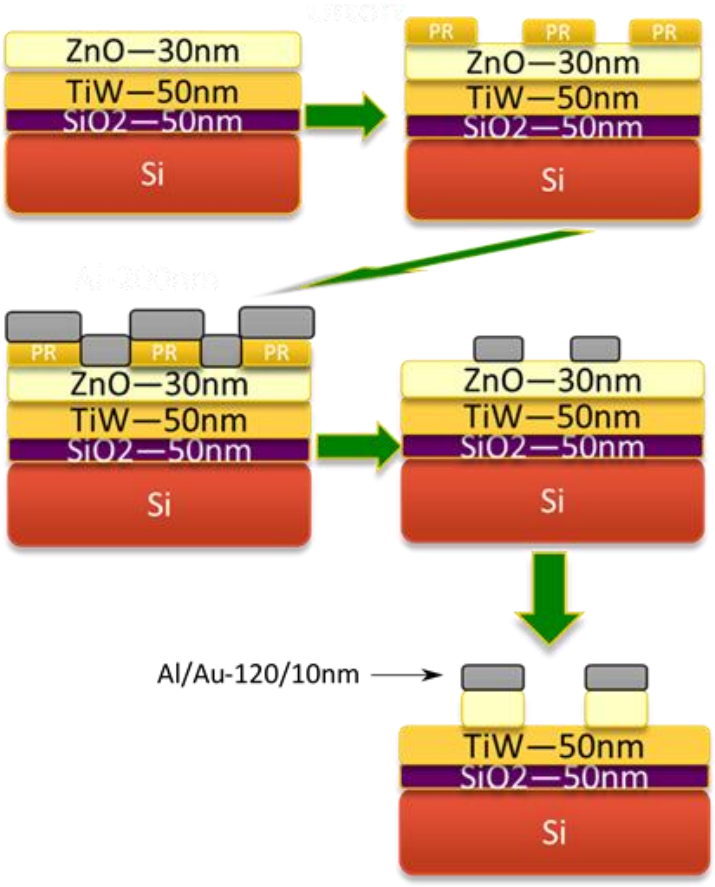

Figure 2.3. Microfabrication process flow of the top ohmic contact for Schottky diode. TiW is used as the bottom Schottky metal for example.

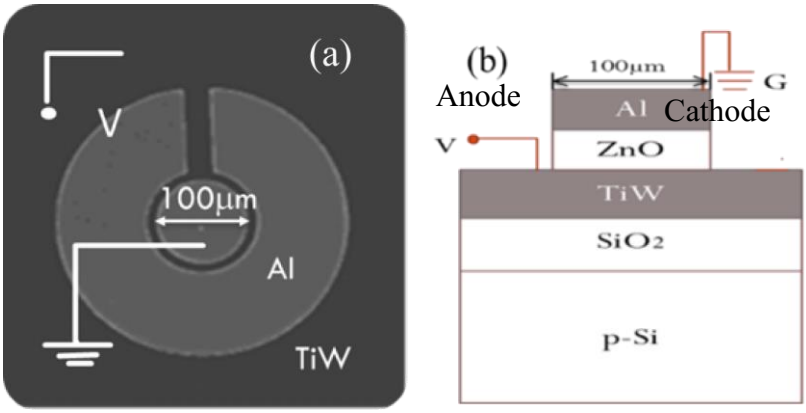

Figure 2.4. (a) A top view microscopic image for a single diode, (b) a schematic diagram for the diode cross section of the inside circle area. TiW is used as the bottom Schottky metal for

Chapter 3

Zinc Oxide Thin Film Characterizations

In the formation of an intimate contact between a metal and a semiconductor, the structural, electrical and chemical natures of the semiconductor are crucial to control the behavior of resulting contact. In this chapter, the techniques used to study the nature of the synthesized ZnO thin films are introduced including field emission scanning electron microscopy (FESEM), atomic force microscopy (AFM), X-ray diffraction (XRD), and X-ray photoemission spectroscopy (XPS).

3.1 FIELD EMISSION SCANNING ELECTRON MICROSCOPY

Field emission scanning electron microscopy (FESEM) generates images from electrons instead of light for conventional optical microscopy. A beam of electron is produced and accelerated from a field-emission cathode in an electron gun. The generated electron beam is then focused onto the sample surface by a series of condenser and objective lenses in a vacuum tube. A scanning coil moves the beam across the sample surface. The electron beam interacts with the sample and produces various types of signals including backscattered electrons, secondary electrons, Auger electrons, characteristic x-rays, etc. The signals, typically secondary electrons signals in standard SEM, are collected by a detector, and amplified and converted to a cathode ray tube image. The contrast in the final image depends on the sample and the equipment setup, providing information on the sample composition, topography and morphology.

Compare to the optical microscopy, the main advantages of using electrons for image formation are high resolution down to 1.5 nm, high magnification up to 500,000X, and large

depth of fields or effective focus range. Compare to the conventional SEM, the FESEM provides narrower probing beams at both low and high electron energy, resulting in improved spatial resolution down to 1.5 nm (three to six times better). Furthermore, the problem of electrical charging of samples can be minimized by low accelerating voltage (in the range of 0.5 to 30 kV), and the low-kinetic-energy resulted from low accelerating voltage reduces penetration depth into the material.

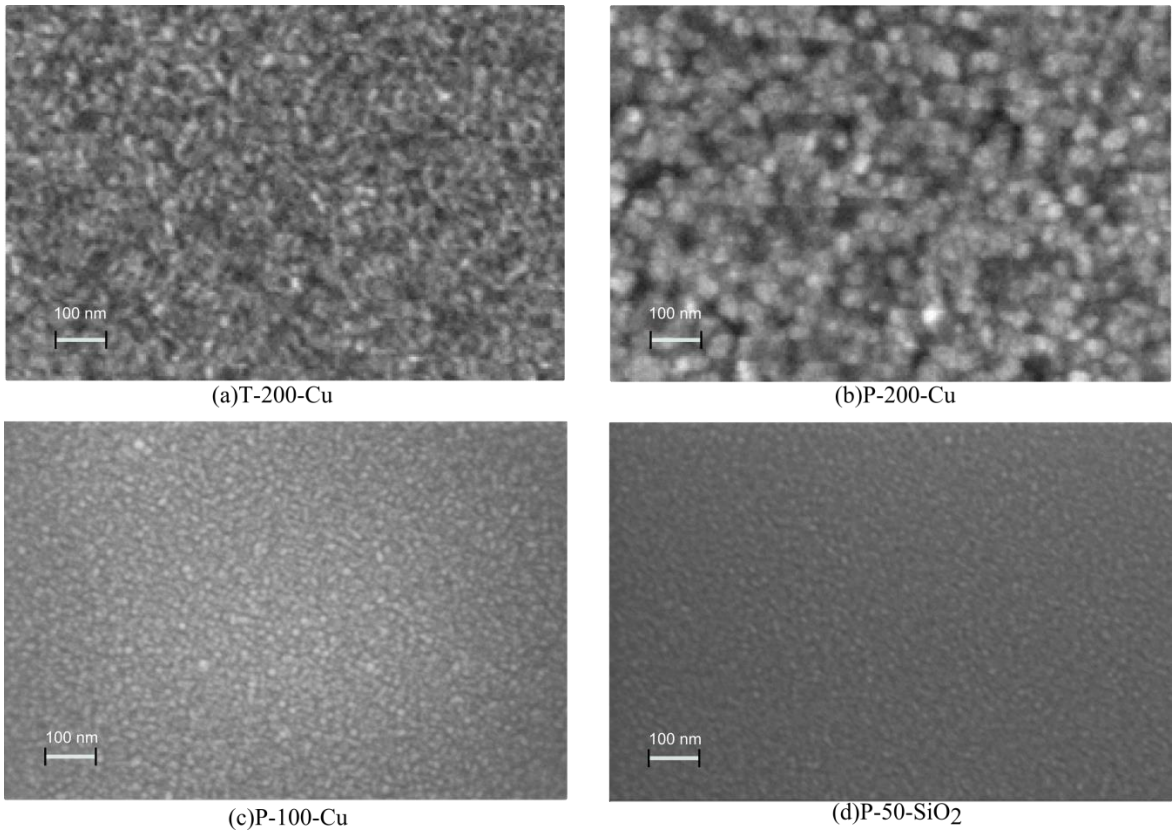

Figure 3.1 SEM image of (a) T-200 ZnO thin film (b) P-200 ZnO thin film (c) P-100 ZnO thin film deposited on Cu substrate; (d) P-50 ZnO thin film deposited on SiO_2 substrate.

A FESEM of model JAMP-9500F (JEOL) was used in this work to study the surface morphology of the ZnO thin films. The samples are named in a format of T (or P)-temperature-substrate. Figure 3.1 shows the high resolution FESEM images for T-200-Cu, P-200-Cu, P-100-Cu and P-50-SiO_2. The T-200-Cu shows a surface feature with mainly elongated shape grains

and mixed with some round shape grains, similar to that reported by Weng *et al*[106]. The P-200-Cu shows more uniform surface features consist of larger round grains with average size ~30 nm. The P-100-Cu also shows smaller round grains. The P-50-SiO_2 shows smoothest surface with the smallest round grain.

3.2 ATOMIC FORCE MICROSCOPY

Atomic force microscopy (AFM) employs a miniature tip on a silicon (or silicon nitride) cantilever that deflects a laser beam depending on surface topography and properties through an interaction between the tip and the surface. The signal is measured with a photodetector, amplified and converted into an image display on a cathode ray tube. Depending on the type of surface, AFM can be performed in contact mode or tapping mode. In tapping mode, a piezoelectric crystal is used to oscillate the cantilever near its resonant frequency. A feedback controlled piezoscanner measures the oscillation amplitude and adjusts the sample surface-tip separation to keep constant force and amplitude on the sample by actuating the cantilever in Z-direction. The resolution in Z direction is on the order of $\mathring{A}$ and constrained by the electrical or thermal noises, while the lateral resolution is limited by the tip radius typically on the order of few nanometers.

AFM measurements in this work were carried out using Veeco DI 3100 Atomic Force Microscopy in tapping mode to study the surface roughness and the quality of the ALD films. All measurements were taken using NanoWorld Pointprobe® NCH probes with a resonance frequency of 320 kHz and a force constant of 42 N/m. The scans were made from a 1x1 μm^2 area and a resolution. Figure 3.1 shows the AFM images for three samples of 30 nm ZnO thin films.

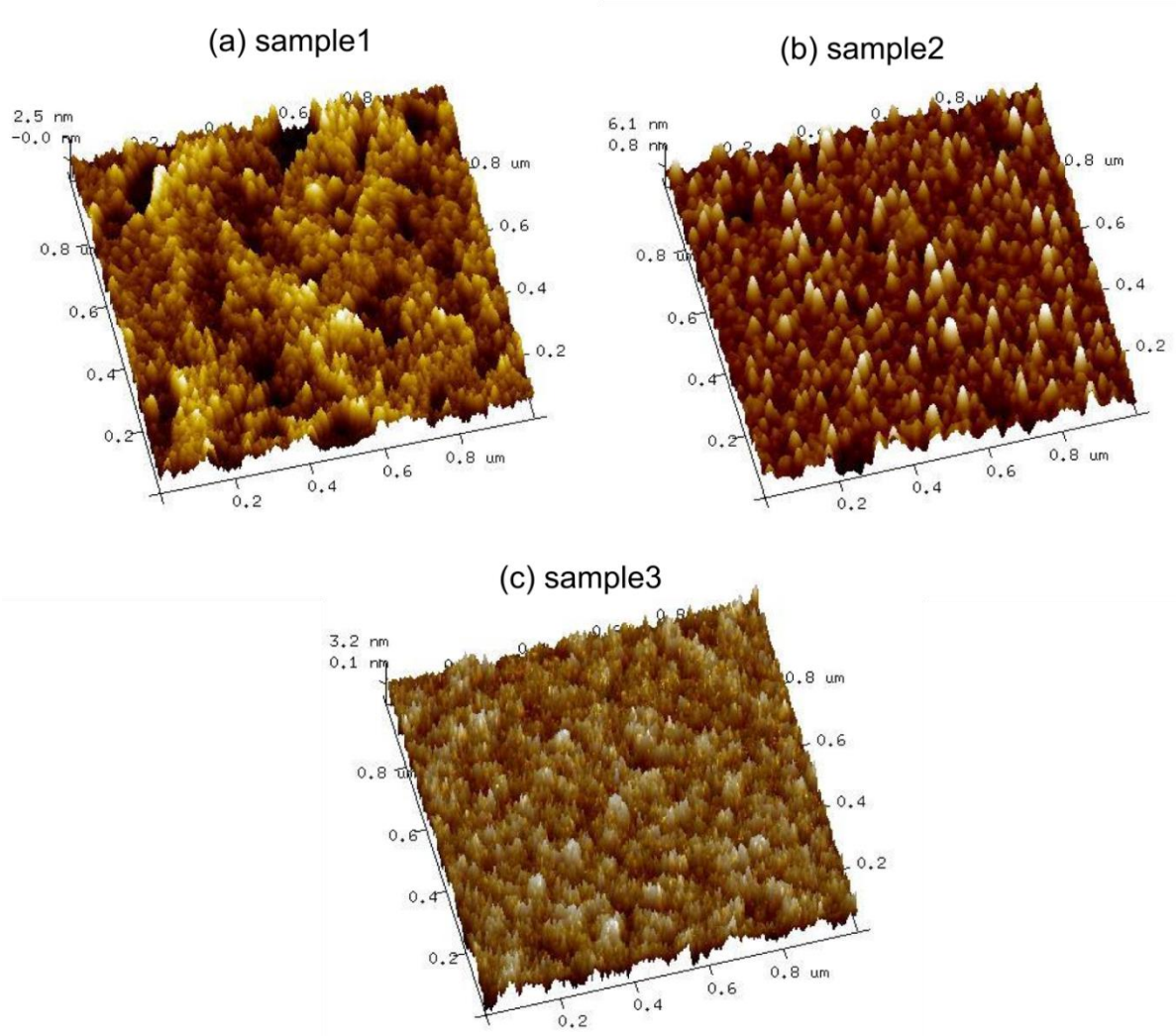

Figure 3.2. Typical AFM images of ZnO thin films deposited by (a) 200°C TALD on TiW substrates (b) 200°C PEALD, (c) 50°C PEALD on SiO_2 substrate.

After capturing of the AFM images, the NanoScope Analysis v1.40r1 software was used to process the images. The images were subjected to 3rd order flattening to remove any nonlinear background artifacts due to the piezoscanner. Three different roughness parameters including root mean square roughness (R_q), average roughness (R_a), and the maximum roughness depth (R_{max}), were analyzed and summarized in Table 3.1. The particle analysis was also carried out and shown in Table 3.1. All the films showed nanoscale grain sizes close to AFM tip radii which

limited the minimum grain size that can be detected. T-200 ZnO showed smoother surface than the P-200 as well as a smaller grain size. P-50 ZnO also showed smoother surface than the P-200 as well as smaller grain sizes. The AFM analysis suggests that the roughness of the ZnO thin films is significantly affected by the crystallinity, i.e. crystal size. The variation of surface profile increases with larger grain size. For T-200 ZnO, the AFM image show non-uninform contrast with dark shadow areas. The roughness analysis verifies the dark shadow areas are not pinholes in the film. This non-uniform contrast in T-200 ZnO thin film may be attributed to the polycrystalline nature of the film with various crystal orientations, which will be further established in XRD structural study in next section.

Table 3.1. Processed information from AFM images for three ZnO thin films (see Table 2.1 for the corresponding recipe).

sample	**Recipe**	**Substrate**	R_q (nm)	R_a (nm)	R_{max} (nm)	**Majority particles' sizes** (nm)
1	T-200	TiW	0.756	0.598	6.09	10-20
2	P-200	TiW	1.37	1.02	12.9	10-30
3	P-50	SiO_2	0.884	0.704	8.36	10-20

3.3 X-RAY DIFFRACTION

X-ray diffraction (XRD) technique uses monoenergistic X-ray beam to interact with the sample and is diffracted in specific direction according to Bragg's law[107]

$$2dsin\theta = n\lambda \qquad (3.1)$$

where d is the spacing between diffracting crystalline planes, θ is the incident angle, n is an integer, and λ is the wavelength of the beam. The interplanar distances d can then be determined by the specific directions θ where the diffraction peaks were detected.

Rigaku Ultima IV in-plane system embedded with Cu-Kα radiation (λ=1.5405 Å) and a thin film mode attachment were used to investigate the crystallinity of the ZnO thin films with

power setting of 40 kV and 44 mA. Since the standard θ-2θ scan XRD can penetrate deep into the substrate, signals from the deeper substrate layer can dominate the weaker diffraction from the ZnO layer. The glancing angle X-ray diffraction (GAXRD) is used to characterize the ultra-thin ZnO films with a beam incident angle of ω (from 0.2 ° to 0.5 °) to the substrate surface. The GAXRD has many advantages over the standard θ-2θ scan XRD including a superior signal/noise ratio[108]. The scan speed was set as 2.00 °/min with a 0.05 ° sampling width.

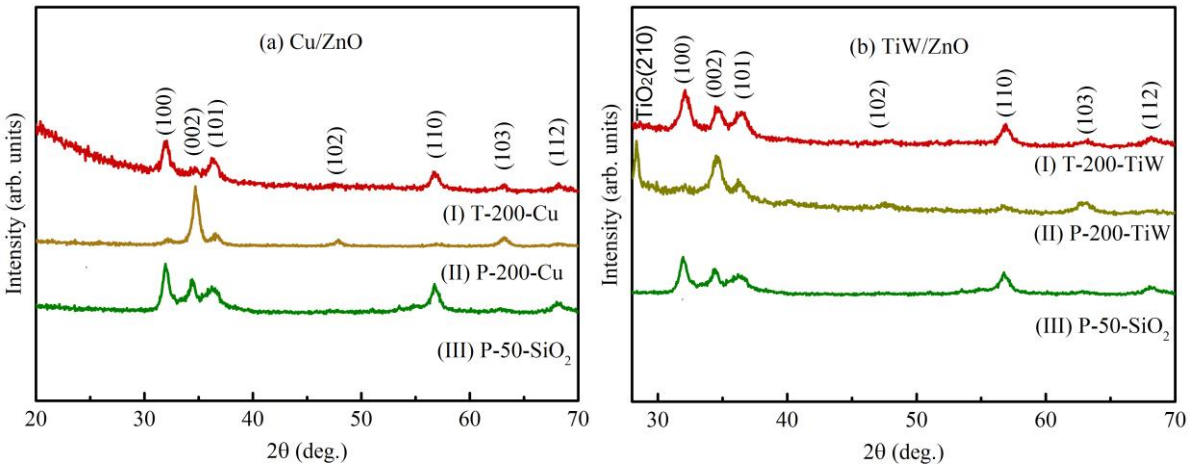

Figure 3.3. GAXRD profiles with ω=0.2 ° for (a) ZnO thin films on Cu substrates; (b) ZnO thin films on TiW substrates; The GAXRD profile with ω=0.5 ° for P-50-SiO_2 is added in both figures for comparison. Note: the anonymous peaks not belong to ZnO in (b) are attributed to bottom TiW layer.

The GAXRD profiles of the ZnO thin films are shown in Figure 3.3 for two set of samples on different substrates with the P-50-SiO_2 for comparison. All of the ZnO showed the hexagonal crystal structure in consistent with the existing liturature[97]. The ZnO peaks (100), (002), (101), (102), (110) and (103) peaks match well with wurtzite ZnO[109]. The P-200 ZnO shows preferred orientation of (002) while T-200 and P-50 show preferred orientation of (100). The GAXRD profiles for Cu and TiW substrates demonstrate similar diffraction peaks positions except the presence of anonymous peaks most likely from the bottom TiW layer in P-200-TiW.

While the intensity of each peaks varies between two different substrates indicating that the crystalline orientation of the ZnO thin film is dependent on the substrate nature[110].

Figure 3.4 shows a comparison between the GAXRD and θ-2θ standard mode XRD profiles for P-50-SiO_2. The θ-2θ standard mode XRD profile shows three major peaks at (100), (002) and (101) with comparable intensities, indicating the polycrystalline nature of the P-50 ZnO. Note that the sharp anomalous peaks not marked are from the Si substrate.

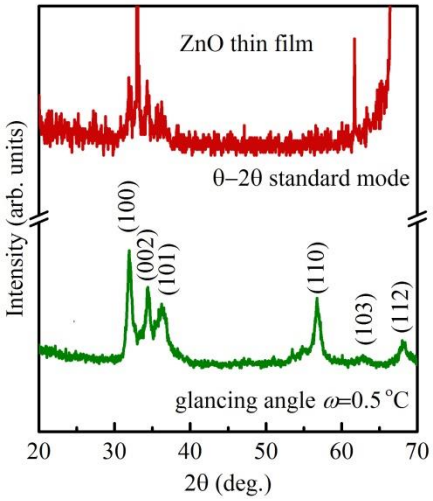

Figure 3.4. Comparison of XRD patterns from GAXRD and θ-2θ standard mode for P-50 ZnO on SiO_2.

3.4 X-RAY PHOTOEMISSION SPECTROSCOPY

X-ray photoemission spectroscopy (XPS) is a quantitative spectroscopic technique for sample's chemistry analysis including elemental composition, electronic states of the element and chemical bonding. A monochromatic soft X-ray beam is applied and focued on the material surface to interact with the samples. The sample material absorbs the X-ray photos and emits electrons which have kinetic energies ($E_{kinetic}$) high enough to escape from the sample surface. The escaping electrons are then detected by a spectrometer in a typical takeoff angle of 90°,

giving a XPS spectrum profile of count rate versus binding energy of ejected electrons. The binding energy is giving by

$$E_{binding} = E_{photon} - (E_{kinetic} + q\Phi) \qquad (3.2)$$

This is known as Ernest Rutherford's equation, where E_{photon} is the known photon energy, qΦ is the work function of the spectrometer. The profile of specific $E_{binding}$ identifies the elements. The shift of the $E_{binding}$ gives information of the oxidation state of the element. The areas of the peaks for different element in a sample provide the stoichiometric ratio of the material. The escaped electrons are usually ejected from 2 to 20 atomic layers deep. The penetration depth can be reduced by tilting the sample or reduce the takeoff angle. The resolution of the XPS is limited to 1.0 atomic percentage (at. %).

XPS measurements in this work were performed using an ULTRA (Kratos Analytical) AXIS-165 spectrometer using monochromatic Al-Kα radiation (hv = 1486.69 eV) ran at a power of 210 W. The systems is equipped with an in situ Argon gun which enables surface cleaning and sputter etching by 4 keV Ar^+ ions, providing a depth profiling study. The system is pumped to an ultrahigh vacuum (10^{-9} torr) under measurement and the X-ray beam is focused to a 300μm×700μm area. High-resolution spectra with step energy of 0.1 eV were collected for P-200 and T-200. Finally, the XPS data were analyzed using CasaXPS software. The binding energies for all peaks were calibrated by the C1s peak at 284.8 eV.

A series of high resolution XPS profiles of Zn, O, C, and Cu (substrate) are used to determine the material stoichiometric of ZnO respect to a continuously etching time. As can be seen from Figure 3.5, the T- ZnO close to the interface shows a Zn-rich interface while the P-200 shows an O-rich interface. The first-principles calculations showed that he formation energy of

the defects including oxygen vacancies (V_O), zinc interstitials (Zn_i), and Zn antisites (Zn_O) in ZnO material are favored in Zn-rich condition[18,111–113].

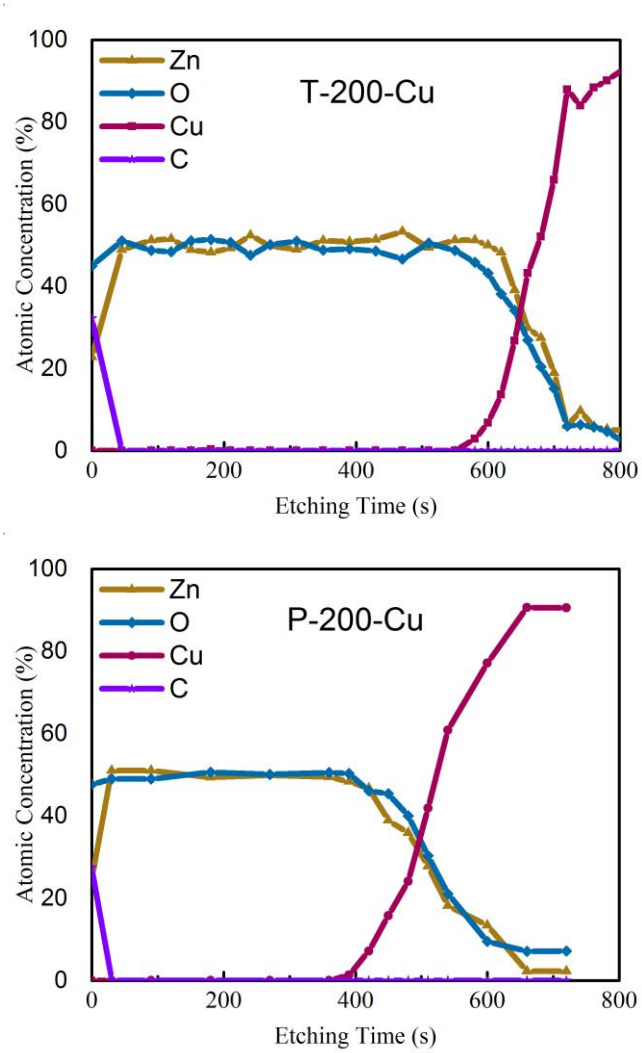

Figure 3.5. The depth profiles for T-200-Cu and P-200-Cu.

The intrinsic defects all behave as donors are believed to be responsible for the inherent n-type nature of ZnO[114]. Among those native defects, V_O has the lowest formation energy in either Zn-rich environment. The role of oxygen vacancies as a shallow donor has been questioned recently, instead, it was regarded as a deep level defects with a ε(2+/0) transition level located approximately at 0.7±0.2 eV respect to the conduction band minimum[18,112,113,115].

Such a deep transition level implies V_O defects are unlikely to contribute to free carrier concentration in ZnO at room temperature. However, they can act as generation-recombination (G-R) centers in the space charge region for G-R current transport or traps assisting tunneling current transport[116] leading to poor on/off rectification.

Furthermore, Figure 3.6 shows the high resolution XPS spectra of O1s with the dominant peak at 529.9 eV of binding energy and a shoulder peak at 531.7 eV. The former dominant peak comes from metal-O bond, in this case, referring to Zn-O bonds, while the shoulder peak is assigned to the O atoms in Zn-OH bonds[117]. The at. % of Zn-OH chemical state out of the total O is calculated to be 11% and 10% for T-200-Cu and P-200-Cu, respectively. This observation suggested that ZnO thin films deposited by both TALD and PEALD at 200 °C have abundant hydrogen impurity while the TALD leaves a bit more –OH reaction sites during deposition compared to that of PEALD. The behavior of hydrogen in ZnO has been well-established that H is responsible, at least partially, for the inherent n-type conductivity in ZnO[51,62,112,118,119].

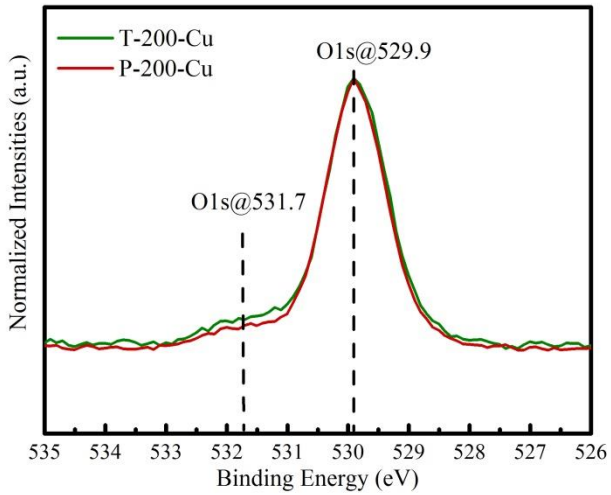

Figure 3.6. High resolution XPS spectra of O1s for T-200-Cu at the etching time of 310 s and P-200-Cu at the etching time of 270 s.

3.5 SUMMARY

The topography, crystallinity and chemistry of the ZnO thin films grown by TALD, and PEALD at various deposition temperatures are studied and compared in this chapter. The XRD results show that all the films under study have multiple crystalline orientations, i.e. polycrystalline nature. The P-200 ZnO thin films have stronger preferred orientation than the T-200 films. Since the P-200 films grown on different substrates show similar XRD patterns, it indicates that substrate type has no strong impact on the polycrystalline property of the ZnO thin films. In addition, the XRD spectra for PEALD films grown at 200 ºC and 50 ºC (refer to Figure 3.3) show that higher deposition temperature may improve the crystalline property of the films.

The FESEM images reveal that the grain shape and grain size varies with different precursors and deposition temperatures. The P-200-Cu has a surface feature with round grains and 20-30 nm average grain sizes while the TALD-200-Cu has a surface feature with majority rice-like grain shape with partial round grains areas and slightly smaller grain sizes. The P-100-Cu also shows round grains but smaller size and the P-50-SiO_2 shows the smallest round grain size and smoothest surface compared to ZnO grown at higher temperatures. Grain size analysis on the AFM images reveals similar trend as that from FESEM images. Surface roughness analysis on the AFM images reveals that the surface roughness is related to the grain size and crystalline orientation of the material. The films with larger grain size tend to have rougher surface. The ZnO film processed by TALD shows some distinct areas with different grain shape and size may be related to its more randomly oriented polycrystals.

The XPS studies give a comparison of stoichiometric composition and chemical bond between ZnO thin films fabricated with TALD and PEALD at the same deposition temperature of 200 °C. The PEALD ZnO shows an oxygen-rich interface while the TALD ZnO has a zinc-

rich interface with same substrate metal, suggesting that PEALD ZnO have reduced defects densities at the interface of Schottky contacts and potentially giving better Schottky behavior. Besides, the P-200 and T-200 ZnO both reveal abundant hydrogen impurities, suggesting high doping densities in both films and potential high tunneling probability across the Schottky barrier.

Chapter 4

Schottky Contact Formation and Characterization

This chapter introduces the general understanding of Schottky contacts formation and current transport mechanisms though the metal-semiconductor interface, explains the Schottky contacts' 'figure of merit' contributing to the device performance, described how to determine these parameters and identify the governing current transport processes. In the end, a model is proposed for analysis of these specific Schottky diodes based on ZnO thin film.

4.1 INTRODUCTION

Schottky diodes are essentially one of the simplest devices in semiconductor technology which consist of two metal electrodes to a given semiconductor: one side with a rectifying (Schottky) behavior and the other side with a linear (ohmic) behavior. The rectifying behavior in metal-semiconductor contacts was first discovered in 1874 with a thin metal wire on a galena (lead sulfide) by Braun[120]. This point contact arrangement, known as point rectifier, was widely used in early crystal radio receivers with the advantage of giving low capacitance especially important for radio detection, but simultaneously comes with high series resistance, poor rectification ratio, poor reproducibility and early reverse breakdown because of electric field crowding (i.e., enhanced electric field) near the sharp point contacts. Thus, most modern Schottky diodes use larger area contacts with a diameter about 10 um to 1 mm fabricated with various techniques like thermal or electron beam (E-beam) evaporation, sputtering, pulsed laser deposition (PLD), etc.

4.2 SCHOTTKY CONTACT FORMATION

The simplest semiconductor device building block-Schottky contact, surprisingly, can give insights into the complex semiconductor interface and bulk properties, thus provides an alternative way to characterize the materials for various applications. It is well known that the Schottky contact formation deviate from conventional Schottky-Mott model due to the complex nature of semiconductor surfaces with reconstructed energy band structure and high density of dangling bonds. Generally, the defects introduced by the interactions between the metal and semiconductor affect the Schottky barrier formation. Therefore the underlying physics governing Schottky contacts formation attracts lot of interest in developing contacts for diverse material systems.

4.2.1 Schottky-Mott Model

Conventional Schottky barrier formation model was proposed by Schottky[121] and Mott[122] in 1938 by assuming there is no interactions of any kind between the metal and semicondutor. Figure 4.1 depicts the Schottky contact formation process. Figure 4.1a gives the energy band structure of an isolated metal adjacent to an isolated *n*-type semiconductor before contact. The work function of metal (Φ_M) is generally different from the that of semicondutor (Φ_S), both referring to the energy differences between the Fermi levels (E_F) and the vacuum level (E_0) of the material. Note that the Fermi level in the semicondutor depends on the doping concentration at which the Fermi-Dirac distribution function equals to ½. The electron affinity (χ_S) is defined in semicondutor as the energy difference between the conduction band to the vacuum level. When the metal and semiconductor are bought into contact, since the respective Fermi levels for any solid in contact must be the same in thermal equilibrium, electron will travel from the higher

Fermi level side to the lower one until equalization occurs, leading to the reconstruction of the energy band structure. To build up a Schottky barrier, the work function of the metal side is higher than that of the semiconductor side, electrons flow from the semiconductor conduction band to the metal as shown in Figure 4.1b, resulting in a space charge region (depletion region) in semiconductor close to the interface. The build-in potential prevent the electrons from moving to the metal and maintaining a zero net current on the interface as shown in Figure 4.1c.

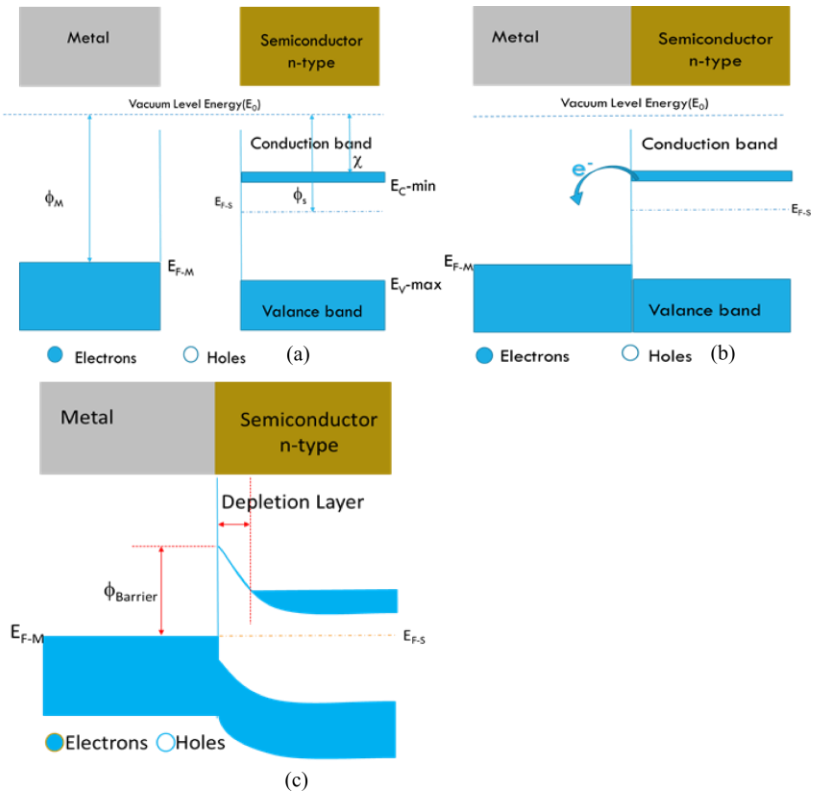

Figure 4.1. Schottky-Mott model of n-type semiconductor Schottky contact: (a) isolated metal and semiconductor band structure; (b) metal and semiconductor are brought into contact ;(c) thermal equilibrium band structure of Schottky contact.

In the absence of interface states, i.e. Schottky-Mott model, the ideal Schottky barrier height (Φ_{B_SMM}) is simply fixed by the metal's vacuum work function (Φ_M) and the semiconductor's vacuum electron affinity (χ_S)

$$\Phi_{B\_SMM} = \Phi_M - \chi_S \qquad (4.1)$$

Although the empirical Φ_B of Schottky contacts never obey the Schottky-Mott model relationship[123], it can be used as an initial prediction of the Schottky barrier height. A table consisting of work funcion of metals and their respective Φ_{B_SMM} to ZnO predicted by Schottky-Mott Model is listed in Table 4.1.

Table 4.1 Work function and Φ_{B_SMM} for polycrystalline potential candidates[214].

Elements	Work function (Φ_M) eV	SMM barrier height (Φ_{B_SMM}) eV
Au	5.1	0.9
Pt	5.65	1.45
Ag	4.26	0.06
Ni	5.15	0.95
Cu	4.65	0.45
W	4.55	0.35
B	4.45	0.25
Cr	4.5	0.3
Al	4.28	0.08

*ZnO electron affinity: 4.2eV[85]

4.2.2 Fermi Level Pining Phenomena

An interface behavior parameter $S_\Phi = d\Phi_B/d\Phi_M$ can be used to determine the relation between effective Schottky barrier height (Φ_B) and Φ_M. In classical Schottky-Mott Model, S_Φ is unity according to eq 4.1. The experimental values of S_Φ for a range of common semiconductors is summerized in Figure 4.2[124]. It can be seen that the experimentally determined interface behavior parameter S_Φ is generally much smaller than the unity. For semiconductors like Si, Ge, GaAs, etc., the experimentally determined Φ_B is almost independent of the Φ_M. This phenomena is known as Fermi level pining and is usually attributed to the interface charge states which lower the Φ_B[125]. As a result this will lead to a net change in the potential energy arrangement for n-type Schottky contact as

$$\Phi_B = \Phi_M - \chi_s + qD_{int} \qquad (4.2)$$

where D_{int} is the potential due to the interface dipole.

The origin of the D_{int} term in eq 4.2 is due to interactions between metal and semiconductor including (i) the overlap of electron wave functions[126], (ii) the creation of native defects introduced either by the metallization or the abrupt interruption of the periodic structure of crystal lattices, and (iii) chemical bonding[124,127]. These interactions create interface charges in both sides of the contact separated by a small physical gap θ about a few Angstroms subsequently leading to the interface dipoles formation. The lack of success of the Schottky-Mott model indicates that these interactions have to be considered in modelling the Schottky contact formation. These types of interaction models are generally referred to as fixed separation models[124], which will be discussed and compared here.

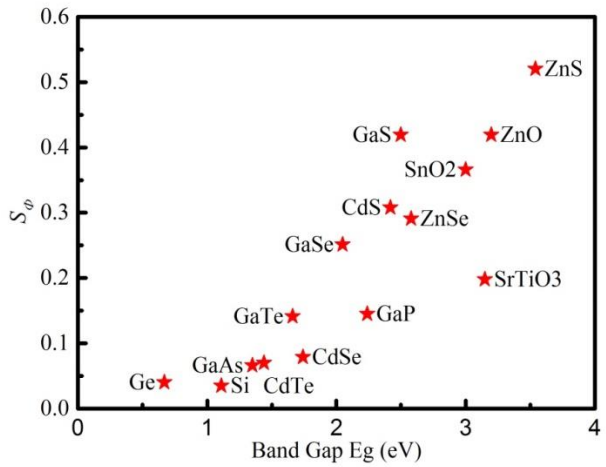

Figure 4.2. Experimental values of interface behavior parameter S_Φ versus bandgap for a range of common semiconductor[124].

4.3 CHARACTERIZATION OF SCHOTTKY CONTACT FIGURE OF MERIT

There are numbers of methods available to determine the Φ_B including current-voltage (*I-V*) measurements, capacitance-voltage (*C-V*) measurements and photoelectric measurements as

introduced by Schroder[128]. For their simplicity, *I-V* measurements and *C-V* measurements are the most widely adopted ones and commonly used by the researchers to characterize the Schottky barrier heights. The ideal electrical characteristics are deduced based on Schottky-Mott model with assumptions: (i) uniform doping; (ii) fully depleted space charge region; (iii) excess carriers flowing through the contact do not interrupt the thermal equilibrium of the barrier. However, the measured electrical characteristics are not ideal. Thus, in the analysis of measured electrical characteristics, the non-ideality factors are necessary to be included. In addition, the capacitance-frequency and conductance frequency techniques are commonly used to explore the interface defects and bulk impurity levels. All of the electrical characteristics reported here were measured by Keithley 4200-SCS with Schottky metal contact as anode and top Al/Au contact as cathode as indicated in Figure 2.4b in section 2.3.

4.3.1 Current-Voltage Measurements

4.3.1.1 Schottky Barrier Heights Extraction

4.3.1.1.1 Ideal Current-Voltage Model

Current-voltage (*I-V*) measurements are the most widely adopted technique to determine the barrier heights ($q\Phi_B$) of Schottky contacts. The widely used theory of the current transport across Schottky contacts was first developed by Bethe in 1942[129]. It proposed that the current flow is determined by electrons for n-type semiconductor, with enough energy to overcome the Schottky barrier by thermionic emission (TE). As mentioned above, for the validity of this method, the thermal equilibrium of the barrier must be maintained provide that $\Phi_B >> kT/q$.

The TE currents flowing through the Schottky contact in either direction are equal in equilibrium and determined by the Φ_B[130],

$$I_{TE}(S \rightarrow M) = I_{TE}(M \rightarrow S) = AA^{*}T^{2}exp\left(-\frac{q\Phi_B}{kT}\right) \qquad (4.3)$$

where $I_{TE}(S \rightarrow M)$ is the current from semiconductor to the metal, $I_{TE}(M \rightarrow S)$ is the current from metal to semiconductor, A is the device area. The diameter of all diodes characterized in this thesis is 100 μm. A^* is the Richardson constant which only depends on the effective mass of the materials, k is the Boltzmann constant, and T is the absolute temperature of the contact. When the Schottky contact is forward biased as shown in Figure 4.3a with an external bias voltage (V) on the anode, i.e. the metal side, the built in potential decreases by qV allowing the electrons flow from the semicondutor to the metal. The current density from the metal to the semiconductor becomes

$$I_{TE}(M \rightarrow S) = AA^{*}T^{2}exp\left(-\frac{q(\Phi_B - V)}{kT}\right) \qquad (4.4)$$

While the current flowing in the reverse direction is fixed by the Φ_B and independent of the applied voltages,

$$I_{TE}(S \rightarrow M) = AA^{*}T^{2}exp\left(-\frac{q\Phi_B}{kT}\right) \qquad (4.5)$$

Thus, the net forward current density (J_{fwd}) flowing across the Schottky contact is

$$I_{fwd} = I_{TE}(M \rightarrow S) - I_{TE}(S \rightarrow M) = I_S\left[\exp\left(\frac{qV}{kT}\right) - 1\right] \qquad (4.6)$$

$$I_S = AA^{*}T^{2}exp\left(-\frac{q\Phi_B}{kT}\right) = I_{s1}\exp\left(\frac{-q\Phi_B}{kT}\right) \qquad (4.7)$$

where I_S is the known as the saturation current. For $V>3kT/q$, the -1 term in eq 4.6 becomes neglibible and then the forward current should increase exponentially with applied voltage V.

When the Schottky contact is reverse biased as shown in Figure 4.3b with an external bias voltage (V) in the anode, i.e. the metal side, the built in potential increases by qV which makes $I_{TE}(S \rightarrow M) >> I_{TE}(M \rightarrow S)$ resulting in a net reverse current of $I_r = I_0$ independent of V.

Eq 4.6 is valid for the ideal case provided TE is the only current transport mechanism involved and the Schottky barrier is homogeneous, defect free and has no interface states. For realistic cases, an ideality factor n is introduced into eq 4.6 to incorporate the non-ideal factors for analysis of the *I-V* characteristics,

$$I = I_S\left[\exp\left(\frac{qV}{nkT}\right) - 1\right] \qquad (4.8)$$

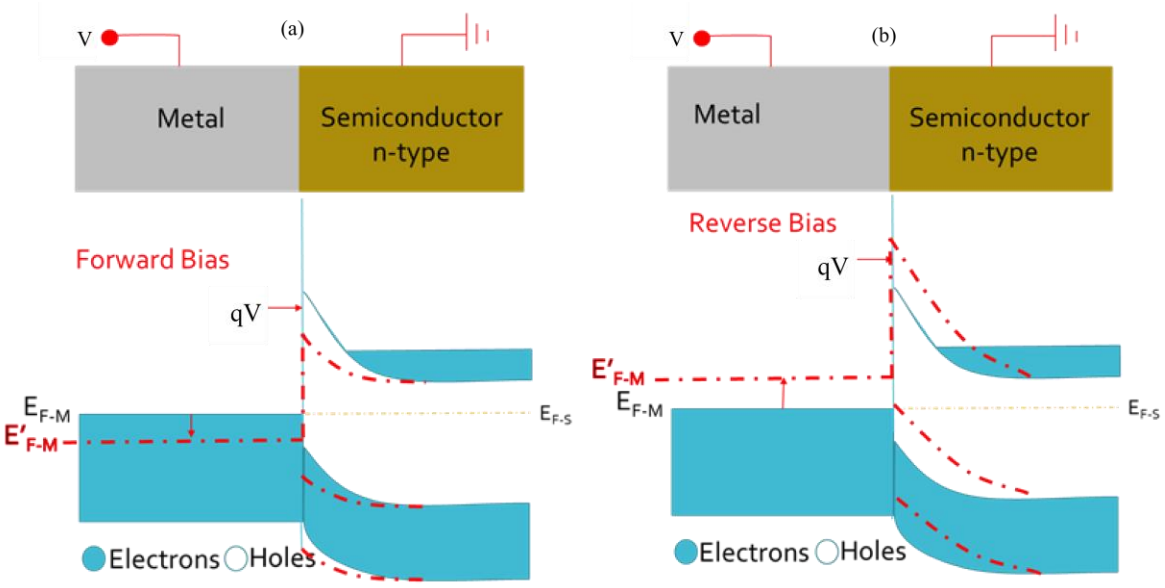

Figure 4.3. Schottky barrier band structure at forward bias voltage; (b) Schottky barrier band structure at reverse bias voltage.

The *I-V* characteristics are usually plotted as current density versus voltage (*J* versus *V*) in semi-log scale provided the physical contact area is well defined, from which the saturation current density J_S can be determined by extrapolating the linear region of the semi-log scaled *J-V* plot at forward bias voltages to V=0. Then the Φ_B can be extracted as

$$\Phi_B = \frac{kT}{q}\ln\left(\frac{J_S}{A^*T^2}\right) \qquad (4.9)$$

The ideality factor n can be determined from the slope of the same linear region of the semi-log scaled *J-V* plot at forward bias voltages. Provided $V >> kT/q$,

$$n = \frac{q}{kT}\left(\frac{d \ln J}{dV}\right)^{-1} \qquad (4.10)$$

To extract the value of Φ_B for a particular diode one typically uses the theoretical Richardson constant A^* value only depending on the effective mass of the materials. In practice, the value of apparent Richardson constant A^{**} is usually not the theoretical value of A^*, and depends on the contact preparation processes including the surface cleaning, sample annealing and metal deposition processes. It is complicated to obtain an accurate A^{**} value. But fortunately, A^* appears in the 'ln' term in eq 4.9, which means if A^* is varied by a factor of 2, the extracted $q\Phi_B$ would change by $0.7kT$. Another type of error arises in choosing the linear range from the semi-log scale *J-V* plot. Since other current transport mechanisms could modify the lower part of the *J-V* plot, especially for structures with high barrier height, while the upper limit affected by the series resistance. Therefore the linear region is reduced making it difficult to fit the experimental *J-V* characteristics with a wide range of temperature when the non-ideal effect on the currents becomes significant[116].

4.3.1.1.2 Voltage-dependent Model for Schottky Barrier

The deviation from TE model is typically due to: (i) TE is not the only dominant current transport mechanism; (ii) the series resistance is too large. In those cases, the ideality factor increases and the physical meaning of the extracted Φ_B cannot be justified as that defined in the thermionic emission model. Empirical values of *n* are usually greater than unity because of non-ideal behaviors. The common mechanisms causing the non-ideal behaviors include image force lowering, field emission, interfacial thin native oxide layer, and lateral barrier inhomogeneity. These mechanisms will be described in Section 4.4.

It has been suggested that the effect of the non-ideality should be included not only for the $I_{TE}(M \rightarrow S)$ but also for the $I_{TE}(S \rightarrow M)$[131]. Assuming the Φ_B depends linearly on voltage as

$$\Phi_B(V) = \Phi_{BV0} + \gamma(V - IRs) \qquad (4.11)$$

Where $\gamma > 0$ since the Φ_B increases with increasing forward bias voltage. The substitution of eq 4.11 in eq 4.6 yields

$$I = AA^*T^2 exp\left(-\frac{q\Phi_{BV0}}{kT}\right) \exp\left(\frac{q(V-IRs)}{nkT}\right)\left[1 - \exp\left(\frac{-q(V-IRs)}{kT}\right)\right] \qquad (4.12)$$

where Φ_{BV0} is the Φ_B at zero bias, and ideality factor is defined as

$$\frac{1}{n} = 1 - \gamma = 1 - \frac{d\Phi_B}{dV} \qquad (4.13)$$

provided R_S is negligible. Thus, a plot of $\log[I/(1-exp(-qV/kT)]$ versus V should now give a straight line all the way to the V=0 and a wider range from which n can be determined.

4.3.1.2 Series Resistance Extraction

4.3.1.2.1 Single Point Approach

The reduction of the diodes thickness can reduce the series resistances and subsequently improve the radio frequency (RF) response for demanding applications. Thus Series resistance (Rs) is one of the important parameters that need to be considered in the developing of Schottky diodes. At large current and large forward bias voltages, the I-V characteristics deviates from linearity which can be attributed to the Rs with $\Delta V = IR_S$, allowing R_S to be simply determined at a particular point according to

$$R_s = \frac{\Delta V}{I} \qquad (4.14)$$

4.3.1.2.2 First Order Derivation of I-V Characteristics Approach

The slope method to extract *R*s is also developed based on eq 4.8[128]. The method is potentially more accurate than the single point approach. When the influence from *R*s on the current becomes significant, For $V >> kT/q$, eq 4.8 can be expressed as

$$I = I_S \exp\left[\frac{qV_D}{nkT}\right] \qquad (4.15)$$

when the effect of R_S is significant, $V_D = V - IR_s$, and eq 4.15 can be rewritten as

$$V = IR_s + n\phi_B + \frac{nkT}{q}\ln\left(\frac{I}{AA^*T^2}\right) \qquad (4.16)$$

Differentiating eq 4.16 with respect to *I* and rearranging terms, we obtain

$$\frac{\mathrm{d}V}{\mathrm{d}(\ln I)} = IR_s + \frac{nkT}{q} \qquad (4.17)$$

Thus, a plot of d*V*/d(ln*I*) versus *I* will give *R*s as the slope, and *nkT/q* as the intercept of *y*-axis.

4.3.1.2.3 Norde Method and Deviations

Another method to extract Schottky parameters was first proposed by Norde[132]. Assuming an ideal diode with *n*=1, the Norde function can be expressed as

$$F = \frac{V}{2} - \frac{kT}{q}\ln\left(\frac{I}{AA^*T^2}\right) \qquad (4.18)$$

Substituting eq 4.16 into eq 4.18 yields

$$F = -\frac{1}{2}V + IR_s + \phi_B \qquad (4.19)$$

when $V >> IR_S$ so that the term IR_S can be neglected, eq 4.19 gives the first order derivative of -1/2 for *F(V)*. When $V \approx IR_S$, eq 4.19 gives the first order derivative of 1/2 for *F(V)*. Hence, *F(V)*

should have a minimum point lying between these two limits at voltage of V_{min}. The corresponding current is I_{min}. At the minimum point where dF/dV=0, the R_S is

$$R_s = \frac{2}{I_{min}} \frac{kT}{q} \qquad (4.20)$$

Substituting eq 4.20 into eq 4.19, the minimum F value is obtained

$$F_{min} = -\frac{1}{2} V_{min} + \frac{2kT}{q} + \phi_B \qquad (4.21)$$

The R_S of the diode is calculated from I_{min} at $V=V_{min}$. One disadvantage of this technique is that an apparent A^* must be known for an accurate evaluation. However, the apparent A^* for particular diodes commonly deviates from its theoretical value depending on the specific contact preparation. In the absence of an accurate apparent A^*, one has to assume a theoretical value or literature values. Another disadvantage of this method is that it assumes n=1, which is not valid in most practical cases.

A modified Norde method was proposed by Sato and Yasumura[133]

$$F = \left(\frac{1}{2} - \frac{1}{n}\right) V + \frac{IR_S}{n} + \phi_B \qquad (4.22)$$

to extract the value of n, Φ_B, and R_S from the I-V measurements of Schottky diodes. Their approach extends the validity of this method to n<2 but requires two experimental I-V measurements conducted at different operating temperature and the determination of minima of the modified function. Besides, the apparent A^* value is still needed.

Another modified Norde method to determine R_S and Φ_B of the diodes was defined as[69]

$$F = \frac{V}{\gamma} - \frac{kT}{q} \ln\left(\frac{I}{AA^*T^2}\right) \qquad (4.23)$$

where γ (dimensionless) is the first integer greater than *n.* This method overcomes the limitation of $n<2$ but still need the apparent A^* value and the determination of minima of the F versus V plot. The value of Φ_B can be determined as

$$\Phi_B = F(V_{\min}) + \frac{V_{\min}}{\gamma} - \frac{kT}{q} \qquad (4.24)$$

Where $F(V_{min})$ is the the minimum point of F and V_{min} is the corresponding voltage. *Rs* value can be determined as

$$R_s = \frac{\gamma - n}{I_{\min}} \frac{kT}{q} \qquad (4.25)$$

It is noted that all of these approaches based on original Norde method have the difficulties of obtaining an accurate value for the F function minimum. Several variations of the Norde method have been proposed to overcome these difficulties and n limitations. H-function is one of these developed by Cheung and Cheung[134] and defined as

$$H(I) = V - \frac{nkT}{q} \ln\left(\frac{I}{I_{s1}}\right) \qquad (4.26)$$

With eq 4.16, eq 4.26 becomes

$$H(I) = n\Phi_B + IR_s \qquad (4.27)$$

Thus, a plot of $H(I)$ versus I will give *Rs* as its slope, and $n\Phi_B$ as its y-intercept. Similar to that of F plot, the H plot also needs the apparent A^* value.

4.3.2 Current-Voltage-Temperature Measurements

Current-voltage-temperature (*I-V-T*) measurements are typically used to extract the apparent A^* provided the physical area of the Schottky contact is well-defined. It also provides a

self-consistency check of the Φ_B derived from the *I-V* measurements in a wide range of temperature. Eq 4.7 can be written as

$$ln(I_s/T^2) = \ln(AA^{**}) - q\Phi_B/kT \qquad (4.28)$$

Where A^{**} is the apparent Richardson constant. A plot of $ln(I_S/T^2)$ versus $1/T$ known as a Richardson plot can be obtained which should be a straight line and gives $-q\Phi_B/k$ as its slope and $ln(AA^{**})$ as its y-intercept if the Φ_B is independent of temperature. The slope of the plot is usually well defined whereas the extraction of A^{**} involving extrapolating the slope to the vertical axis ($1/T = 0$) over a long distance is prone to error since the experimental data usually covers only a narrow temperature range. Uncertainty in the data typically can lead to a large uncertainty in A^{**}.

Precautions should be taken if the Schottky parameters from the *I-V-T* measurements are temperature dependent. The variation of barrier heights and ideality factors extracted from *I-V-T* measurements by classical thermionic emission model can be attributed to the existence of excess current introduced by superposition of recombination current and/or field emission current over thermionic emission, or the presence of potential fluctuations at the interface of metal and semiconductor. In this case, accurate extraction of *n* and Φ_B becomes difficult by the standard Richardson plot. Based on the *I-V* relationship proposed by Hackam and Harrop[135] as

$$I = AA^{**}T^2 exp\left(-\frac{q\Phi_B}{nkT}\right) \exp\left(\frac{qV}{nkT}\right) \qquad (4.29)$$

Bhuiyan *et al*. proposed a modified Richardson plot as

$$n(T)ln\left(\frac{I_S}{T^2}\right) = a\ln(AA^{**}) + \alpha/k - (1/T)(\Phi_{BT0} - kblnA^*)/k \qquad (4.30)$$

by taking into account the temperature dependence of both the *n* and Φ_B based on their empirical observations as

$$n(T) = a + b/T \qquad (4.31)$$

And

$$\Phi_B(T) = \Phi_{BT0} - \alpha T \qquad (4.32)$$

where Φ_{BT0} is the Φ_B at absolute 0 K.

4.3.3 Capacitance-Voltage Measurements

The capacitance-voltage (*C-V*) technique provides an alternative method to obtain Φ_B even without a well-defined physical contact area. The barrier heights obtained by the C-V measurements are regarded as the most reliable value not strongly affected by non-ideal behavior[136].

4.3.3.1 Schottky Barrier Heights Extraction

As described above in the Schottky-Mott model, the equalization of Fermi levels of the contacted metal and semiconductor results in a depletion region which can be regarded as a dielectric layer naturally. It consists of space charges due to the ionized donors and locates entirely in the semiconductor side of the contact. Thus, the depletion region forms a "planar capacitor" with the metal and the non-depleted semiconductor bulk as the parallel plates. The width of the depletion region W_d can be determined by applying the Poisson equation with "full depletion approximation" which means[130]

i. All the donors in the depletion region from the Schottky interface to the W_d are completely ionized with resultant positive charge;
ii. The semiconductor bulk region beyond the depletion region is neutral with zero electric field.

The charge density profile in the semiconductor thus becomes

$$\rho(x) = \begin{cases} qN_D & 0 < x < W_d \\ 0 & x \geq W_d \end{cases} \qquad (4.33)$$

where N_D is the effective doping density of the semiconductor, as shown in Figure 4.4a. The positive charge density in the semiconductor is exactly equalized by the negative charge in the metal

$$Q_M = -Q_S = -qN_D W_d \qquad (4.34)$$

So that the net charge is zero and the electrical field beyond the depletion region is zero. To determine the electric field distribution in the depletion region, we can start with the one dimensional Poisson equation

$$\frac{d\xi}{dx} = -\frac{d^2V}{dx^2} = \frac{\rho(x)}{\varepsilon_S \varepsilon_0} \qquad (4.35)$$

With the boundary condition $\xi(W_d) = 0$, the electric field distribution in the depletion region as shown in the Figure 4.4d is

$$\xi(x) = \begin{cases} -\frac{qN_D}{\varepsilon_S \varepsilon_0}(W_d - x) & 0 < x < W_d \\ 0 & x \geq W_d \end{cases} \qquad (4.36)$$

The maximum electric filed $\xi max = -qN_D W_d/\varepsilon_S \varepsilon_0$ can be obtained at the Schottky interface. By integrating the $-\xi(x)$ from 0 to x, the potential distribution in the semiconductor as shown in Figure 4.4c can be obtained

$$V(x) = \begin{cases} -V_{bi}\left(1 - \frac{x}{W_d}\right)^2 & 0 < x < W_d \\ 0 & x \geq W_d \end{cases} \qquad (4.37)$$

where V_{bi} is the build-in voltage representing the potential drop across the depletion region of the semiconductor. The width of the depletion region W_d can be obtained as

$$W_d = \sqrt{\frac{2\varepsilon_S \varepsilon_0 V_{bi}}{qN_D}} \qquad (4.38)$$

In practice, the thermal energy distribution of the majority carrier has to be considered. Thus the potential drop across the depletion region becomes $V_{bi}-kT/q$, the width of the depletion region becomes

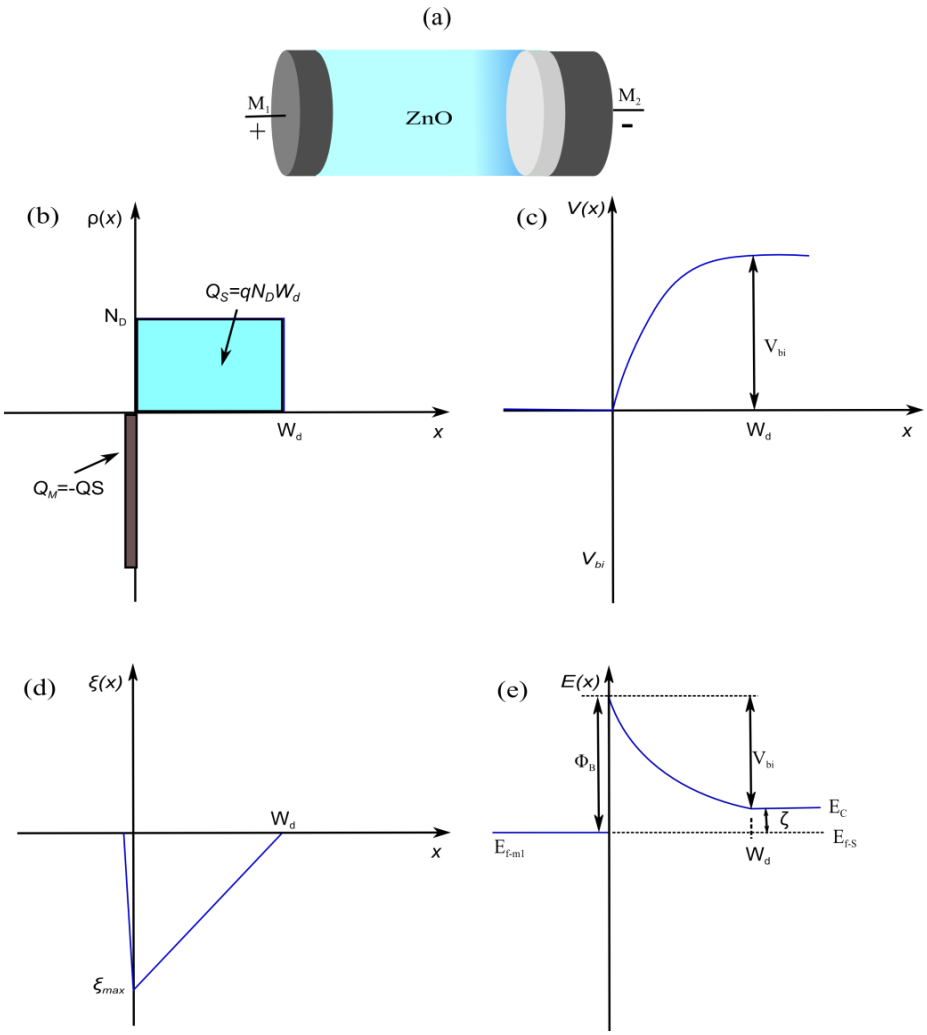

Figure 4.4. (a) A schematic diagram of the Schottky diode, (b) charge distribution, (c) potential distribution, (d) electric field distribution, (e) energy distribution across the Schottky barrier.

$$W_d = \sqrt{\frac{2\varepsilon_S\varepsilon_0}{qN_D}\left(V_{bi} - \frac{kT}{q}\right)} \qquad (4.39)$$

And the maximum electric field becomes

$$\xi_{max} = -\sqrt{\frac{2qN_D}{\varepsilon_S\varepsilon_0}\left(V_{bi} - \frac{kT}{q}\right)} \qquad (4.40)$$

When a small external voltage is applied, the boundary condition changes from *V(Wd) = 0* to *V(Wd) = V*, the W_d varies subsequently as

$$W_d = \sqrt{\frac{2\varepsilon_S\varepsilon_0}{qN_D}\left(V_{bi} - \frac{kT}{q} - V\right)} \qquad (4.41)$$

Provided the physical contact area *A* is known, the total space charge Q_{SC} in the depletion region is

$$Q_{SC} = qN_D W_d A \qquad (4.42)$$

The small-signal capacitance (*C*) of the depletion region can be obtained from dQ_{SC}/dV, resulting in

$$C = A\sqrt{\frac{q\varepsilon_S\varepsilon_0 N_D}{2(V_{bi} - kT/q - V)}} \qquad (4.43)$$

And

$$\frac{A^2}{C^2} = \left(\frac{2}{q\varepsilon_S\varepsilon_0 N_D}\right)\left(V_{bi} - \frac{kT}{q} - V\right) \qquad (4.44)$$

In the *C-V* measurements, the capacitance is measured as a function of the applied external voltage (*V)* by applying a small AC signal with a typical frequency between 10 kHz to 1 MHz. The *C-V* measurements are then plotted as $1/C^2$ versus *V* of which the V_{bi}-kT/q is obtained by extrapolating the slope of $1/C^2$ versus *V* to the $1/C^2$axis.

The Φ_B of the Schottky contact is related to the V_{bi} by

$$\Phi_B = V_{bi} + \zeta \qquad (4.45)$$

Where

$$\zeta = \frac{kT}{q}\ln\left(\frac{N_C}{N_D}\right) \qquad (4.46)$$

where N_C is the effective density of states in the conduction band.

4.3.3.2 Effective Donor Concentration extraction

The *C-V* technique can also be used to obtain depth profile of the effective donor concentration of the semiconductor. The effective donor concentration is obtained from the slope of $1/C^2$-V curve as

$$N_{C-V} = \left(-\frac{2}{q\varepsilon_S\varepsilon_0}\right)\left[d\left(1/{C_D}^2\right)/dV\right]^{-1} \qquad (4.47)$$

or from the *dC/dV* method with[137]

$$N_{C-V} = \frac{{C_D}^3}{q\varepsilon_0\varepsilon}\frac{dV}{dC_D} \qquad (4.48)$$

both as a function of depth

$$W_{C-V} = \frac{\varepsilon_0\varepsilon}{C_D} \qquad (4.49)$$

where C_D is the capacitance density,

$$C_D = C/A \qquad (4.50)$$

The $1/C^2$-*V* plot is preferred in analyzing *C-V* characteristics as it can easily tell if the carrier density is uniform. In the simplest case for non-compensated and homogeneously doped semiconductor, the C-V concentration $N_{C\text{-}V}$ equals to the free carrier concentration and donor concentration. While for the semiconductor with large variation of the donor concentration, the $N_{C\text{-}V}$ does not have a direct physical meaning but related to the total depletion charge.

4.3.4 Frequency-dependent Capacitance and Conductance Method

Capacitance - frequency (*C-F*) and conductance - frequency (*G-F*) techniques have been commonly used to investigate the interface states energy distribution in the bandgap of the contact interface. Ideally, the diode capacitance and conductance should be frequency-

independent. However, in reality the quantities usually are dependent on frequency due to the presence of interface defect states and/or the series resistance R_S and impurity levels[69,138,139].

equivalent circuit models

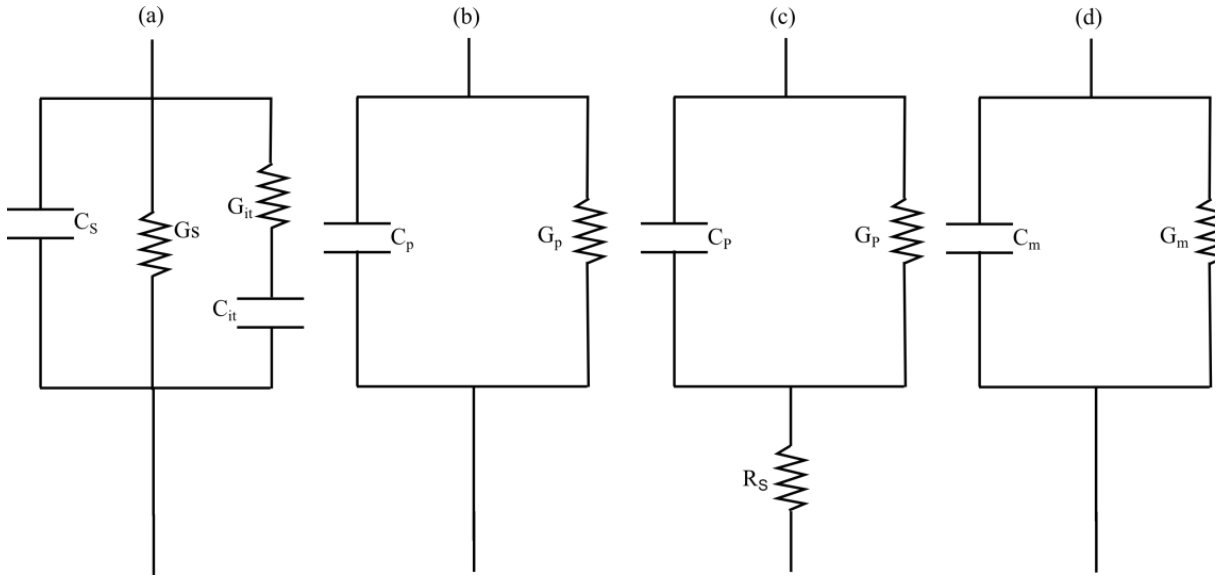

Figure 4.5. The small signal equivalent circuits for capacitance and conductance measurements; (a) Schottky diode depletion region capacitance C_S and conductance G_S with interface trap time constant $\tau_{it} = C_{it}/G_{it}$; (b) simplified parallel circuit of (a); (c) taking into account series resistance R_S; (d) measured circuit.

The electron emission-capture process at interface states in equilibrium is able to follow the low frequency AC signals and provide a source of excess capacitance C_{it} beside C_S from the depletion region. The conductance represents the loss mechanisms due to the carrier transport over the Φ_B and the interface trap capture and emission. Figure 4.5a depicts the complete equivalent circuit for the Schottky diode with interface traps. The normalized parallel capacitance C_p and G_p in the simplified circuit as shown in Figure 4.5b are defined as[128]

$$C_p = C_s + \frac{C_{it}}{1+(\omega\tau_{it})^2} \qquad (4.51)$$

$$\frac{G_p}{\omega} = \frac{G_s}{\omega} + \frac{q\omega\tau_{it}D_{it}}{1+(\omega\tau_{it})^2} \qquad (4.52)$$

Where $C_{it} = q^2 D_{it}$, $\omega = 2\pi f$ (f is the measurement frequency) and $\tau_{it} = C_{it}/G_{it}$, is the interface time constant. Eq 4.51 and eq 4.52 are for interface traps with single energy level in the band gap. For interface defects continuously distributed in the energy band gap, the primary capture and emission occurs by traps located around the Fermi level within a few kT/q leading to a time constant dispersion, the parallel G_p then becomes [140]

$$\frac{G_p}{\omega} = \frac{G_S}{\omega} + \frac{qD_{it}}{2\omega\tau_{it}} \ln[1 + ((\omega\tau_{it})^2)] \qquad (4.53)$$

Eq 4.51 and eq 4.52 show that the parallel capacitance and conductance are depending on not only applied voltage from C_S and G_S, but also frequency. At a fixed applied bias voltage, the C_S and G_S are constants. The interface traps density and the time constant can be extracted from *C-f* and *G-f* measurements provided the C_{it} and G_{it} are not screened by C_S and G_S. Capacitance meter which generally assumes the device to consist of the parallel C_m - G_m combination as shown in Figure 4.5d should directly give the C_p and G_p.

For diode with appreciable series resistance, Figure 4.5c gives a more complete circuit with the R_S. Compare the circuits in Figure 4.5c and d gives[141]

$$G_m = \frac{G_p(G_p R_s + 1) + \omega^2 {C_p}^2 R_s}{(G_p R_s + 1)^2 + \omega^2 {C_p}^2 {R_s}^2} \qquad (4.54)$$

$$C_m = \frac{C_P}{(G_p R_s + 1)^2 + \omega^2 {C_p}^2 {R_s}^2} \qquad (4.55)$$

$$C_P = \frac{C_m}{(1 - G_m R_s)^2 + \omega^2 {C_m}^2 {R_s}^2} \qquad (4.56)$$

$$G_p = \frac{\omega^2 C_m C_P R_s - G_m}{G_m R_s - 1} \qquad (4.57)$$

The interaction of R_S and R_P cause the measured capacitance to be underestimated in parallel mode of the capacitance meter. For $G_p \ll 1/R_s$ and low frequencies, the effect of R_s to the

measured capacitance can be neglected, the parallel capacitance is close to the measured capacitance. By fitting *C-f* curve with eq 4.51, the interface trap density and time constant can be obtained. As to the G_m *-f* curve, when the diode current is small and R_S is negligible, the loss due to the interface states becomes dominant and it should show a maximum peak at $\omega \approx 1/\tau_{it}$ (or $\omega \approx 2/\tau_{it}$ for continuously distributed defect energy leading to a time constant dispersion). The density of states is given by the first derivative of eq 4.52,

$$D_{it} = \frac{2}{\mathrm{q}}\left(\frac{G_p}{\omega}\right)_{\max} \quad \text{for single level} \qquad (4.58)$$

or

$$D_{it} = \frac{2.5}{q}\left(\frac{G_p}{\omega}\right)_{\max} \quad \text{for continuous levels} \qquad (4.59)$$

In n-type semiconductor, the energy of the interface states E_{ss} with respect to the conduction band is given by[138,142]

$$E_c - E_{ss} = q\Phi_B - q(V - IR_s) \qquad (4.60)$$

where E_c is the bottom of conduction band.

By applying either of the two methods in appropriate applied voltage range and frequency range, an energy distribution of the interface states could be obtained for a specific Schottky contact.

4.4 NON-IDEAL BEHAVIOR IN CURRENT TRANSPORT

There are numbers of mechanisms which could cause non-ideal behavior in current transport. These mechanisms include image force lowering (IF), thermionic field emission (TFE), defect-assisted tunneling, recombination, lateral barrier inhomogeneity, etc., as shown in Figure 4.6. In this section, the major sources which cause non-ideal behavior in nanodiodes based on polycrystalline oxide semiconductor will be described.

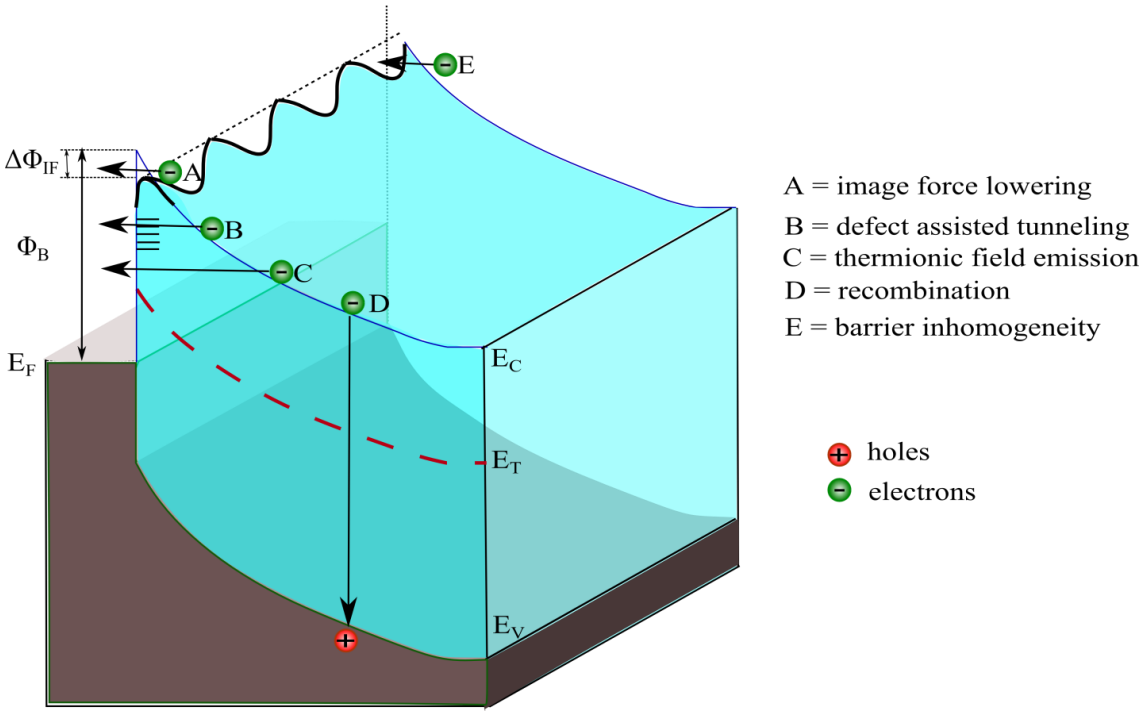

Figure 4.6. Non-ideal behaviors in current transport across Schottky barrier.

4.4.1 Image Force Lowering

In ideal Schottky-Mott model described in Section 4.2.1, the ideal Schottky barrier height of the Schottky contact is determined by the metal work function and semiconductor electron affinity. In reality, the effective barrier heights of Schottky contacts are always slightly reduced by the image force (IF) lowering effect even for perfect Schottky contact with perfect crystallinity, homogeneous interface potential and no interface states. This effect is produced by a small attractive force between the electron approaching the barrier and its respective positive "image" charge induced in the metal[143] and results in a barrier height lowering by $\Delta\Phi_{IF}$ given by

$$\Delta\Phi_{IF} = \left[\left(\frac{q^3 N_D}{8\pi^2 \varepsilon_\infty{}^2 \varepsilon_S \varepsilon_0{}^3}\right)\left(\Phi_B - \frac{kT}{q} - V - \zeta\right)\right]^{\frac{1}{4}} \qquad (4.61)$$

Where ε_∞ is the image force dielectric constant, other symbols have their usual meanings. Eq 4.61 implies that the $\Delta\Phi_{IF}$ increase with increasing reverse bias. The resultant Φ_B varies depending on applied voltage V. Also, the $\Delta\Phi_{IF}$ is positively dependent on the effective donor concentration N_D for a given semiconductor. Thus, for moderately doped semiconductor, although $\Delta\Phi_{IF}$ is small, it can lead to a deviation of reverse current from a constant I_S, i.e., voltage-dependent reverse currents. It is worthwhile to note that the IF lowering only affects the *I-V* characteristics but not *C-V* characteristics as it is only produced by electrons which approach the barrier. The ideality factor of a Schottky contact due to the IF lowering is increased to

$$\frac{1}{n_{IF}} = 1 - \frac{\Delta\Phi_{IF}}{4}\left(\Phi_B - \frac{kT}{q} - V - \zeta\right)^{-1} \qquad (4.62)$$

4.4.2 Thermionic Field Emission

According to the eq 4.38, the width of the depletion region W_d is proportional to the effective donor concentration $N_D^{-1/2}$. Thus, for heavily doped semiconductors the barrier may be sufficiently thin for electrons to tunnel directly through it. A more preferred process for moderately doped semiconductor is thermionic field emission (TFE), in which the electrons are thermally excited to a position on the barrier where it can tunnel through. A tunneling parameter E_{00} determined by[144]

$$E_{00} = \frac{qh}{4\pi}\left(\frac{N_D}{m^*\varepsilon_S\varepsilon_0}\right)^{\frac{1}{2}} \qquad (4.63)$$

where m^* is the effective electron mass, can be compared to the thermal energy kT to evaluate the relative probability of these processes. When $E_{00} << kT$, the dominant current transport process is the thermionic emission, whereas when $E_{00} >> kT$ the field emission, i.e., tunneling becomes

significant. For E_{00} is comparable to kT, the current transport will be affected by maily TFE, leading to a lowering of the Φ_B by

$$\Delta\Phi_{TFE} = \left(\frac{3E_{00}}{2}\right)^{\frac{2}{3}}\left(\Phi_B - V - \frac{kT}{q} - \zeta\right)^{\frac{1}{3}} \qquad (4.64)$$

And the ideality factor is increased to

$$n_{TFE} = \frac{qE_{00}}{kT}coth\left(\frac{qE_{00}}{kT}\right) \qquad (4.65)$$

Thus, the ideality factor n_{TFE} varies with the temperature in the presence of TFE. For Schottky contacts of moderately doped semiconductor with infinite semiconductor layer, the probability of the TFE is very low. However, it can be enhanced with the presence of defect states or traps in the depletion region which provide a tunneling route to promote the tunneling probability and consequently increase the ideality factor n_{TFE}.

4.4.3 Generation and Recombination

Generation and recombination (G-R) currents can occur in the depletion region of a Schottky contact as that in p-n junction by simultaneous capture of elections and holes assisted by defects states in the semiconductor. The G-R current can be described by the relation[116]

$$I_{G-R} = I_{S-GR}\left[\exp\left(\frac{qV-IR_S}{2kT}\right) - 1\right] \qquad (4.66)$$

And

$$I_{S-GR} = \frac{qn_iW_d}{2\tau} \qquad (4.67)$$

Where n_i is the minority carrier concentration and τ is the minority carrier lifetime with in the depletion region and is inversely proportional to the defect density so that the G-R current increase with increasing defect density. For wide band semiconductor like ZnO, the n_i is very small therefore the $I_{G\text{-}R}$ can be negligible. Instead, the hopping current transport induced by electrons tunneling between defects states for these materials may be important.

4.4.4 Barrier Inhomogeneity

The presence of Schottky barrier inhomogeneity was recognized and reported sporadically before 1990s[145–148]. This issue has not received serious attention until the advances achieved in ballistic electron emission microscopy (BEEM) technique provided the spatial resolution needed to study the potential distribution underneath the metal layers[149,150]. The presence of Schottky barrier inhomogeneity is very common because: (i) any defects and contamination in the interface may provide as the sources for the barrier potential fluctuation, (ii) non-epitaxial growth of materials can lead to the local variation in interface atomic structure varies locally, and (iii) the interface dipole induced by the interaction between metal and semiconductor can vary laterally. The Schottky barrier inhomogeneity may be particularly important for polycrystalline Schottky diodes studied here[125].

Song et al.[151] has firstly introduced an analytical potential fluctuation model assuming the contact area is composed of isolated sub-areas with definite Φ_B following a Gaussian distribution. The model provides a physical insight for the difference in Φ_B obtained from capacitance-voltage and current-voltage measurements. Recently, Tung proposed a dipole-layer approach which induced an embedment of low barrier patches in a higher background uniform barrier[145]. The barrier inhomogeneity approach generally assumes a lateral distribution of non-uniform Schottky

barrier height in the contact area and different functions including Gaussian and exponential distributions have been proposed[152]. Among these functions, the Gaussian distribution is most widely adopted and it leads to useful expressions for current-voltage characteristics. The model developed by Werner and Guttler[153] is widely used for Schottky barrier inhomogeneity which assumes a Gaussian distribution P(Φ_B) for spatial distribution of the Φ_B with a mean value of $\bar{\Phi}_B$ and a standard variation of δ as described by:

$$P(\Phi_B) = \frac{1}{\delta_S\sqrt{2\pi}} \exp\left(-\frac{(\Phi_B-\bar{\Phi}_B)^2}{2{\delta_S}^2}\right) \qquad (4.68)$$

where $\frac{1}{\delta_S\sqrt{2\pi}}$ is the normalization constant of the Gaussian distribution. The total current under the forward bias voltage is given by[154]:

$$I = \int_{-\infty}^{+\infty} I(\Phi_B, V)\, P(\Phi_B) d\Phi_B \qquad (4.69)$$

Provided pure thermionic emission dominant the current transport,

$$I = A \cdot A^* T^2 \exp\left(-\frac{q\Phi_B^{inh}}{kT}\right) \exp\left[\frac{q(V-IR_S)}{n_{inh}kT}\right] \qquad (4.70)$$

Where the A^* is the theoretical Richardson constant. Φ_B^{inh} and n_{inh} are the apparent Φ_B at zero bias and apparent ideality factor respectively, given by:

$$\Phi_B^{inh} = \bar{\Phi}_{B0} - \frac{q{\delta_0}^2}{2kT} \qquad (4.71)$$

$$\left(\frac{1}{n_{inh}} - 1\right) = \rho_2 - \frac{q\rho_3}{2kT} \qquad (4.72)$$

where $\bar{\Phi}_{B0}$ stands for the mean barrier height and δ_0 is the standard deviation, both at zero bias. It is assumed that the mean barrier height $\bar{\Phi}_B$ and standard variation δ^2 linearly depend on bias voltage: $\bar{\Phi}_B(V) = \bar{\Phi}_{B0} + \rho_2 V$ and standard deviation $\delta^2(V) = \delta^2_0 + \rho_3 V$, where $\bar{\Phi}_{B0}$ is the mean barrier height at zero bias, ρ_2 (dimensionless) and ρ_3 are the voltage coefficients which may depend on T. These assumptions quantify the deformation of the barrier height distribution

caused by the bias voltage[153]. The temperature dependence of the standard deviation δ is usually negligible.

The relation of the Richardson plot could now be modified by taking into account the barrier inhomogeneity. The expression of the modified relation is

$$\ln(j_s/T^2) - \left(\frac{q^2\delta_0{}^2}{2(kT)^2}\right) = \ln(A^{**}) - \frac{q\bar{\Phi}_{B0}}{kT} \qquad (4.73)$$

Thus, the A^{**} can be calculated from the y-intercept and $\bar{\Phi}_{B0}$ from the slope of the ln (j_s/T^2)-q^2 $\delta_0{}^2/2(kT)^2$ versus q/kT plot.

During the extraction of Φ_B^{inh} and n_{inh}, an initial value of A^* which is the theoretical Richardson constant of the material is used. The reliability of the extracted parameters in this barrier inhomogeneity model is discussed here. Similar to that discussed above in section 4.3.1, A^* (or A^{**} in this case) appears in the 'ln' term in eq 4.9, which means if A^* (or A^{**}) is varied by a factor of 2, the extracted effective barrier height, the Φ_B^{inh} in this case, would change by $0.7kT$; The resultant discrepancies in δ_0 and $\bar{\Phi}_{B0}$ are about 2% and 3%, respectively, indicating that the values of δ_0 and $\bar{\Phi}_{B0}$ are little relevant to the initial value of A^*. In contrast, the extraction of apparent Richardson constant A^{**} in eq 4.73, is highly relevant to the initial value of A^*.

Chapter 5

Schottky Nanodiodes Results and Analysis

5.1 INTRODUCTION

The choice of the best metal for Schottky contacts to ZnO is an important topic in the developing of ZnO based technology. Many noble metals have been widely used as Schottky electrodes on ZnO in the literatures[44,47,49,51,54,64,66–71,155,156]. Potential interdiffusion and chemical reactions between the electrodes and ZnO could be harmful to the device performance. In particular for the bottom electrode configuration in this thesis, the thermal stability of the electrodes is an essential concern to obtain good device performance, since the interface interaction could be enhanced by heating during the fabrication process of the diodes. The source of heating can come from the photolithography process which can reach 115 °C during the photoresistor baking and in the range of 50 to 200 °C during the ALD process.

An overview of literatures on thermal stability studies with several Schottky contact metals relevant to this thesis is given below. There are several reports indicating that Au electrode tends to interact seriously with ZnO at ambient temperature higher than 60 °C[59,60,115]. Some studies indicated that Ag contact has a slightly better thermal stability than that of Au[59,115]. Temperature-dependent electrical characterizations showed that both Pt and Pd formed thermal stable contacts to bulk ZnO up to 200 °C[62,63,157,158]. However, Pt contact on *n*-type ZnO thin film degraded significantly after annealing at 300 °C[63]. Tungsten (W) contact on (0001) bulk ZnO crystal was found to be stable up to ~700 °C without any detectable intermixing due to the high melting points of W (3410 ◦C)[64]. Elemental Copper (Cu) has been widely used in silicon-based

integrated circuits because of its excellent thermal and electrical conductivity, high electromigration resistance and low cost[159]. However, Cu diffuses easily into semiconductor layers so that a diffusion barrier is normally required in the Si-based devices. And thermal stability of Cu Schottky contacts is one of the most important issues in Si devices. In the case of other material system, Chang-da Tsai *et al.*[45] reported Cu Schottky contacts to InGaP were stable with thermal stability up to 450 ºC.

Alloys and other compounds materials can also be good Schottky contact candidates. Sputtered TiW alloys have good thermal and electrical properties, high corrosion resistance and low diffusion of metals. Hence, it is used as diffusion barrier between Al and Au and in the presence of silicides. However, in the case of using TiW alloy as contact to ZnO, one uncertainty is the interdiffusion of Ti and ZnO based on the evidences that Ti/Au as an ohmic contact to ZnO thin film showed significant changes in morphology for > 200 °C[60], and that Ti and the ZnO react to form Ti-O phases after annealing at 250 °C[60]. Recent studies showed that partial oxidized noble metals such as PdO_x, AgO_x and IrO_x have good thermal stability at 180 °C[160,161]. Since the interactions of electrodes to various material systems typically differ from one to another, a systematic study on the stability of metal contacts on ZnO is important for devices consist of ZnO Schottky contact.

As discussed in section 1.4 Schottky nanodiodes based on ultrathin ZnO film grown at low temperature are ideal for many applications. In the following sections a number of systematic studies on ZnO Schottky nanodiodes are reported. In study I, metals shown rectifying behavior on P-200 ZnO are identified. The electrical characteristics of the P-200 Schottky diodes are studied. Material studies to investigate the interface chemistry of the winning contacts TiW and Cu contacts are reported. In study II, the effects of PEALD deposition temperatures, metal

surface plasma pretreatment durations as well as thermal stability of Cu contact are studied. In study III, comprehensive studies for P-50 Schottky nanodiodes are reported. The studies include (i) the identification of Schottky metals in some of which have been rarely applied as Schottky contacts to ZnO in literatures; (ii) the long-term stabilities for all P-50 ZnO Schottky contacts with aging, providing a piece of evidence for interface interaction extent between ZnO and these electrodes; (iii) interface defects and temperature-dependent behavior for the winning contacts Pt and Cu. The temperature-dependent measurements on Cu and Pt Schottky nanodiodes also provide an estimate of their thermal stabilities; (iv) series resistance analysis for the best nanodiode, P-50-Pt; (v) the mechanisms involved in the diode behavior. In the last section of this chapter, a current transport model for the ZnO Schottky nanodiodes is developed by using analytical transfer matrix method.

5.2 STUDY I: P-200 AND T-200 SCHOTTKY NANODIODES

5.2.1 Summary of Device Behavior

Schottky nanodiodes based on T-200 and P-200 ZnO were firstly investigated. Metals including Cu, Ni, Pt, Au, Ag, and TiW were used as the bottom electrode to investigate their suitability as Schottky contacts. These candidates are selected according to their work function (see Table 4.1) and their thermal stability, and also for comparison to previous reported works. The ohmic contact was kept as Al/Au stacks for all diodes. The resultant contact type of each device is determined by *I-V* measurements and summarized in Table 5.1 with either ohmic (linear) or Schottky (rectifying).

Table 5.1 Summary of P-200 and T-200 Schottky diodes performance

Contact Metal	P-200	T-200
Au	ohmic	ohmic
Ag	Schottky	ohmic
Pt	ohmic	ohmic
TiW	Schottky	ohmic
Cu	Schottky	ohmic
Ni	Schottky	ohmic

None of the devices with T-200 ZnO thin films showed Schottky behavior. We attributed it to the extremely high free carrier concentration nature of the T-200 ZnO thin film. There are numbers of mechanisms that can lead to high free carrier concentration: (i) high concentration of hydrogen (H) related dopants like hydroxyl detected in high resolution XPS study, hydrocarbons and free H atoms; (ii) zinc-rich interfacial layers observed from the XPS study, and (iii) more random orientations of the polycrystalline grains observed from the XRD study. Please refer to Chapter 3 for the details of thin film characterizations. As to the devices with P-200 ZnO thin films, the Au and Pt contacts appeared to be ohmic while other reactive metals showed rectifying behavior (Schottky).

Despite the fact that Au has been widely investigated as a rectifying contact to ZnO, its rectifying behavior varies significantly depending on the interface conditions and ambient temperatures in literatures[48,54,95,115,162–164]. Mosbacker *et al.*[51] demonstrated a conversion of Au contact from ohmic to rectifying behavior by remote oxygen plasma treatment on atomically ordered polar single-crystal ZnO. The authors attributed the conversion to the removal of the adsorbate-induced accumulation layer and reduction of near-surface donor density and defects leading to a lower tunneling and hopping current transport. Neville and Mead[164] measured an effective barrier height value of 0.66 eV for Au on chemically prepared ZnO crystals with an

unspecified orientation. Polyakov *et al.*[59] measured the effective barrier height of ~0.65 eV for Au on (0001) Zn surface of bulk *n*-ZnO crystals. The authors also indicated that the Au Schottky diodes were degraded by heating to 365 K (92 °C) in vacuum due to chemical reaction between Au and ZnO interface. Simpson and Cordaro[115] also indicated that Au contacts on single-crystal ZnO are easily degraded with thermal cycling under room temperature. To this end, the ohmic behavior of the Au/ZnO contacts in this work is attributed to their poor thermal stability since the bottom Schottky contact has to be heated to 200 °C in the ZnO growth process.

Unlike the Au contacts, the Pt contacts were reported with good thermal stability for temperatures lower than 200 °C. A potential reason for the Pt/ZnO contact showing ohmic behavior could be there are the insufficient O species deposited onto the Pt surface during the growth of initial layers due to the simultaneously oxygen desorption is enhanced by higher temperature, subsequently creating a Zn rich interface layer in the contact and becoming a ohmic type due to high tunneling current. A further study of the interface chemical states is needed to confirm this speculation.

5.2.2 Electrical Characteristics of P-200 ZnO Schottky Diodes

Typical normalized $I-V$ (J-V) characteristics for Ag, TiW, Cu and Ni Schottky contacts on P-200 ZnO are shown in Figure 5.1a in semi-log scale. The linearity of the logarithmic of the forward-bias junction current versus voltage is poor due to the significant effect of series resistance or voltage-dependent Φ_B. The precise extrapolation of Schottky parameters (Φ_B and n) from J-V characteristics becomes difficult since it requires that the series resistance has negligible contribution in V_D at $V_D > 3kT/q$ and also Φ_B is a constant. While the approach based on the semi-log $J/\{1-\exp[-qV/kT]\}$ versus voltage plot is valid for the entire bias range and

allows for a linear dependence of Φ_B on applied voltage, as discussed in section 4.3.1.1.2. Since the series resistance effect on the *J-V* characteristics vanishes when the current gets to zero, the extrapolation of Schottky parameters from the small current region in the semi-log $J/\{1-\exp[-qV/kT]\}$ versus voltage plot should be more accurate. The semi-log $J/\{1-\exp[-qV/kT]\}$ versus voltage plots for all the diodes are shown in Figure 5.1b. The Φ_{B0} and n_0 are then determined from the y-intercept and the slope for nearly zero current region of the semi-log $J/\{1-\exp[-qV/kT]\}$-*V* plot for each diode, according to eq 4.12. The theoretical Richardson constant A^* value of 32 A cm^{-2} K^{-2} is used for the calculations with $m^* = 0.27\,m_0$ for ZnO[54,56,58,63–65,68,71,155,157,158,165–168].

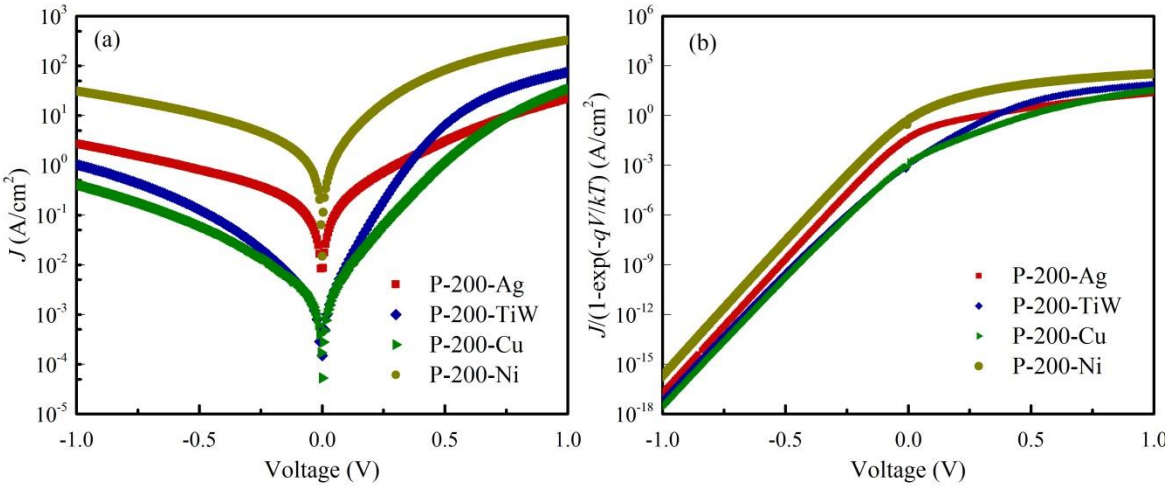

Figure 5.1 (a) Typical normalized *I-V* characteristics for Schottky contacts with P-200 ZnO thin films; (b) A logarithmic plot of the $J/\{1-\exp[-qV/kT]\}$ versus voltage respect to the (a).

The obtained Schottky parameters from both *J-V* plot (Φ_B and *n*) and $J/\{1-\exp[-qV/kT]\}$-*V* plot (Φ_{B0} and n_0), plus the rectifying ratio at ±1 V, are shown in Table 5.2. The effective barrier heights calculated by these two approaches for each diode are close to each other. While the ideality factor n_0 calculated form the $J/\{1-\exp[-qV/kT]\}$-*V* plot is obviously smaller than *n* calculated form *J-V* plot, which can be attributed to the presence of series resistance. The larger

of the deviation between n_0 and n suggest more significant of the series resistance effect. By comparing the measured *J-V* characteristics and the Schottky parameters in Table 5.2, one can tell that the extent of the effect from series resistance is not only depends on the value of the series resistance but also depends on the magnitude of the current, corresponding to the IR_S term in eq 4.12. Furthermore, the $J/\{1\text{-}\exp[-qV/kT]\}$-$V$ plot is not linear even at V=0 V would suggest that the R_S is not the only factor leading to the large ideality factor.

Table 5.2 Schottky parameters for Schottky contacts with P-200 ZnO thin films. (All the measurements were performed at room temperature.)

Sample	Φ_B (eV)	n	Φ_{B0} (eV)	n_0	*Ratio* @ ±1 V
P-200-Ag	0.44	4.45	0.45	1.99	<10
P-200-TiW	0.54	1.98	0.54	1.76	10<&<100
P-200-Cu	0.53	2.82	0.54	1.73	10<&<100
P-200-Ni	0.37	3.29	0.39	1.99	<10

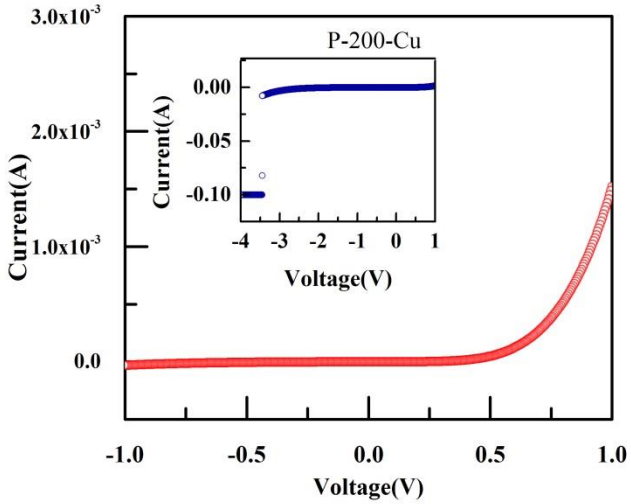

Figure 5.2. Typical *I-V* characteristic curve for PEALD ZnO/Cu Schottky diode. The inset shows the breakdown voltage of the diode.

It is worthwhile to note that a permanent breakdown occurs at 3.45 V for the P-200-Cu as shown in Figure 5.2. Using the method described by Baliga[169], a minimum breakdown field

strength of 2.3 MV cm^{-1} can be calculated, which is among the highest breakdown field strengths reported for ZnO.

Typical normalized *C-V* and *G-V* characteristics are shown in Figure 5.3a-d for Schottky contacts on P-200 ZnO thin films with Ag, TiW, Cu, and Ni contacts. Precaution should be taken in the analysis of doping concentration from the measured *C-V* characteristics. With the presence of the series resistance, the measured capacitance and conductance can deviate from the parallel capacitance with large frequency of the small AC signal as discussed in section 4.3.4. Furthermore, the Keithley 4200 SCS gives valid data only if the device under test (DUT) has an impedance value higher than a specific value. The suggested minimum impedance value is ~100 Ω for the LCR meter in this system[170]. Hence, for the devices with high conductance at both forward and reverse bias voltage, the available valid measurement range is very limited.

The P-200-Ag diode gives relatively high capacitance value and the lowest conductance value. By performing *C-V* analysis in the bias voltage range from -0.2 to -1 V according to section 4.3.3, the doping concentration and the depletion width versus voltage profiles are determined and shown in Figure 5.3e. A consistent doping concentration of 1.8×10^{18} cm^{-3} is obtained for the ZnO thin film. The extrapolated doping concentration data have significant scattering in the large reverse bias voltages region due to the noises from the measurement. The lowest depletion depth of 38 nm obtained here indicating that there is a significant effect of the excess capacitance in addition to the space-charge-region induced capacitance.

The analysis of the *C-V* characteristics for the P-200-TiW diode is performed in the bias voltage range from -0.25 to -0.75 V as there is a preliminary breakdown present at ~-0.75 V. The doping concentration and the depletion width versus voltage are determined and shown in Figure 5.3f. Different from that observed in P-200-Ag, the reasonable probable depletion depth of few

nanometers indicates the contribution of series capacitance is much less in this diode. The extracted doping concentration of the ZnO thin film in this P-200-TiW diode much larger than the Ag one and decreases continuously with increased reverse bias voltage. Since the depletion width decrease with increased reverse bias voltage, Figure 5.3f suggests the doping concentration of ZnO in P-200-TiW is nonuniform and decreases away from the bottom interface, i.e. increases toward the bottom interface. An increasing carrier concentration close to the interface may be resulted from diffusion of titanium and oxygen between the TiW and ZnO layers as well as higher lattice defects. According to H. Kim *et al*[171], oxygen diffuses into the TiW layer and reacts with Ti element since the enthalpies of formation for TiO_2 (ΔH_{TiO_2}=-944 kJ/mol) and TiO (ΔH_{TiO}=-519 kJ/mol) are much smaller than that for ZnO (ΔH_{ZnO}=-350 kJ/mol). GAXRD results discussed in section 3.3 also indicated that Ti diffuses into the ZnO and formed detectable titanium oxide phases in P-200 ZnO thin film.

The analysis of the *C-V* characteristics for the P-200-Cu diode is performed in the bias voltage range from -0.2 to -1 V. The measured conductance for the P-200-Cu diode is comparable to that of the P-200-Ag diode. The doping concentration and the depletion width versus voltage are determined and shown in Figure 5.3g. An almost constant doping concentration of $6x10^{18}$ cm^{-3} is obtained for the ZnO thin film. The smallest depletion depth of 14 nm obtained here indicates effect of series capacitance could be also present for this P-200-Cu diode. From the comparison of the *I-V* characteristics and *C-V* characteristics of these three diodes, we can find that the effect of series capacitance is related to the effect of series resistance on the diode. The effect of series resistance on the diode is Ag>Cu>TiW, the effect of series capacitance on the diode is Ag>Cu>TiW.

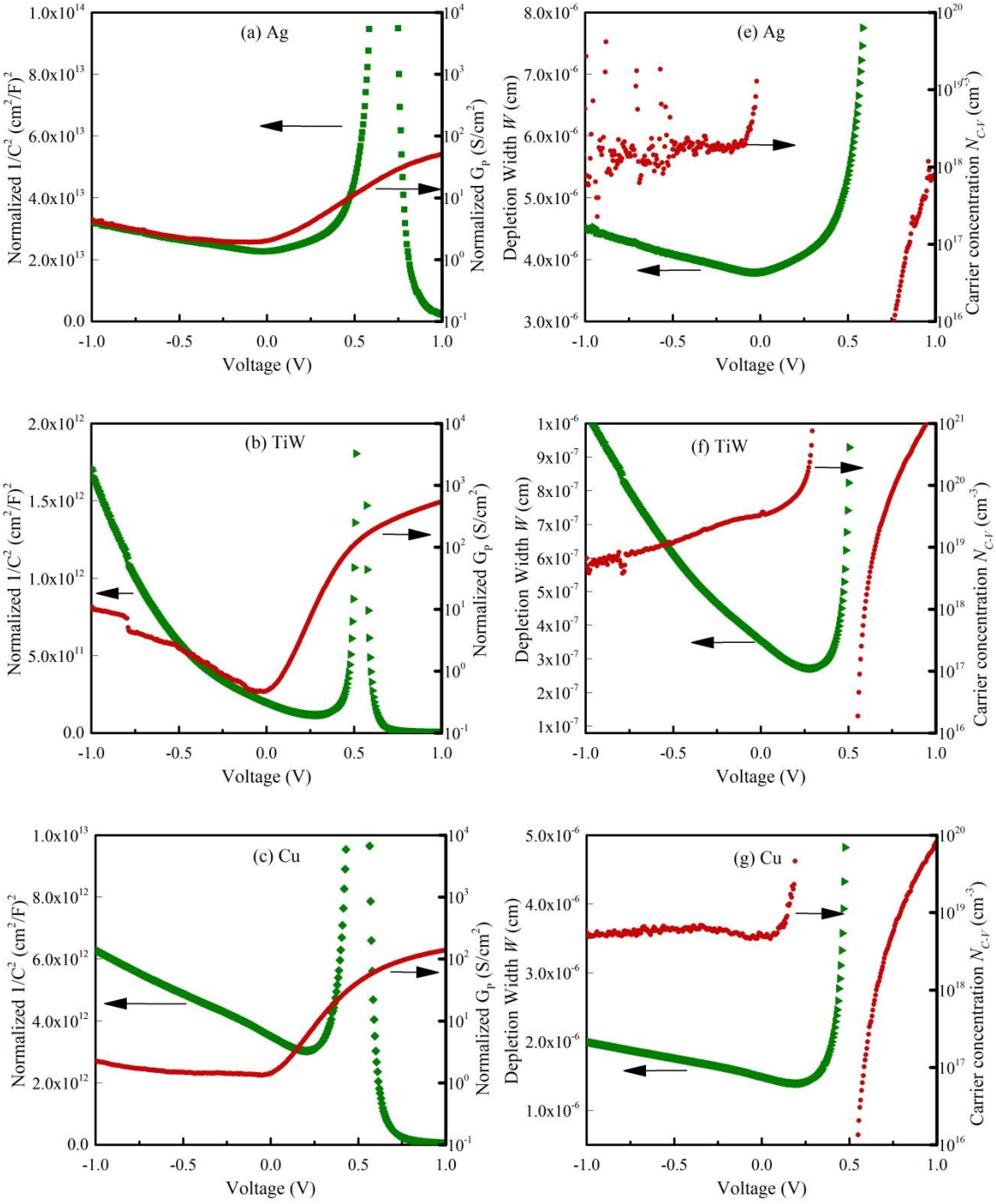
(a) Ag
Normalized 1/C² (cm²/F)²
Normalized G_p (S/cm²)
Voltage (V)
(e) Ag
Depletion Width W (cm)
Carrier concentration N_C-V (cm⁻³)
Voltage (V)
(b) TiW
Normalized 1/C² (cm²/F)²
Normalized G_p (S/cm²)
Voltage (V)
(f) TiW
Depletion Width W (cm)
Carrier concentration N_C-V (cm⁻³)
Voltage (V)
(c) Cu
Normalized 1/C² (cm²/F)²
Normalized G_p (S/cm²)
Voltage (V)
(g) Cu
Depletion Width W (cm)
Carrier concentration N_C-V (cm⁻³)
Voltage (V)

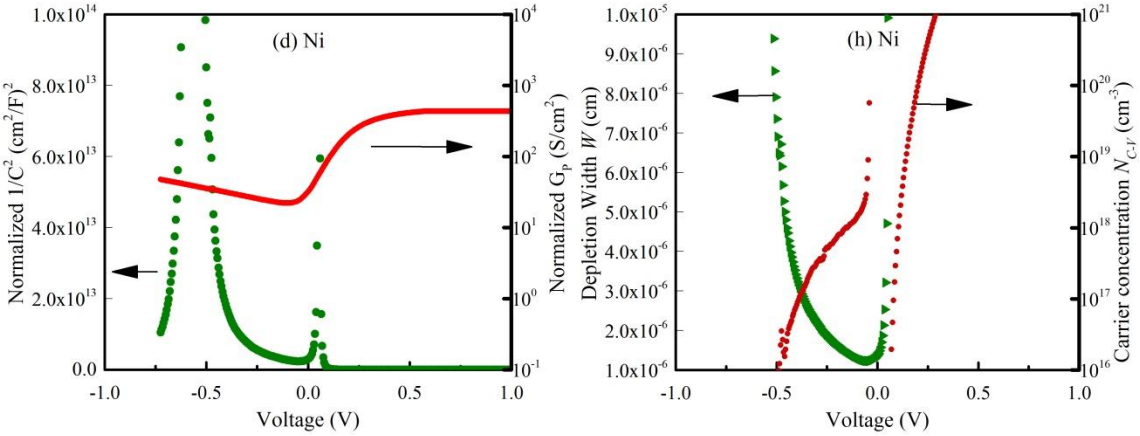

Figure 5.3 Typical normalized *C-V* and *G-V* characteristics (a-d) and extracted depletion width and doping profile versus voltage (e-f) for Schottky contacts with P-200 ZnO thin films.*C-V* measurements are performed at 1 Mhz for Ag and Cu, and 0.5 Mhz for TiW and Ni.

Lastly, for the P-200-Ni diode, the analysis of the *C-V* characteristics is difficult due to its large conductance value. No useful information was extracted since the analysis of the doping profile and depletion depth is unreliable because of the narrow valid voltage range. For all diodes, the extraction of build-in potential from $(A/C)^2$ versus voltage plot cannot be obtained with the approach given in section 4.3.3.1, due to the presence of series capacitance, series resistance, non-uniform doping concentration, etc.

5.2.3 Interface Chemistry of P-200-Cu Contact

As the PEALD process involves exposure of Cu surface to reactive remote oxygen plasma, the chemistry of the Cu/ZnO interface and the crystal structure of the Cu substrate are studied with XPS and GAXRD. It was observed that a thin layer of native copper oxide can later be reduced by the ZnO growth during the ALD process.

Figure 5.4 shows the XRD patterns for the 30 nm P-200 ZnO thin films on Cu substrate at glancing angles of (a) 0.5 degrees and (b) 0.2 degrees. The XRD pattern for T-200 ZnO thin film on Cu substrates performed at glancing angles of 0.2 degrees is shown in Figure 5.4(c). At a

glancing angle of 0.5 degrees, the sub-layer of Cu showed peaks at (111) and (200) planes with a predominant (111) texture well matched with elemental Cu XRD card[172], indicating the polycrystalline nature of the Cu film. The absence of any XRD peaks of copper oxides and of Zn-Cu intermetallic compounds show that interfacial layers of Cu remained elemental after ZnO growth.

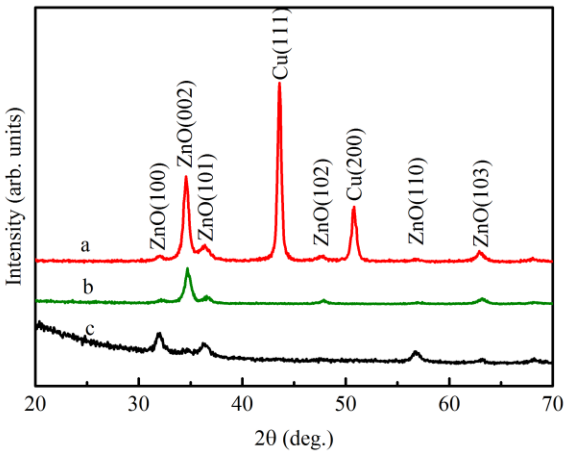

Figure 5.4. GAXRD for as deposited 30 nm PEALD ZnO thin film on Cu substrate with different glancing angle: (a) Theta=0.5 deg. (b) Theta=0.2 deg. (c) as deposited TALD ZnO thin film Theta=0.2 deg.

Figure 5.5 depicts a series of Cu 2p XPS spectra with increasing Ar^+ beam etching time. Cu 2p signal started to appear on the XPS spectrum after 360 s of etching starting from the PEALD-ZnO thin film surface. The etching rate is calculated to be ~3 nm/min. By increasing the etching time with 30 s increments, the Cu 2p signals become stronger without any change in peaks shape or position. After 540 s of etching, the Cu 2p spectra maintained at consistent shape and intensity regardless of any further etching. Many researchers have used the presence of a well-known shake-up satellite located at 943 eV found beside the Cu 2p main peak as an evidence for the presence of CuO[117], which is not observed in our sample, indicating the lack of CuO presence at the interface. It was also reported that there is very little Cu $2p_{3/2}$ binding

energy (BE) shifted (~0.4 eV) between Cu_2O and Cu metal[173], leading to the difficulty in chemical state differentiation by XPS only. The series of Cu 2p spectra showed a consistent Cu $2p_{3/2}$ binding energy of 932.6 eV agreed with the standard value reported for Cu metal[174]. The scans from the top layers has broader peaks can be attributed to the very thin thickness as well as the potential presence of Cu_2O. Cu LMM X-ray generated Auger LMM spectra (XAUS) is typically used to distinguish the Cu chemical state due to the distinct chemical shifts between copper metal and Cu(I) oxide. Although Cu LMM XAUS was not acquired here, considering the atomic composition ratio of Cu, Zn and O shown in section 3.4, it is reasonable to suggest that there is not significant Cu_2O present at the interface.

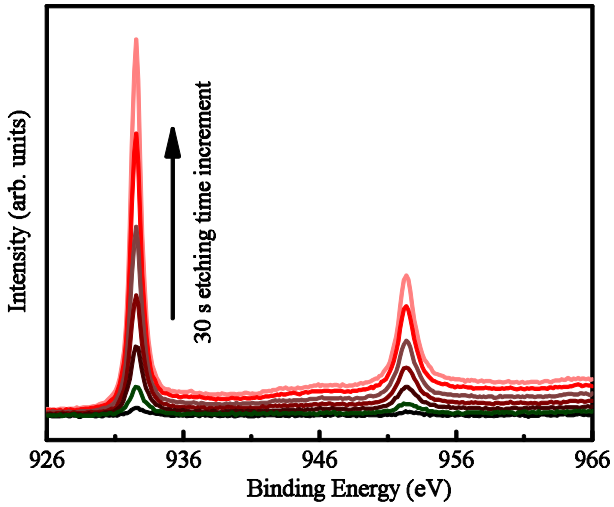

Figure 5.5. Series of Cu 2p XPS peaks detected along *in-situ* Ar^+ beam etching on 30 nm PEALD ZnO/Cu sample. Cu 2p peaks started to appear at 360 s etching time (the bottom first spectrum in the figure). XPS scan was performed with every 30 s etching from 360 s to 540 s.

However, XPS study of the Cu substrate surface before the ZnO deposition exhibited a typical Cu 2p spectrum for native Cu oxide with the well-known shake-up satellite as shown in Figure 5.6, suggesting that the native copper oxide at the surface was reduced in the ZnO deposition process[117,175]. This is consistent with the fact that the oxidation of Zn is preferred due

to the Gibbs free energy formation of ZnO ($\Delta_f G^o_{ZnO}$ = -320.52 kJ mol^{-1}) is more negative than that of CuO ($\Delta_f G^o_{CuO}$ = -129.7 kJ mol^{-1}) and Cu_2O ($\Delta_f G^o_{Cu2O}$ = -149.kJ mol^{-1})[176].

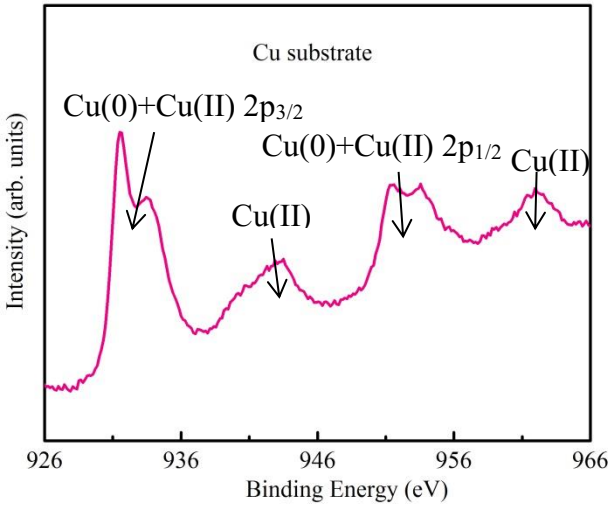

Figure 5.6. XPS spectrum for Cu substrate before ZnO growth shows the Cu surface has native oxidation.

5.2.4 Interface Chemistry of P-200-TiW Contact

A series of high resolution XPS spectra of P-200-TiW sample are used to determine the material stoichiometric of ZnO respect to a continuously etching time. The atomic percentage of each element versus etching time, i.e., depth profile of the sample is shown in Figure 5.7. The XPS peaks from Zn2p, O1s, C1s, Ti2p and W4f are used for the calculation of atomic percentage. The P-200-TiW shows an O-rich interface due to the oxidation of substrate surface. The oxygen composition profile with a tail into the substrate indicates the presence of oxides in the substrate, which are further verified by the chemical state study of the Ti and W.

Figure 5.8 depicts a series of W4f XPS spectra with increasing Ar^+ beam etching time. W4f signals started to appear on the XPS spectrum after 135 s of etching starting from the PEALD-ZnO thin film surface. By increasing the etching time with 45 s increment steps, the W4f signals become stronger with a transition of chemical state as seem from the change of peak

shape or position shifted. The first two scans on the interfacial layers indicate the presence of tungsten oxide in the interface, which vanishes when etching into deeper layers[177]. After 270 s of

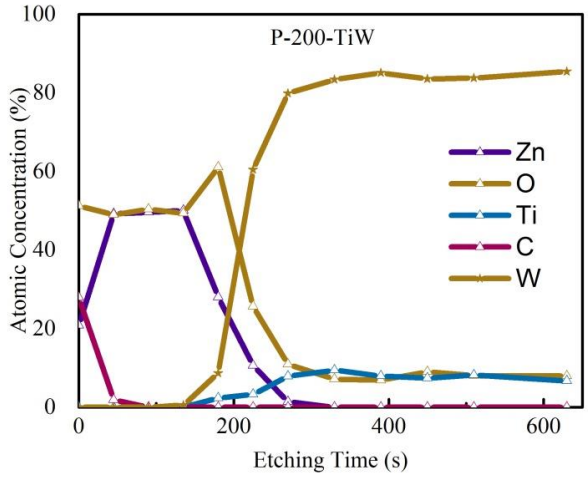

Figure 5.7. The depth profile for P-200-TiW shows the stoichiometric composition of the sample with increasing etching depth.

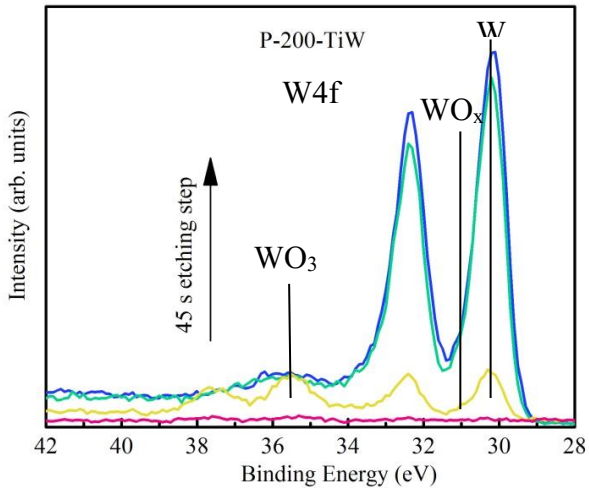

Figure 5.8. A series of W4f XPS spectra detected along *in-situ* Ar^+ beam etching on P-200-TiW sample. W4f peaks started to appear at 135 s etching time (the first bottom spectrum). XPS scan was performed with every 45 s etching steps from 135 s to 270 s.

etching, the W4f spectra maintained at consistent shape and intensity regardless of any further etching. Ti2p spectra also show a transition of chemical states from the interface to deeper inside layer as shown in Figure 5.9[117]. In the interface layers, Ti(IV) chemical states is detected locating

at ~458 eV binding energy, which vanishes when etching into deeper layers. An component analysis for the Ti2p spectra from the scan after 450 s etching duration (shown in Figure 5.9) indicates the existing of Ti(II) together with majority elemental Ti(0) which coincides the presence of oxygen in the substrate of TiW in Figure 5.7.

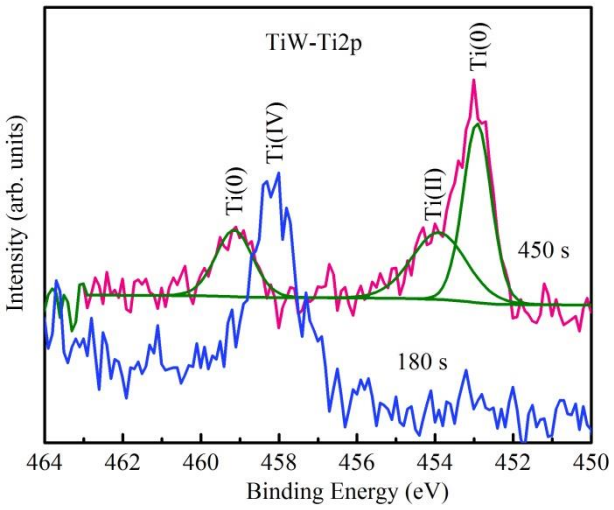

Figure 5.9. Ti2p spectrum after 180 s etching and 450 s etching. The component analysis of the 450 s spectrum is performed and shows more bond states of Ti2p.

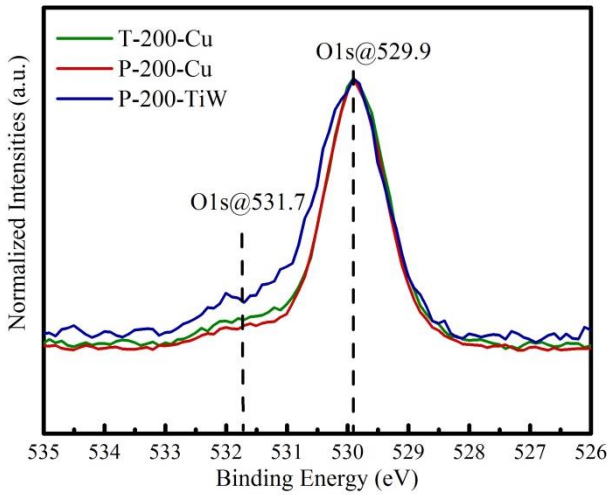

Figure 5.10 High resolution XPS spectra of O1s for P-200-TiW, compared to that of P-200-Cu and T-200-Cu.

In addition, Figure 5.10 shows the high resolution XPS spectra of O1s in ZnO layers with the dominant peak at 529.9 eV and a shoulder peak at 531.7 eV. The *at.* % of OH chemical state

out of the total O for P-200-TiW is calculated to be 19.3%, which is much higher than the P-200-Cu of 10% (see section 3.4). The higher hydrogen impurity in P-200-TiW agrees with the observation of higher doping concentration in this device from C-V characteristics discussed in section 5.2.1.

5.3 STUDY II: OPTIMIZATION OF CU SCHOTTKY NANODIODES

Table 5.3. Schottky parameters of Cu/ZnO diodes with various deposition temperatures, oxygen plasma pretreatment durations, and/or annealing temperatures.

Recipe	Remote plasma (s)	Annealing T (K)	$q\Phi_B$ (eV)	n
P-100	5 s O_2	/	0.55	2.3
P-130	5 s O_2	/	0.56	2.6
P-130	5 s O_2	373 K	0.56	2.6
P-130	5 s O_2	473 K	0.57	2.6
P-130	5 s O_2	573 K	0.60	2.4
P-200	5 s O_2	/	0.54	2.7
P-200-2	15 s O_2	/	0.58	2.7
P-200-3	30 s O_2	/	0.56	2.6

The effects of deposition temperature and plasma treatments on the substrate surface prior to ZnO growth are studied for Cu-ZnO system. Cu metallization is applied on a set of ZnO thin films fabricated by PEALD with deposition temperatures of 100 °C, 130 °C, and 200 °C, referring to as recipes P-100, P-130 and P-200 respectively in Table 5.1. The Cu surface for each sample in this set is treated with 5 s ICP oxygen plasma in situ (see section 2.2.2) before the ZnO deposition. Another set of Cu/ZnO contacts with ZnO thin films grown by PEALD with the same deposition temperature of 200 °C but the Cu contacts were exposed to oxygen plasma with pretreatment duration of 5 s, 15 s and 30 s, referring to as recipes P-200, P-200-2, and P-200-3 respectively in Table 5.1. The thermal stability of Cu contact with P-130 ZnO is explored by annealing the same sample in forming gas (with a formulation of 5% hydrogen in nitrogen) for 5

mins at 100 °C, 200°C and then 300 °C. The Schottky parameters, including effective barrier height and ideality factor, for all diodes are obtained and summarized in Table 5.3. The Φ_B and n are extracted from forward bias region in the range of 0.1 V - 0.3 V according to eq 4.9 and eq 4.10.

5.3.1 Cu Contacts to ZnO with Various Deposition Temperatures

I-V curves for devices with P-200, P-130, and P-100 ZnO thin films are shown in Figure 5.11. All devices have a similar Schottky barrier (Φ_B) in the range of 0.51-0.55 eV with an increasing trend when the deposition temperature decreases, a similar n in the range of 1.1-1.13 with a decreasing trend respect to decreasing deposition temperature. The devices also have increasing on/off ratio at ±1 V as deposition temperature decreases. As can be seen from Figure 5.11, the on/off ratio of the sample with 100 °C deposition temperature is increased by an order of magnitude compared to that of 200 °C deposition temperature. The values of effective Schottky barrier height are slightly different. The value of the ideality factor larger tends to increase at higher deposition temperature. A hypothesis taking into account the presence of interfacial layer of oxide is proposed following for the obtained ideality factor values.

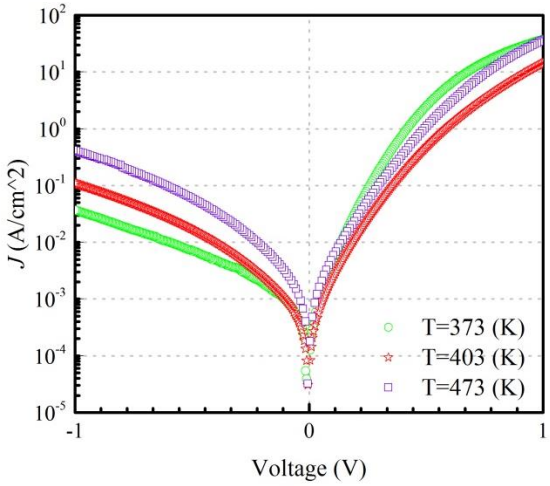

Figure 5.11. *I-V* curves of Cu Schottky contact to P-100, P-130 and P-200 ZnO thin films.

A complete description for the *J-V* characteristics requires taking into account quantum mechanical effects (QME) [178]:

$$J = A^{**}T^2\, exp(-q\varphi_B/kt)\,[exp(qV/kt) - 1] \qquad (5.1)$$

Where

$$A^{**} = f_p f_Q A^*/\left(1 + f_p f_Q\, v_R/v_d\right) \qquad (5.2)$$

where φ_B is Schottky barrier potential, f_p is the probability of emission over the potential maximum, f_Q is the ratio of total current flow with QME to the thermionic current flow without these effects, A^* is the Richardson constant only depending on the effective mass of materials, A^{**} is the apparent Richardson constant depending on practical factors, v_R is thermal velocity constant, and v_d is an effective diffusion velocity. *n* is originally defined as:

$$n \equiv \frac{q}{kT}\frac{dV}{dlnJ} \qquad (5.3)$$

for $V > 3kT/q$,

$$n \approx \left[1 - \frac{kT}{2qV_{bi}}\frac{d\, lnA^{**}}{d\ln\xi} - \frac{\Delta\varphi_{IF}}{4V_{bi}} + \frac{d\varphi_B}{d\xi}\frac{\xi}{2V_{bi}}\right]^{-1} \qquad (5.4)$$

where

$$\xi = (2qN_d V_{bi}/\varepsilon_s/\varepsilon_0)^{1/2} \quad (5.5)$$

and

$$V_{bi} = \varphi_B - V - \frac{kT}{q}[1 + ln(N_c/N_d)] \quad (5.6)$$

If the $\frac{kT}{2qV_{bi}}\frac{d\ lnA^{**}}{d\ln\xi}$ and $\frac{\Delta\varphi_{IF}}{4V_{bi}}$ terms in eq 5.4 is negligibly small, the deviation of n from unity is dominated by $\frac{d\varphi_B}{d\xi}$. The quality of $\frac{d\varphi_B}{d\xi}$ is related to the interface defects density and interfacial layer thickness in the model proposed by Crowell *et al*.[179]:

$$\frac{d\varphi_B}{d\xi} = -\left[\frac{qD_s}{\varepsilon_s} + \frac{\varepsilon_i}{\theta\varepsilon_s}\right]^{-1} \quad (5.7)$$

where θ and ε_i, is the thickness and permittivity of the interfacial layer respectively, D_S is surface defects density near the fermi level at the interface of the semiconductor. According to eq 4.39, $\xi/2V_{bi} \approx {W_d}^{-1}$, when $d\varphi_B/d\xi$ is comparable with the width of the semiconductor depletion region W_d, large deviation of n from unity would occur according to eq 5.4. For example, the W_d for the P-100-Cu at ~0.25 V is ~10 nm obtained from C-V characteristics as shown in Figure 5.12d, the n for the P-100-Cu of 2.3 could be obtained with $(d\varphi_B)/d\xi \approx$ -5.7. The value -5.7 of $(d\varphi_B)/d\xi$ can be induced by either a surface state density of ~10^{13} states/cm^2/V or a thin interfacial layer of 2 nm with $\varepsilon_{ZnO}/\varepsilon_{CuO} \approx 3$[180]. According to eq 5.4 and eq 5.7, the larger value of ideality factor for P-200-Cu could be due to slightly increased thickness of interfacial layer, which is thermodynamically plausible for the reaction of Cu oxidation.

The *C-V* and *G-V* curves for devices with P-100, P-130 and P-200 ZnO thin films in are shown Figure 5.12 (a) to (c). Conductance at reverse bias voltages decreases with decreasing synthesis temperature from 200 to 100 °C, which is in accordance with the observation of

reduced leakage current in *I-V* characteristics. The effective carrier concentration $N_{C\text{-}V}$ data extracted according to eq 4.48 for P-100 as shown in Figure 5.12 (d) has significant scattering. Hence it is hard to use the $N_{C\text{-}V}$ to make a comparison of the doping concentration in the ZnO films. In the other hand, the depletion width *W* depends on both bias voltage and doping concentration according to eq 4.49. Under the same bias voltage, e.g. -1 V, assume the effect of series capacitance and non-ideal factors on the *C-V* characteristics are negligible, a comparison of *W* at -1 V shows the P-100 has slightly larger *W*, i.e., lower doping concentration.

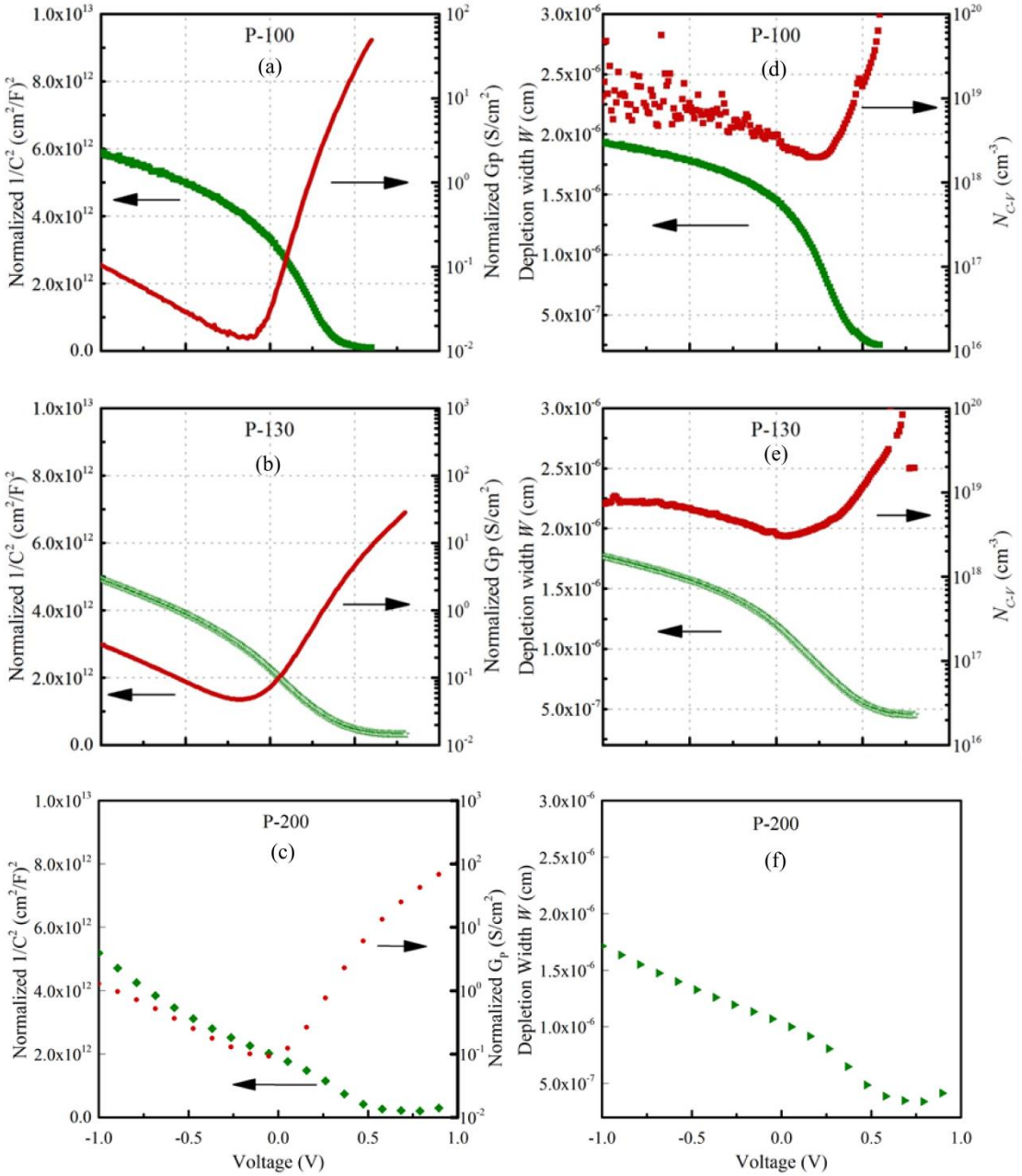

Figure 5.12. *C-V* and *G-V* curves of Cu Schottky diodes with P-100 (a), P-130 (b) and P-200 (c) ZnO with their respective depletion width *W* and effective doping concentration $N_{C\text{-}V}$ *versus* voltage characteristics for (d) P-100-Cu, (e) P-130-Cu and (f) P-200-Cu. All measurements were performed at a frequency of 100 kHz.

Figure 5.13 shows the *C-f* curves for P-130 and P-200 ZnO device. The frequency-dependence capacitances for both devices suggest the existence of interface defects according to section 4.3.4. The reduced frequency-dependence with larger reverse bias voltage could be

attributed to the reduction of effective carrier contributed from interface defects. This observation indicates that the energy distribution of interface defects in the bandgap is not uniform and decreases with increasing energy respect to the minimum conduction band as the energy level of the interface states detected is related to the bias voltage according to eq 4.60.

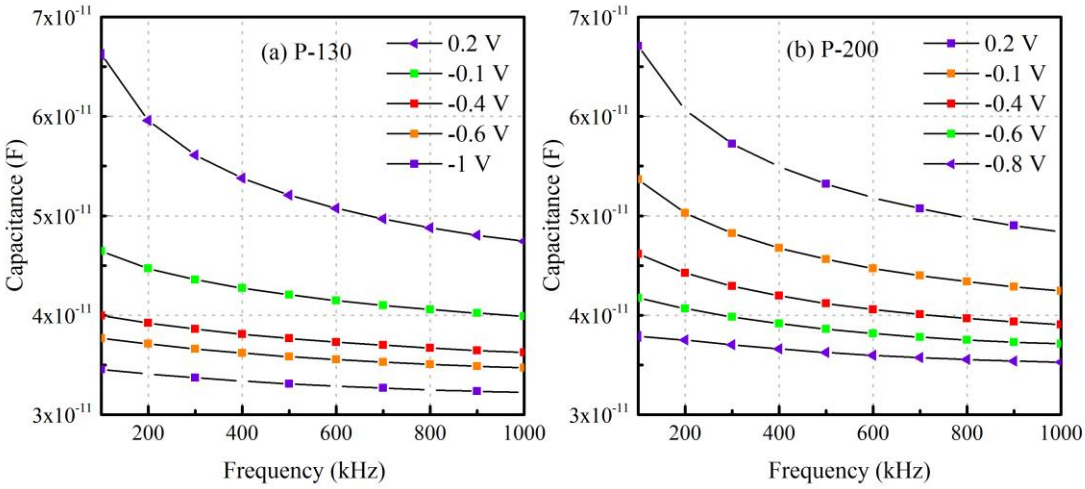

Figure 5.13. *C-f* curves of Cu Schottky contacts with P-130 (a) and P-200 (b) ZnO. Both devices show frequency-dependence nature indicating the existence of interface defects.

5.3.2 Cu Contacts to ZnO with Various Pretreatments Duration

The *I-V* characteristics of the P-200 ZnO/Cu devices with Cu substrates pretreated with oxygen plasma at various durations are shown in Figure 5.14. The performance of the devices is affected by the interface conditions altered by the duration of the plasma cleaning process. Both devices with 15 s and 30 s pretreatments show significantly increased series resistance from the *I-V* characteristics, which can be due to the oxidation of Cu substrates. Although the device with 15 s pretreatment shows the smallest leakage current which is mostly likely due to its highest series resistance, the rectifying behavior is not improved. The decrease of the series resistance

for the device with 30 s pretreatment suggests that the resistivity of the Cu substrate is not proportional to the pretreatment duration.

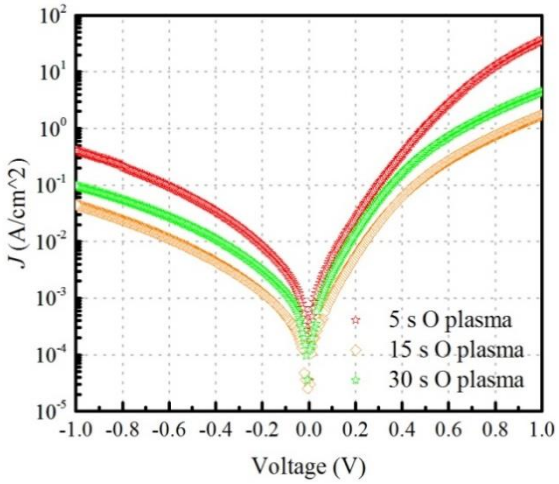

Figure 5.14. *I-V* curves for P-200 ZnO devices pretreated with oxygen plasma duration of 5 s, 15s, and 30 s.

Figure 5.15 shows the *C-V, G-V,* depletion width *versus* voltage and doping concentration *versus* voltage curves for P-200 ZnO/Cu devices with various oxygen plasma pretreatment durations. The capacitance decreases in the order of 5 s > 30 s > 15 s pretreatments as shown in Figure 5.15a and their respective minimum depletion width increase in the order of 5 s < 30 s < 15 s pretreatments as shown in Figure 5.15b. According to eq 4.55, it suggests the effect of series resistance is significant on Cu devices in the order of 15 s > 30 s >5 s pretreatments, which agrees well with the *I-V* characteristics. The doping concentration can be estimated by the slope of $1/C^2$-V plots with 5 s > 30 s > 15 s pretreatments as shown in Figure 5.15a provided the series resistance and parallel conductance is independent of the applied bias voltage.

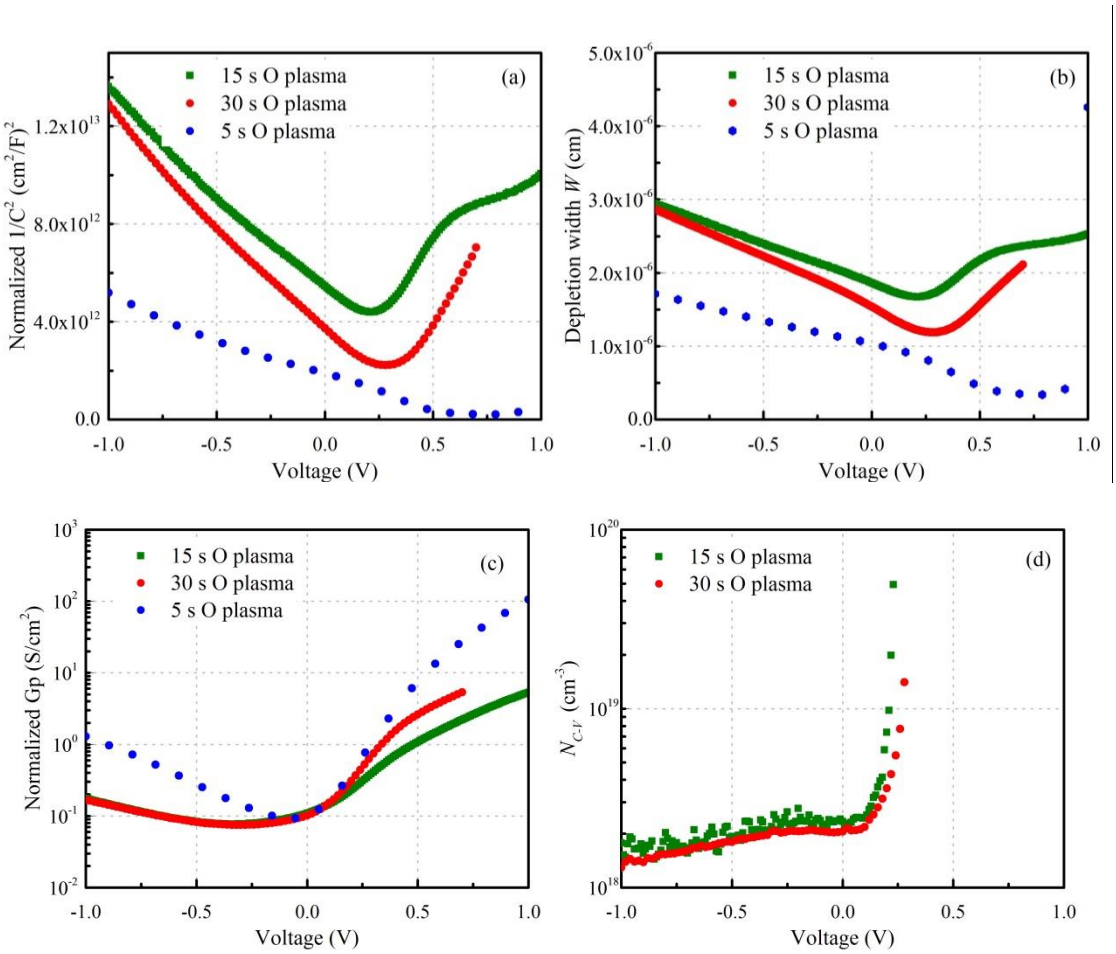

Figure 5.15. (a) *C-V,* (b) depletion width *versus* voltage, (c) *G-V*, and (d) doping concentration *versus* voltage curves for P-200-Cu devices pretreated with various oxygen plasma duration. The measurements were all performed at 100 kHz.

In this case, the depletion width is improper to be used as a clue for the doping concentration. The extracted effective carrier concentration $N_{C\text{-}V}$ is neither reliable before the contribution of other elements into the measured capacitance can be identified. Overall, longer oxygen plasma pretreatment on Cu substrate didn't show any beneficial impact on the device to this end. Long oxygen plasma pretreatment increases the series resistance which is harmful for the turn on behavior of the diode. Thus, the oxygen plasma pretreatment duration should be kept short enough to avoid over-oxidation of the Cu substrates.

5.3.3 Cu Contacts to ZnO with Various Annealing Temperatures

The thermal stability of the P-130-Cu contact is studied by post-deposition annealing for 5 mins in forming gas ambient to a maximum temperature of 573 K (300 °C) beyond which the device breaks down permanently. It is of interest to find that the rectifying behavior is improved with reduced reverse current by annealing at 573 K (300 °C), while the series resistance of the diode varies very little from the large forward bias *I-V* curves as shown in Figure 5.16. This improvement of rectifying behavior can be attributed to the increase of Φ_B as shown in Table 5.3.

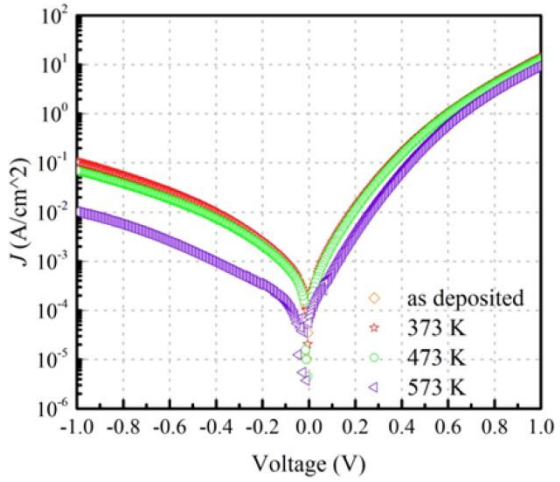

Figure 5.16. *IV* characteristics of P-130-Cu ZnO Schottky diodes measured as deposited and after annealed at 373 K (100 °C), 473 K (200 °C), and 573 K (300 °C).

According to section 4.4.2, with the presence of thermionic field emission, the Φ_B and n is related to the doping concentration in Schottky contacts on highly doped semiconductors. The higher doping concentration will lead to further lowering of the Φ_B and increasing of n. The *C-V* measurements following can provide the doping concentrations in the ZnO thin film, which agree well with the observation from *I-V* characteristics.

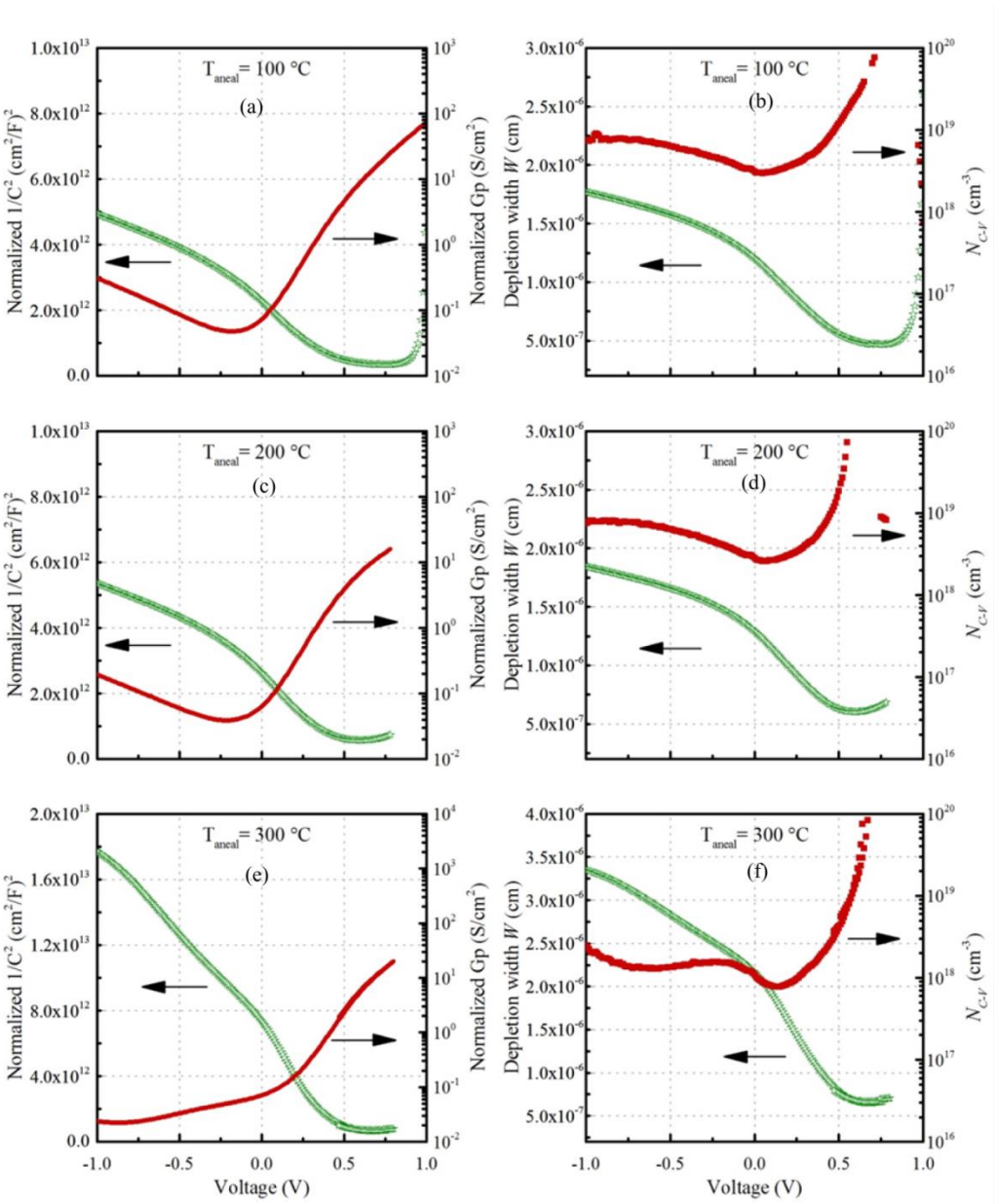

Figure 5.17. *C-V* and *G-V* characteristics for annealing temperature T_{anneal}=100°C (a), T_{anneal}=200°C (c), and T_{anneal}=300°C (e); Depletion width *W versus* voltage and doping concentration $N_{C\text{-}V}$ *versus* voltage curves for T_{anneal}=100°C (b), T_{anneal}=200°C (d), and T_{anneal}=300°C (f). All the measurements were performed at 100 kHz for P-130-Cu devices.

Comparisons of the *C-V, G-V,* depletion width *versus* voltage, and doping concentration *versus* voltage curves is shown in Figure 5.17. The smallest detectable depletion width of the annealed diodes remains similar after annealing up to 573 K (300 °C), which suggests the effect of series capacitance is little on the *C-V* curves for all annealed samples. The extracted effective

doping concentrations $N_{C\text{-}V}$ for the samples annealed under 473 K (200 °C) as shown in Figure 5.17 (b) and (d) are similar to the as deposited sample (see Figure 5.12e). While the sample annealed at 573 K (300 °C) shows lower doping concentration of ZnO thin film. The potential mechanism for the decrease of doping concentration with annealing is the eviction of mobile dopants like hydrogen, which is proved to be present in P-200-Cu sample (see Figure 5.10).

5.4 STUDY III: P-50 SCHOTTKY NANODIODES

In our recent study reported by Dr. Triratna Muneshwar[96], for ALD growth of ZnO at deposition temperature (T_{sub}) ≥ 60 °C, precursor decomposition during growth was suspected which led to increasing in doping concentration and reduction in resistivity in deposited ZnO thin film with increasing deposition temperature T_{sub}. The speculation was confirmed by the self-limiting ZnO PEALD growth observed at T_{sub}=50 °C with respect to both DEZ pulse duration and O_2-plasma exposure duration. Similar trend for doping concentration and film resistivity respect to deposition temperature was also observed by Guziewicz *et al*[97,99]. The resistivity the P-50 ZnO thin film is determined to be 211 Ω-cm from van-der-Pauw sheet resistance measurement with the sample grown on bare SiO_2/ Si wafer.

Schottky diodes with P-50 ZnO were investigated on a series of Schottky metals including Cu, Ni, Pt, Au, Cr, Ru and TiW with the other electrode kept as Al/Au stacks for every diode. Substrates were pre-cleaned using 10 s Ar plasma prior to ZnO deposition. To avoid non-uniform surface oxidation of the Pt layers that would lead to more serious barrier potential inhomogeneity problem during the initial oxygen (O_2) plasma cycles in ZnO deposition, 1.8 nm-thick T-50 ZnO layer was deposited, it was then followed by depositing 30 nm-thick P-50 ZnO. The resultant contact type of each device is determined by *I-V* measurements and summarized in

Table 5.4 with either ohmic (linear) or Schottky (rectifying). All of the devices show rectifying behavior except the Au contacts. The ohmic behavior of Au contacts is attributed to the poor thermal stability as discussed in section 5.2.1.

Table 5.4 Summary of P-50 Schottky diodes performance

Contact Metal	P-50
Au	ohmic
Pt	Schottky
Cr	Schottky
TiW	Schottky
Cu	Schottky
Ru	Schottky
Ni	Schottky

5.4.1 Aging-related Effect on P-50 Schottky Nanodiodes

The aging-related effect on P-50 Schottky diodes are studied by *I-V* measurements. Figure 5.18a-f shows the *I-V* characteristics measured from the first day to 60th days after fabrication for Cr, TiW, Cu, Ru and Ni Schottky diodes while the Pt Schottky diodes are tracked till 250 days after fabrication. The Pt contacts show a large increase in rectifying ratio @ ±1 V from 5x10^4 to 10^6 resulted from the decrease of leakage current as they age. Cu contacts also show a small increase as they age while Cr and Ru contacts show relatively good stability over time. The TiW and Ni show obvious degradation in rectifying ratios as they age.

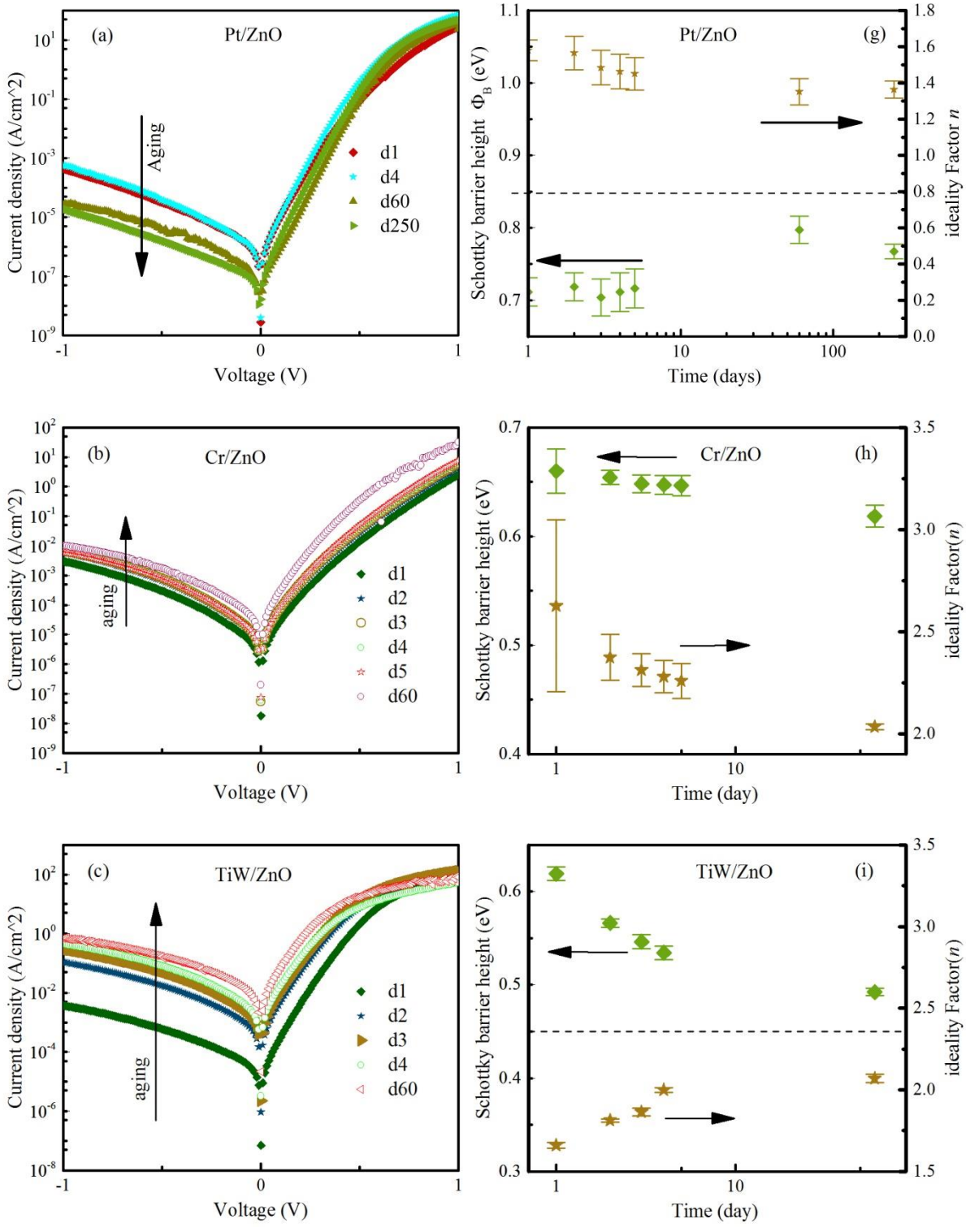
(a)
Pt/ZnO
Aging
d1
d4
d60
d250
Current density (A/cm^2)
Voltage (V)
(g)
Pt/ZnO
Schottky barrier height Φ_B (eV)
ideality Factor n
Time (days)
(b)
Cr/ZnO
aging
d1
d2
d3
d4
d5
d60
Current density (A/cm^2)
Voltage (V)
(h)
Cr/ZnO
Schottky barrier height (eV)
ideality Factor(n)
Time (day)
(c)
TiW/ZnO
aging
d1
d2
d3
d4
d60
Current density (A/cm^2)
Voltage (V)
(i)
TiW/ZnO
Schottky barrier height (eV)
ideality Factor(n)
Time (day)

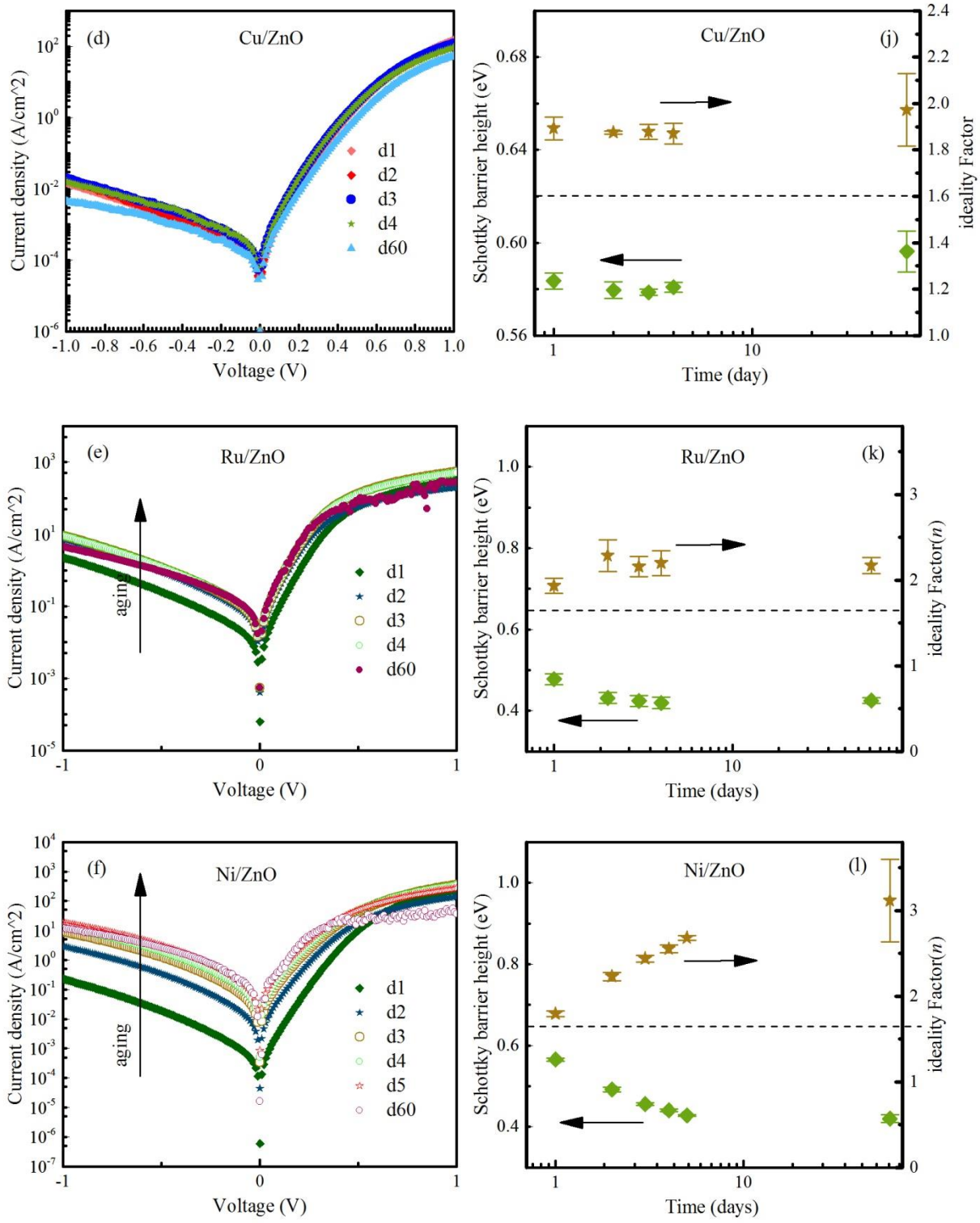

Figure 5.18. (a-f) aging related *I-V* curves of P-50 Schottky diodes with different bottom electrodes; (g-l) Extracted Schottky barrier heights and ideality factors from the forward *I-V* curves for the respective diodes.

If the aging effect is introduced by the interface chemical reaction, then the thermal stability of the contacts can be extrapolated based on the aging behavior since interface chemical reaction is typically as a result of thermal degradation. Figure 5.18 (g) to (l) shows the evolution of Schottky parameters Φ_B and n extracted from forward I-V plots using eq 4.9 and eq 4.10, respectively. The decrease (or increase) of ideality factors and increase (or decrease) of barrier height correspond to improved (or degraded) rectifying behaviors of the respective diodes. The aging effects in P-50 Schottky contacts may be attributed to the diffusion of ambient oxygen to the Schottky contact interfaces which subsequently annihilates the interface oxygen vacancy defects[50]. For ZnO, the role of oxygen vacancies has been studied extensively[18,110,112,113]. These studies showed that the oxygen vacancies V_O are preferred to form in Zn-rich condition and have a deep transition level located at approximately 0.7±0.2 eV under the conduction band E_C. Such a deep transition level implies V_O defects are unlikely to contribute to free carrier concentration in ZnO at room temperature. However, they can behave as generation-recombination (G-R) centers in the space charge region for G-R current transport, traps assisting tunneling current transport[116], or high density interface defects pining the fermi levels across the contacts. The Φ_B deviates from the Schottky-Mott model and Fermi level pining at about V_O energy level are commonly observed for ZnO and typically attributed to interface defects[125].

The self-healing of the interface V_O defects during aging is speculated based on the observation of increasing Φ_B as the device ages. The source of oxygen for the self-healing could be from absorption and diffusion of ambient molecular oxygen to the Schottky interface in aging[50,181]. A model to describe the aging effect is proposed and shown in Figure 5.19. A schematic diagram of the newly-fabricated Pt/ZnO/Al Schottky diode (not scaled) and its respective band structure are shown in Figure 5.19 (a) and (c) respectively. The model assumes (i)

the ZnO layer has a uniformly lower doped region close to the Pt electrode and a degenerately doped region close to the Al electrode; (ii) there are interface states heavily populated around V_O (+2, 0) energy level; and (iii) there are volatile shallow donors like hydrogen, hydroxyl, hydrocarbons, etc. existing in the ZnO layer[112]. The diode's schematic diagram and its respective band structure after aging are shown in Figure 5.19 (b) and (d) respectively.

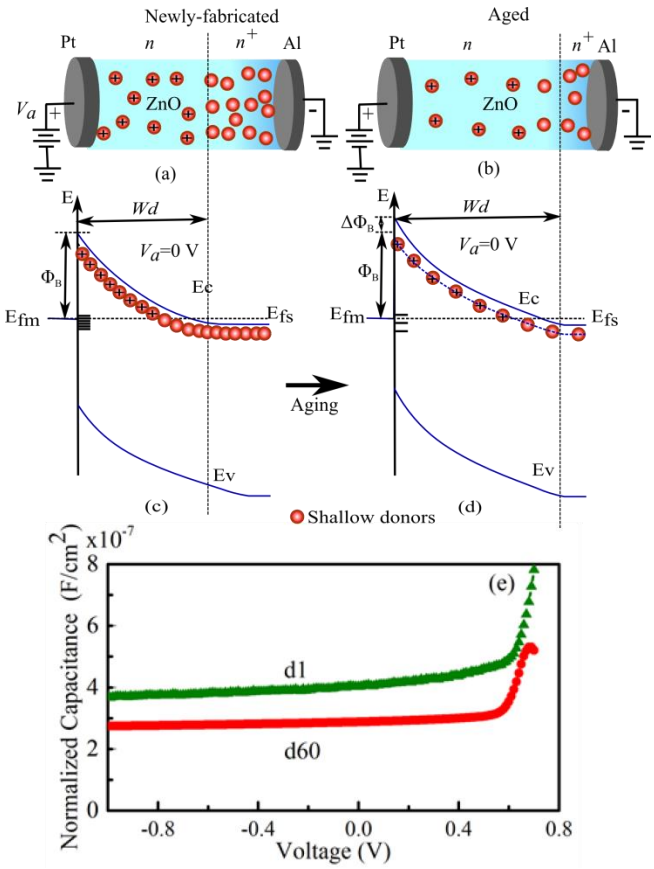

Figure 5.19. Non-scaled schematic diagrams of (a) the newly-fabricated and (b) the aged Pt/ZnO/Al diodes, respectively. V_a is applied voltage to the anode (Pt), n is the doping concentration of the uniformly doped region and n^+ is the doping concentration of the degenerately doped region close to the Al contact; (c) and (d) are band structures of the newly-fabricated and aged Schottky contacts at 0 V bias. E_{fm} and E_{fs} are the fermi levels of Pt and ZnO respectively, E_C and E_V are the conduction band minimum and valence band maximum in ZnO, *Wd* is the depletion region width; (e) A comparison of normalized *C-V* characteristics from 1st day (d1) and 60th day (d60).

The aged diode has relatively less interface defects density and volatile dopants concentration. A spontaneous annihilation of the interface defect states is suspected by absorption and diffusion of ambient molecular oxygen into the Schottky interface as the device age, the formation of molecular oxygen O_O in n-type ZnO is energetically more favorable compared to oxygen vacancy V_O and oxygen interstitial O_i[31]. This annihilation reduces the interface defects density and consequently reduces the fermi level pinning and enhances the Φ_B by $\Delta\Phi_B$. Another possible mechanism involved in this aging behavior is the decrease of volatile shallow donors (mainly hydrogen) as the transition of H^+ to H_2 molecule is energetically preferred in high doped ZnO[30], which can decrease the tunneling possibility and reduce the Φ_B lowering by thermionic field emission process[144], and consequently increase the Φ_B. Both the increase of Φ_B and decrease of shallow dopants can result in larger depletion region which is confirmed by the capacitance-voltage (*C-V*) measurements before and after aging as shown in Figure 5.19e.

5.4.2 The Analysis of Series Resistance in Pt/ZnO Contact

Series resistance (*Rs*) is one of the important parameter that needs to be considered in the analysis of Schottky diodes. The analysis of *Rs* is carried out in this section for the P-50-Pt diode with the best performance. As all devices use the same ohmic electrode-Al/Au, the series resistance behavior due to the top ohmic contact in the P-50-Pt diode is representative for all devices. At large forward voltages when the *I-V* characteristics are significantly influenced by *Rs*, the semi-log *I-V* plot deviates from linearity with a voltage deviation $\Delta V = IR_S$ as shown in Figure 5.20(a), which gives a simple approach to determine $R_S = \Delta V / I$ at a particular current (refer to section 4.3.1.2.1). The diode impedance $Z = dV/dI$ is also derived and shown in the right axis of Figure 5.20(a). It is found that R_S extracted from *I-V* curve is not a constant but

continuously decreasing with increasing applied bias voltage with a minimum R_S of 90 Ω at 1V. Other methods to extract *R*s as discussed in section 4.3.1.2 assuming a constant series resistance present in the diode according to eq 4.17 and eq 4.27, making them unsuitable for the case here since neither the d*V*/d(ln*I*) versus *V* plot nor the H(*I*) versus *V* plot show linearity as can been seen in Figure 5.20b and 5.20c. Similar phenomena were observed by other researchers using Al as the cathode contacts[182,183].

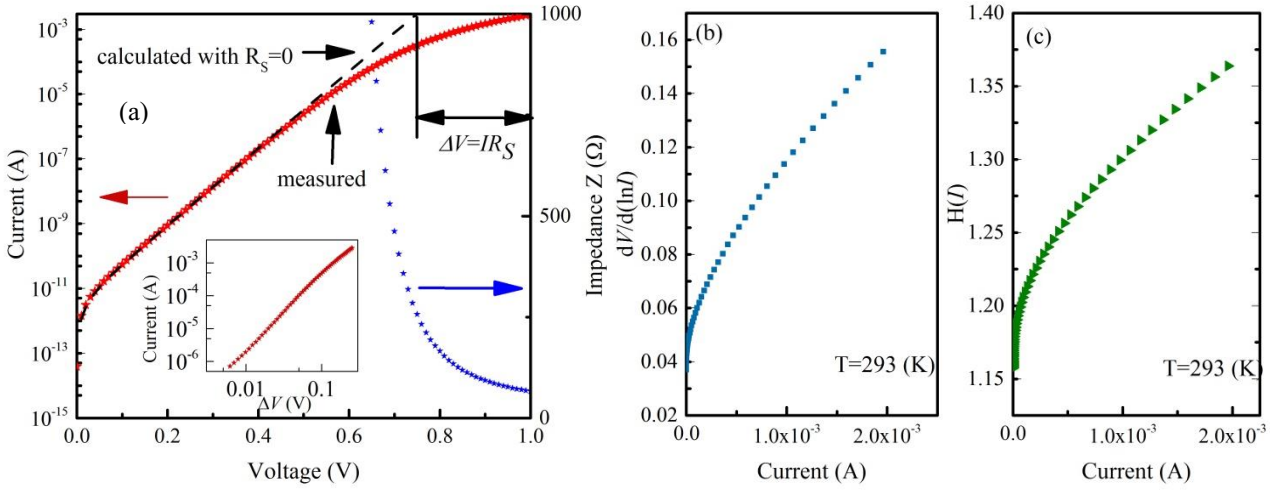

Figure 5.20. (a) A typical semi-log scale I-V characteristic of a Pt/ZnO Schottky diode, right y-axis shows the diode impedance, the dash line plots the simulated current based on thermionic model assuming R_S=0 Ω ; (b) d*V*/d(ln*I*) versus *I* plot; (c) H(*I*) versus *I* plot.

Several underlying mechanisms might be responsible for the variation of *Rs*: first of all, in the general for metal-semiconductor contact, the neutral charge region (NCR) expands while the depletion width narrows simultaneously with increasing forward bias voltages, leading to an increasing of *Rs*. However, this is opposite to the trend observed from the *I-V* characteristics here. Secondly, larger bias currents may change the series resistance by heating the substrate, which is unlikely a concern for our case since the diodes operate at low power in our measurements. For Schottky diodes with large barriers, low doping and thin layers, increasing minority carriers injection ratios under forward bias voltages can lead to a significant change of the substrate

resistance due to conductivity modulation[184–186]. It is noted that the log (ΔV) versus log (I) plot has almost linear relationship with a slope of 2.4 as shown in the inset of Figure 5.20a. The space charge limited current transport mechanism is typically attributed for power law relationship between current and voltage at high injection[187]. The space charge limited conduction can be arisen from the interface oxide layer as a results of the interaction between the top Al layer and the ZnO surface layer[188].

5.4.3 The Analysis of Interface Defects

5.4.3.1 Pt/ZnO contact

Capacitance (*C-f*) and conductance (*G-f*) techniques have been commonly adopted to investigate the interface defects distribution located in the forbidden band[142]. At large forward bias current, the validity of the measured capacitance values are limited by the LCR meter[170]. At small forward bias currents, the measured capacitance shows dependences on both voltage and frequency. Figure 5.21a shows the normalized *C-V* characteristics at a fixed frequency between 20 kHz to 1MHz. Figure 5.21b shows the frequency-dependence of capacitance at a steady DC bias. The results indicate that the measured capacitance originates from both the space charge region (C_s) depending on applied voltage and interface states (C_{it}) depending on frequency applied. Furthermore, the effect of the series resistance lowers the measured capacitance at high frequency as introduced in section 4.3.4. The capacitance at low frequency is significantly larger than the C_s from space charge region since the electron emission-capture process on the interface states in equilibrium with ZnO is able to follow the AC signal and induce excess capacitance. For an ideal Schottky diode, the conductance (G_p) should be independent to the small AC signal frequency ($\omega=2\pi f$). However, the G_p/ω - ω plots in Figure 5.21c show flattened curves for the

diode biased under small forward and reverse DC voltages. These G_p/ω - ω plots indicate frequency-dependence of G_p, attributed to the presence of the diode conductance, the effect of the series resistance (R_S), and impurity levels[69,138,139] as introduced in section 4.3.4. For diode biased under large forward DC voltages, the G_p/ω decrease continuously with increasing ω. This observation coincides with the case if G is almost a constant when the conductance contributed from the interface states response is screened out by the large diode conductance.

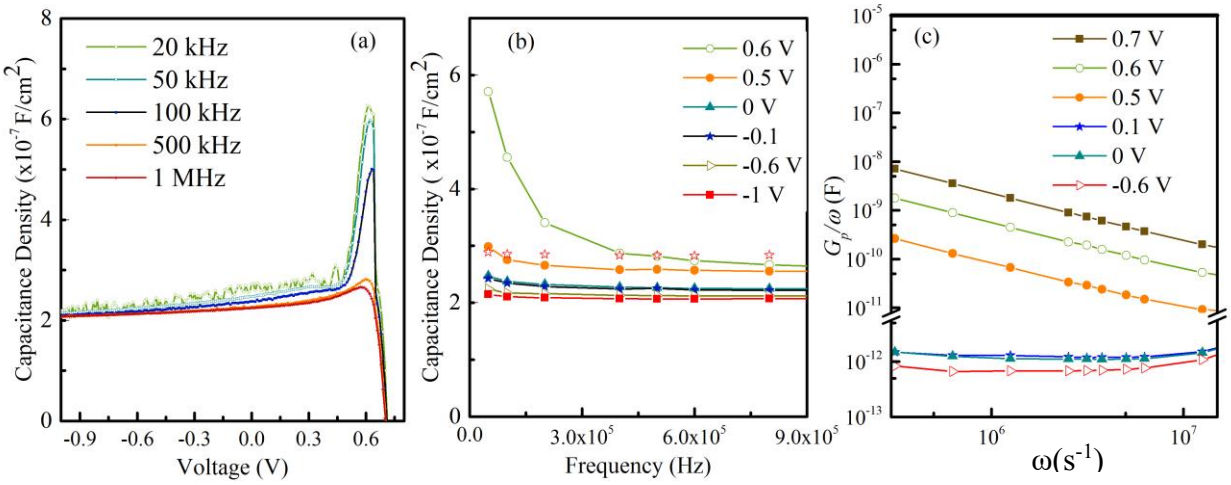

Figure 5.21. (a) Typical capacitance voltage plot of Schottky contact with different bias; (b) measured frequency-dependent capacitance for the diode under different DC bias condition; (c) G_p/ω - ω plots from conductance measurement for the Schottky diode under different DC bias condition.

By analyzing the *C-f* measurements, the interface states density and trap time constant can be extracted. For $G_p \ll 1/R_s$ and at low AC signal frequencies, the effect of R_s to the measured capacitance can be ignored[141], resulted in the measured capacitance being close to the parallel capacitance. The interface trap density and time constant can be obtained by fitting *C-f* curve with eq 4.51 in a frequency range of 50 kHz to 1MHz. At large forward bias, the effect of series resistance R_S on the measured capacitance become significant invalidating the fitting of the *C-f* curve with the simple model in eq 4.51. A fitting example of the experimental data is shown

in the inset of Figure 5.22 for 0.1 V bias. By performing the fitting to all bias voltages from -1 V to forward 0.3 V, an energy distribution of the interface states can be obtained as the energy level of the interface states E_{ss} with respect to the conduction band in *n*-type semiconductor is given by[138,142]

$$E_c - E_{ss} = q\Phi_B - q(V - IR_s) \qquad (5.8)$$

where E_c is the bottom of conduction band, $q\Phi_B$ is the barrier height and V is the applied voltage, IR_s is the voltage drop across the series resistance.

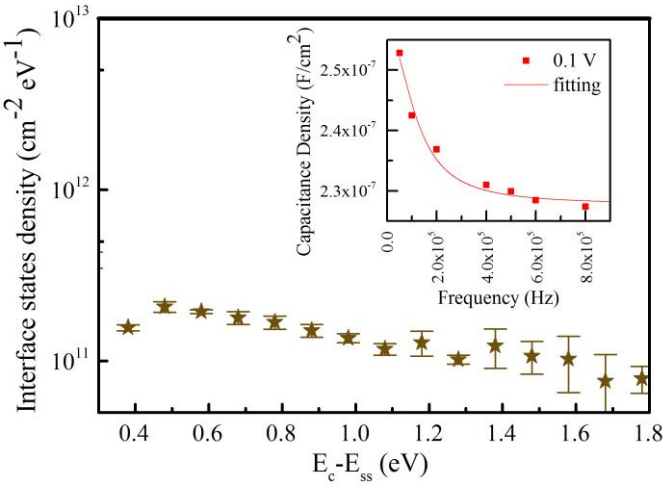

Figure 5.22. Energy distribution curve of the interface states fitted from C_p-*f* data for P-50-Pt. (Inset:The C_p-*f* characteristics of the Schottky diode at 0.1 V forward bias. The solid line presents the functional fitting)

As shown in Figure 5.22, the energy distribution of the interface states in the bandgap can has an overall gradual decrease of interface states densities away from the conduction band. There is a peak appearing close to the oxygen vacancies V_O(+2, 0) defect level at ~0.7 eV below the conduction band minimum(CBM)[50]. The increase of V_O close to the interface can be attributed to the chemical reaction at metal-ZnO interface. As mentioned above, V_O plays an important role in Schottky barrier formation by pining ZnO fermi level close to ~0.7 eV regardless of the metal work function[50], which corresponds to the peak position of the defects

energy distribution curve. This analysis agrees with the previous assertion of oxygen vacancies dominating interface states which also explains the potential fluctuations in the Schottky contact interface.

5.4.3.2 Cu/ZnO contact

The interface defects analysis is performed for Cu/ZnO contact by *C-f* and *G-f* techniques. A voltage- and frequency- dependent capacitance is also observed in this diode as shown in Figure 5.23. By functional fitting the *C-f* characteristics with eq 4.51 as shown in Figure 5.24a for 0 V bias for example, the interface trap density and the trap time constant can then be extracted to be 1.4×10^{12} $cm^{-2}eV^{-1}$ and 1.6 μs, respectively. A series of G_p/w versus frequencies plots calculated from measured *G-f* characteristics with various bias voltages are illustrated in in Figure 5.23c. The interface states density and the trap time constant can be obtained from the maximum value of the peak in G_p/w-w plot according to eq 4.53. The interface trap density and the trap time constant can then be extracted to be 3.7×10^{11} $cm^{-2}eV^{-1}$ and 0.8 μs respectively at 0 V bias. However, the conductance attributed to the interface states is screened out with the presence of large diode conductivity and significant series resistance, the analytical region in the *G-f* techniques is thus less than that in the *C-f* techniques.

The energy level of the interface traps E_{ss} with respect to the CBM is given by eq 5.8. An energy distribution profile of interface states is obtained and shown in Figure 5.24b. The interface traps density is larger than that of the Pt/ZnO diode and shows an overall decrease against increasing of E_c-E_{ss} but no obvious peak appears exactly around the oxygen vacancy transition energy level at 0.7±0.2 eV.

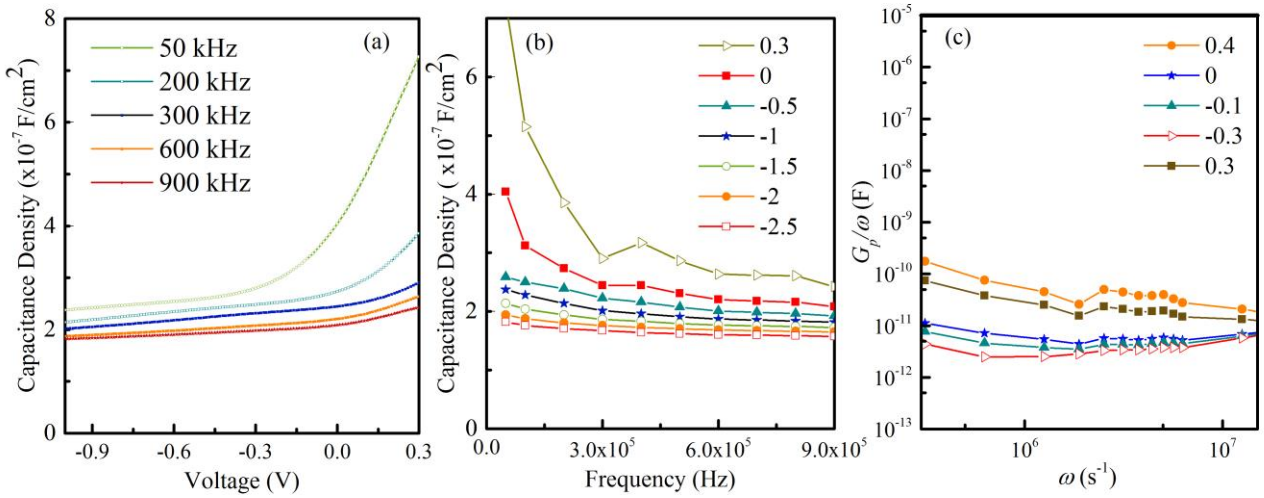

Figure 5.23. (a) Typical capacitance - voltage plot of Cu/ZnO Schottky contact with different bias; (b) frequency-dependent capacitance measured with different DC bias condition; (c) conductance measurement of Cu/ZnO Schottky diode with various DC bias condition.

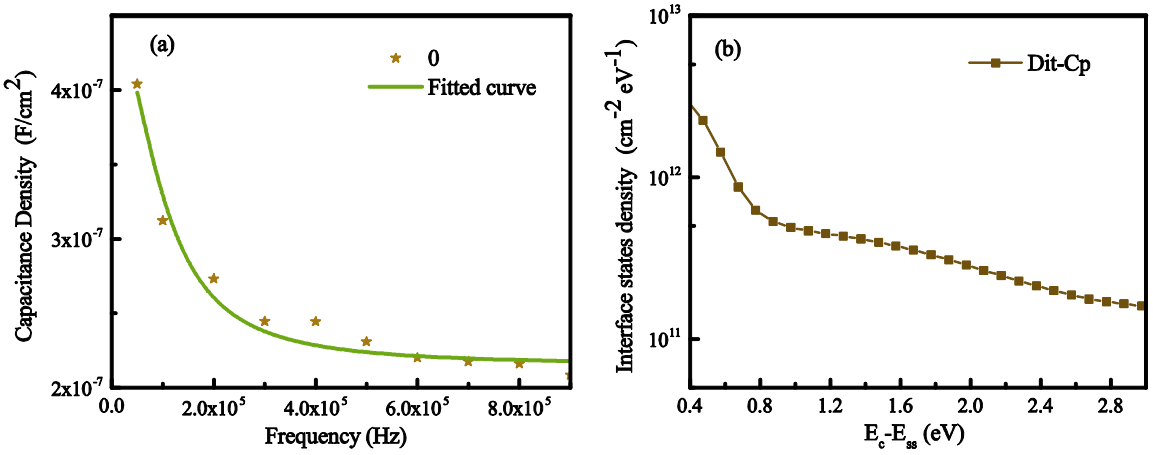

Figure 5.24. (a) The C_p-*f* characteristics of the Schottky diode at 0 V forward bias, the solid line presents the functional fitting plot; (b) energy distribution curve of the interface states fitted from C_p-*f* data at different bias for P-50-Cu.

5.4.4 Non-ideal Behavior Effect on Schottky Parameters

The deviation of ideality factor from unity can be attributed to the presence of different mechanisms including image force, barrier inhomogeneity, interface layers, series resistance, tunneling and trap assisted tunneling as introduced in section 4.4. Among those many

mechanisms, the effect of image force on Schottky parameters is essential for all Schottky contacts, and the thermionic field emission is speculated to dominate the current transport across the Schottky barrier in addition to thermionic emission. The evaluations of the effects of these mechanisms on Schottky contact performance are related to the doping concentration according to the conventional theories introduced in section 4.4. The doping concentration in the P-50-Pt diode is estimated by the $1/C^2 - V$ characteristics measured at 10 kHz as shown in Figure 5.25a and the extracted depth profile is depicted in Figure 5.25b according to section 4.3.3. The doing concentration in P-50 ZnO thin film is estimated to be 2.38 x 10^{17} cm^{-3}.

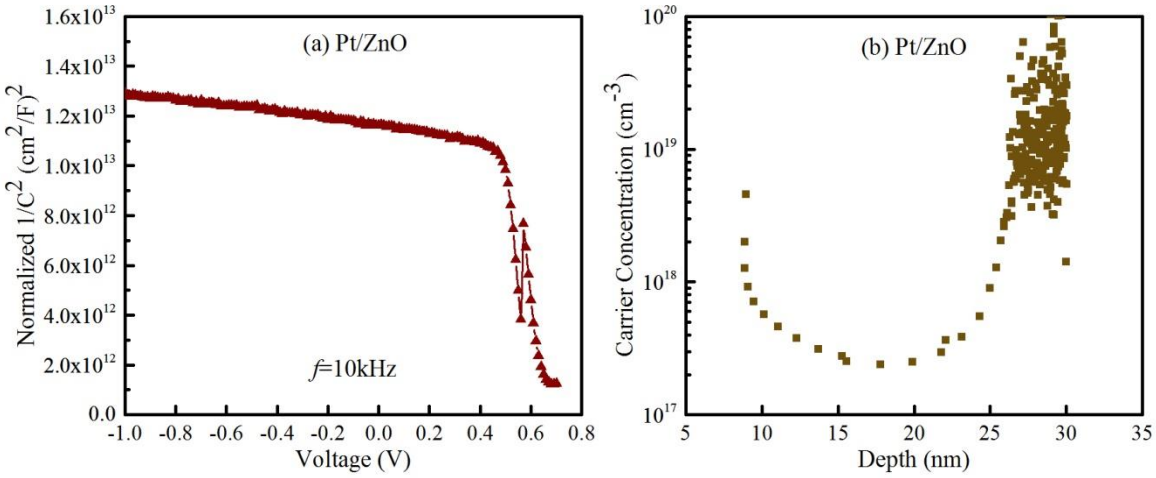

Figure 5.25. (a) Normalized $1/C^2$ versus voltage plot of Pt/ZnO contact; (b) Carrier concentration versus depth plot. The measurement was performed at 10 kHz frequency.

The image force lowering behavior is introduced in section 4.4.1. The barrier height lowering due to image force is depicted as a function of applied voltage assuming a Schottky barrier height of 1 eV according to eq 4.61 and shown in Figure 5.26 together with the ideality factor *n* calculated according to eq 4.62. The *n* is only increased by 2-7% at room temperature (300 K) which is not sufficient to explain the much larger values obtained from the room temperature measurements.

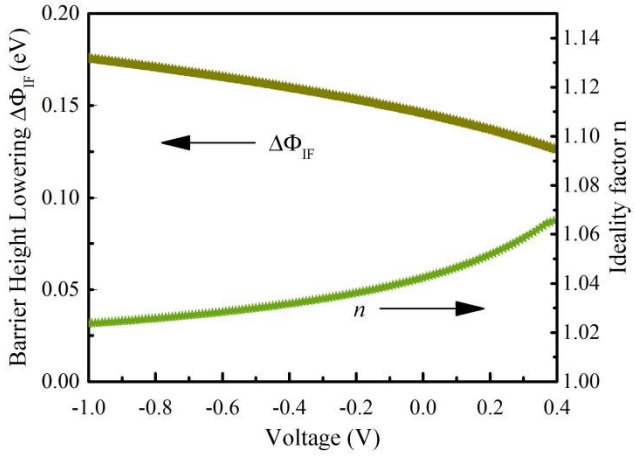

Figure 5.26. The barrier height lowering $\Delta\Phi_{IF}$ and ideality factor *n* enlargement introduced by image force.

According to Padovani and Stratton's thermionic field emission (TFE) model as introduced in section 4.4.2, the tunneling parameter E_{00} is 5 meV for such doped ZnO. The barrier height lowering due to the presence of TFE is depicted as a function of applied voltage assuming a Schottky barrier height of 1 eV and shown in Figure 5.27 together with the ideality factor *n* is calculated according to eq 4.64 and eq 4.65. The *n* is only increased by 1- 2% calculated at room temperature (300 K). Again, this value is too low to explain the much larger values extracted from the room temperature measurements. The conventional theory fails to explain the diode performance due to the finite thickness of the active layer in our case since the quantum mechanical transmission could be enhanced significantly in such nanoscale barrier. A model to calculate the apparent transmission coefficient and the combined current transport across this nanodiode is developed in section 5.5 following.

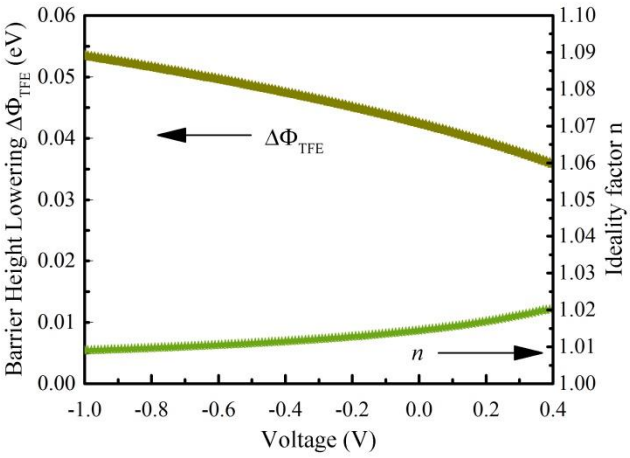

Figure 5.27. The barrier height lowering $\Delta\Phi_{TFE}$ and ideality factor n enlargement introduced by TFE.

5.4.5 Temperature-dependent Behavior of Schottky Parameters

5.4.5.1 Pt Contacts

A series of current density-voltage (j-V) plots for the P-50-Pt diodes at various ambient temperatures T are shown in Figure 5.28a. A Richardson plot of $\ln(j_s/T^2)$ versus $1/T$ for the saturation currents (j_s) deduced from the j-V curves by extrapolating the forward bias curve toward $V = 0$ is presented in Figure 5.28b. The Richardson plot is typically used to determine the thermal activation energy from the slope and the apparent Richardson constant (A^{**}) for specific diode according to section 4.3.2. Figure 5.28b shows the Richardson plot deviates from a straight line, indicating a temperature-dependent Φ_B due to other mechanisms besides thermal emission participating in the current transport[144,153,154,189]. The A^{**} and temperature-independent Φ_B for this particular diode is extracted as 1.932 A/cm^2/K^2 and 0.846 eV respectively by a linear fitting of the Richardson plot with eq 4.28 in the temperature range of 333 K – 413 K.

The limited temperature range leads to a large inaccuracy in the evaluation of A^{**}. The theoretical A^{*} value of 32 A/cm^2/K^2 for ZnO (m^{*}=0.27m_o) is still used for the extraction of Schottky parameters. Schottky parameters values are listed in Table 5.5 including Φ_B and n extracted from 0.1 - 0.2 V region of *I-V* plots according to eq 4.9 and 4.10. Figure 5.28c depicts the calculated Φ_B and n for diodes at different ambient temperatures T. The room temperature Φ_B are lower than that estimated by Schottky-Mott model (see Table 5.1), but similar to that reported previously for Pt on cleaned n-type single crystal ZnO wafer[58,64].

Table 5.5 Schottky parameters for Pt/ZnO diodes measured at temperature range from 293 K to 413 K.

T (K)	Φ_B (eV)	n
293	0.797±0.019	1.35±0.073
333	0.885±0.032	1.29±0.03
353	0.920±0.018	1.30±0.018
383	0.928±0.006	1.19±0.034
413	0.944±0.005	1.06±0.02

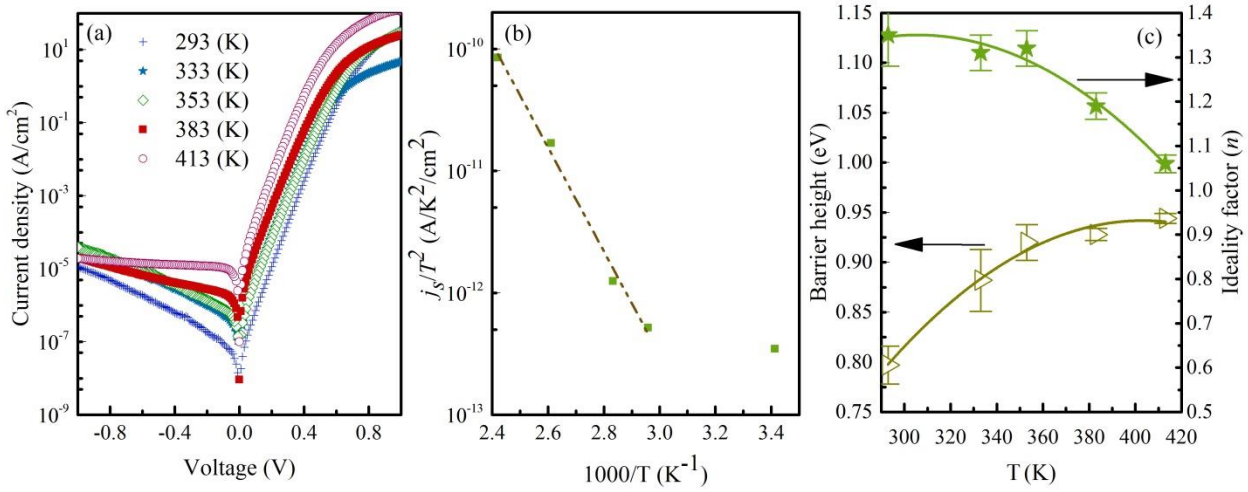

Figure 5.28. (a) Typical *I-V* characteristics of Pt/ZnO Schottky diode measured from 293 K to 413 K; (b) Richardson plot in the temperature range of 293 K – 413 K.; The inset is a schematic image of the Pt/ZnO diode; The contact diameter is 100 μm; (c) temperature-dependent barrier height ($q\Phi_B$) and ideality factor (n) for Pt/ZnO diodes measured at temperature range from 293 K to 413 K.

To deduce the barrier height and Richardson constant using a Richardson plot, precautions should be taken if temperature dependences of the Schottky parameters are observed from the *I-V-T* measurements. The variation of barrier heights and ideality factors extracted from *I-V-T* measurements by classical thermionic emission model can be attributed to the existence of excess current introduced by superposition of recombination current or/and field emission current over thermionic emission, or the presence of potential fluctuations at the interface of metal and semiconductor. The potential fluctuations in Schottky contact interface can be attributed to numbers of localized defects.

Furthermore, it is worthwhile to note that the breakdown voltage of the stabilized P-50-Pt diode was measured to be 5 V at room temperature indicating a breakdown electrical field of 1.67 MV/cm assuming a deep depletion mode planar capacitor configuration which is among the highest reported values for ZnO. In addition, the Pt contacts show thermal stability with temperature of at least 413 K, which is the highest temperature available in the cyclic temperature-dependent measurements.

5.4.5.2 Cu Contacts

A series of current density- voltage (*j-V*) plots at various measurement temperatures are shown in Figure 5.29a. A Richardson plot of $\ln(j_s/T^2)$ versus $1/T$ is presented in Figure 5.29b with the saturation currents (j_s) deduced by extrapolating the forward bias *j-V* curves towards *V*=0. By a linear fitting of the Richardson plot with eq 4.28 in the temperature range of 293 K – 383 K as shown in Figure 5.29b, the A^{**} and temperature-independent Φ_B for P-50-Cu diode are extracted as 6.9×10^{-4} A/cm^2/K^2 and 0.32 eV respectively. The extracted A^{**} is very much smaller than the theoretical value for ZnO (32 A/cm^2/K^2). At high measurement temperature, the diode

starts to degrade, leading to the deviation of Richardson plot from a straight line as observed in Figure 5.29b.

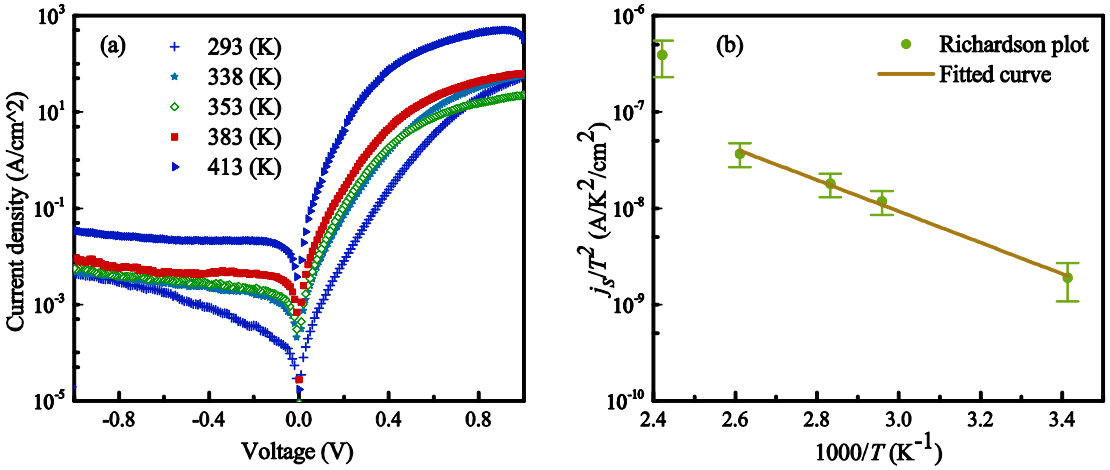

Figure 5.29. (a) Typical *I-V* curves of P-50-Cu Schottky diodes measured from 293 K to 413 K; (b) typical Richardson plot of the saturation current j_s obtained from the *I-V* curves in part (a).

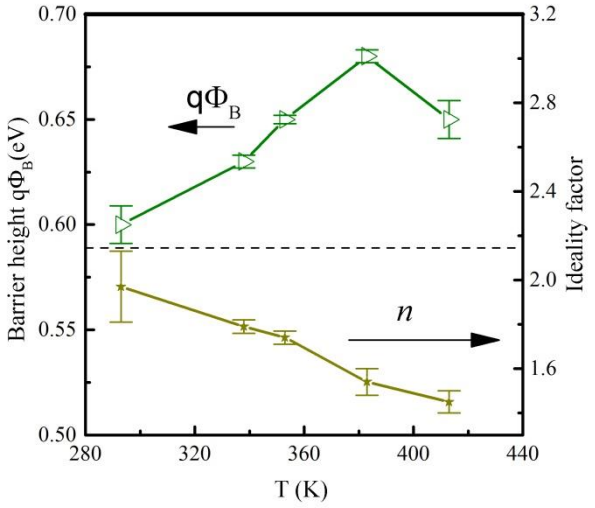

Figure 5.30. Temperature-dependent effective barrier height $q\Phi_B$ and ideality factor n for Cu/ZnO diodes measured at temperature T range from 293 K to 413 K.

The diode performance degrades permanently after measured at 140 °C. The rectifying behavior at room temperature becomes similar to the ones fabricated at deposition temperature of 200 °C discussed above. The early degradation indicates the P-50-Cu diode has less thermal

stability compared to the P-50-Pt diode. Note that the limited *T* range may leads to an inaccuracy of the extracted parameters. Furthermore, plots of barrier height qΦ_B and ideality factor (*n*) versus *T* are illustrated in Figure 5.30. The decrease of *n* with increasing *T* is observed. The increase of the Φ_B with increasing *T* is observed till ~383 K beyond which it decreases.

5.4.5.3 Barrier Inhomogeneity effect on *I-V-T* behavior

When the barrier inhomogeneity effect (introduced in section 4.4.4) is present in the contacts, the analysis of the experimental *I-V-T* characteristics with eq 4.9 and 4.10 now gives Φ_B^{inh} and n_{inh}, respectively, which should obey the relationship given by eq 4.71 and eq 4.72 provided the barrier inhomogeneity is the only mechanism besides thermionic emission responsible for the temperature-dependent properties of Schottky contacts. The plots of Φ_B^{inh}(T) versus *q/2kT* and (n_{inh}^{-1}-1) versus *q/2kT* are calculated and shown in Figure 5.31a along with their linear fits. The experimental results fit very well with the theoretical predication and gives $\overline{\Phi}_{B0}$=1.32 V and δ_0=0.16 V, and (n_{inh}^{-1} (T)-1) versus *q/2kT* plot gives ρ_2=-0.30 and ρ_3=0.029. This $\overline{\Phi}_{B0}$ value after correction is much closer to the theoretical Schottky barrier height value for P-50-Pt of 1.45 eV estimated by the ideal Schottky-Mott model. The standard deviation stands for the extent of the barrier inhomogeneity. The smaller the value of δ_0 means better homogeneity of the potential distribution. A δ_0 value of 0.16 V is significant when compared to the $\overline{\Phi}_{B0}$ value of 1.32 V for this P-50-Pt diode, indicating significant inhomogeneity of potential distribution. The linearity of the Richardson plot should be able to restore by taking into account the barrier inhomogeneity. The modified Richardson plot ln (j_s/T^2)-q^2 $\delta_0^2/2(kT)^2$ versus q/*k*T is shown in Figure 5.31b. The corrected A^{**}=11.64 A/cm^2/K^2 with an uncertainty of 141% due to the limited range of measurement temperature and $\overline{\Phi}_{B0}$=1.25±0.1 V are obtained for the P-50-Pt

diode by comparing the linear approximation of the modified Richardson plot with eq 4.73. The corrected A^{**} is much closer to the theoretical value of 32 A/cm^2/K^2 in comparison to that of 1.932 A/cm^2/K^2 obtained from the standard Richardson plot. This value is consistent with those values extracted from *I-V-T* measured in similar temperature ranges reported for the best ZnO Schottky diodes[183]. The $\overline{\Phi}_{B0}$=1.25±0.1 V from this modified Richardson plot agrees well with the value of 1.32 V obtained from the Φ_B^{inh}(T) versus *q/2kT* plot.

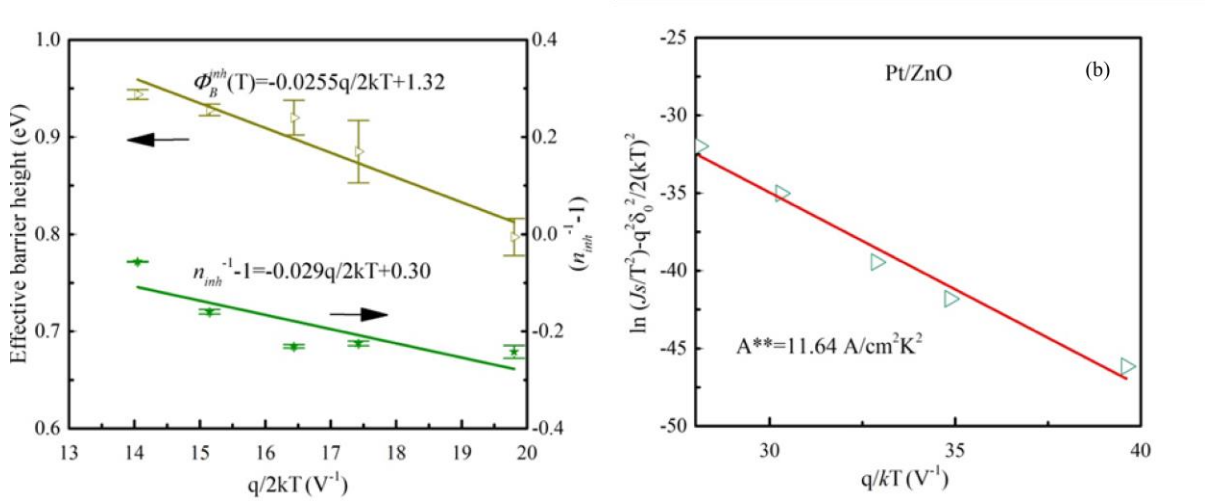

Figure 5.31. (a) The Φ_B^{inh}(T) versus q/2kT and (n_{inh}^{-1}-1) versus q/2kT plots with linear approximation for Pt/ZnO diode; (b) modified Richardson plot of ln (js/T^2)-q^2 δ_0^2/2(kT)^2 versus q/kT for Pt/ZnO diode.

For P-50-Cu, Φ_B^{inh}(T) versus *q/2kT* and (n_{inh}^{-1}(T)-1) versus *q/2kT* plots can be obtained using the experimental data of Φ_B^{inh}(T) and *n,* which are illustrated in Figure 5.32a. By comparing the linear approximation of the Φ_B^{inh}(T) versus *q/2kT* plot with eq 4.71, the zero bias mean barrier height $q\overline{\Phi}_{B0}$ and standard deviation δ_0 for P-50-Cu diode were obtained as 0.93 eV and 0.13 V, respectively. This estimated value of $q\overline{\Phi}_{B0}$is much higher than the value of 0.45 eV calculated from the ideal Schottky-Mott model for elemental Cu Schottky contacts, however, it is close to the one calculated for ideal CuO/ZnO heterojunction (~1 eV). This suggests that

significant oxidation on the Cu surface may occur pre-deposition or during deposition of the PEALD ZnO resulted an increase in the work function of the Cu surface.

The modified Richardson plot, $\ln(j_s/T^2)-q^2\delta_0^2/2(kT)^2$ versus q/kT, considering barrier inhomogeneity is shown in Figure 5.32b. The excellent linear fitting of the data indicates that the barrier inhomogeneity model can well explain the temperature-dependent phenomena of the Cu/ZnO contact before it reach the high temperature limit. The intercept value (with an uncertainty of 34.5% due to the limited available measurement temperature) of the plot is used to get the A^{**}=19.96 A/cm^2/K^2 for the Cu/ZnO diode, which is much closer to the theoretical Richardson constant for ZnO of 32 A/cm^2/K^2 comparing with that of 6.9x10^{-4} A/cm^2/K^2 obtained before the inhomogeneity correction was considered.

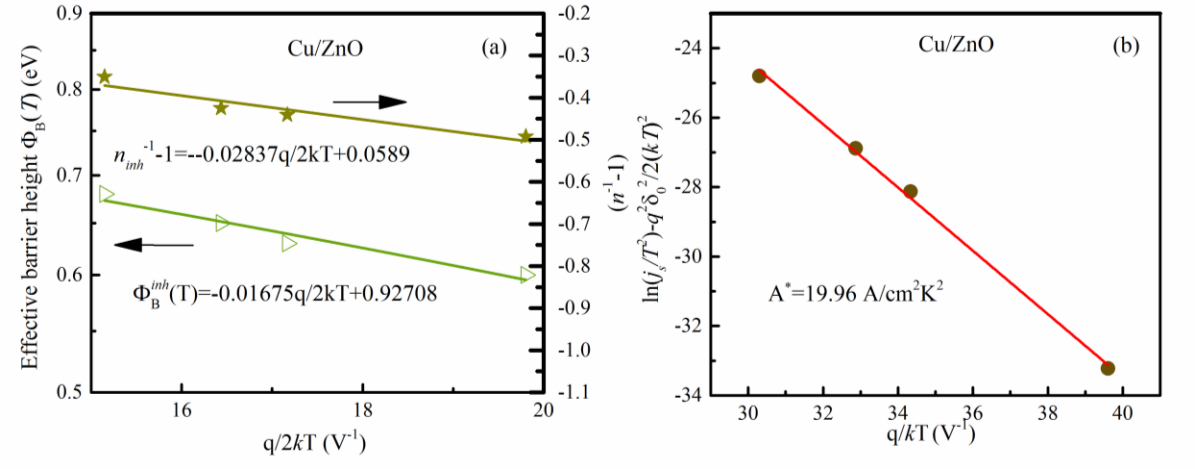

Figure 5.32 The Φ_B(T) versus q/2kT and (n^{-1} (T)-1) versus q/2kT plots with linear approximation for Cu/ZnO diode; (b) modified Richardson plot of ln (js/T^2)-q^2 $\delta 0^2$/2(kT)^2 versus q/kT for Cu/ZnO diode.

5.5 CURRENT TRANSPORT MODEL FOR NANODIODE

There are various current transport mechanisms existing in rectifying metal-semiconductor contacts affecting the majority carrier current flow including diffusion, thermionic emission, tunneling, space-charge-limited effect, image force lowering of the barrier

height, etc.[130]. In nanodiodes with such a thin layer of semiconductors, further expansion of the space charge region with increasing reverse bias voltage is prevented by the finite physical dimension. Thus, the electrical field distribution in the semiconductor will principally deviate from the conventional models discussed in the section 4.3, and subsequently affects the tunneling probability across the barrier and the thermionic field emission (TFE) current transport in the diode[190,191]. Ideally, the space charge region can principally "reach through" the whole semiconductor layer if the ZnO's doping concentration is lower than 10^{18} cm^{-3} without any extra bias[192]. However, in practice with metal electrodes in both sides, the semiconductor surface layers close to the ohmic side is tends to be degenerately doped due to unintentional factors such as hydrocarbons contaminations from atmosphere, and the defects introduced by the sputtering, inter-diffusion of metal (referring to Al used in this work) into semiconductor, etc.

5.5.1 Schottky Potential Barrier for Calculating Transmission Probability

The following assumptions are proposed based on the previous observations to model the current transport mechanisms: (I) the top few nanometers of ZnO layer in this region W_d to W is degenerately doped (n^+); (II) the bottom ZnO layer is uniformly doped with a carrier concentration of N_D in $x \leq W_d$. A schematic diagram of the proposed diode layout is depicted in Figure 5.33.

The electrical field $\xi(x)$ and barrier potential $U(x)$ profile in the Schottky diode are calculated by Poisson's equation as

$$\xi(x) = \begin{cases} \frac{qN_D}{\varepsilon_S\varepsilon_0}x + \frac{qn^+}{\varepsilon_S\varepsilon_0}W_d - \frac{qN_D}{\varepsilon_S\varepsilon_0}W_d - \frac{qn^+}{\varepsilon_S\varepsilon_0}W & 0 \leq x < W_d \\ \frac{qn^+}{\varepsilon_S\varepsilon_0}x - \frac{qn^+}{\varepsilon_S\varepsilon_0}W & W_d \leq x < W \end{cases} \quad (5.9)$$

$$U(x)=\begin{cases}-\frac{qN_D}{2\varepsilon_S\varepsilon_0}x^2-\left(\frac{qn^+}{\varepsilon_S\varepsilon_0}W_d-\frac{qn^+}{\varepsilon_S\varepsilon_0}W-\frac{qN_D}{\varepsilon_S\varepsilon_0}W_d\right)x & 0\le x<W_d\\ -\frac{qn^+}{2\varepsilon_S\varepsilon_0}x^2+\frac{qn^+}{\varepsilon_S\varepsilon_0}Wx+\frac{qN_D}{2\varepsilon_S\varepsilon_0}{W_d}^2-\frac{qn^+}{2\varepsilon_S\varepsilon_0}{W_d}^2 & W_d\le x<W\end{cases} \quad (5.10)$$

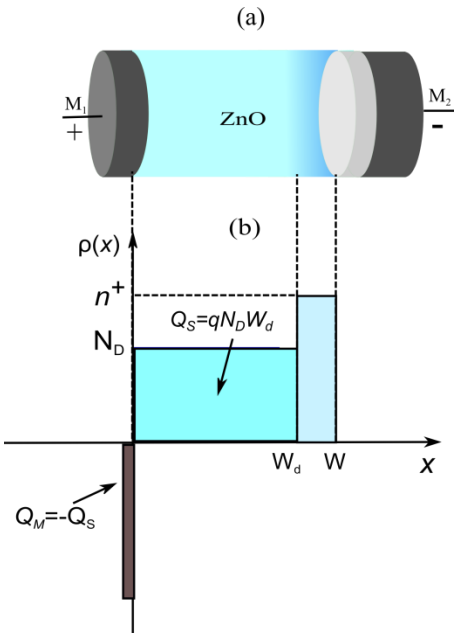

Figure 5.33. (a) Schematic diagram of a ZnO Schottky diode (not to scale); (b) assumed doping profile in the ZnO layer.

Where

$$W=\sqrt{\frac{2\varepsilon_S\varepsilon_0(V_{bi}-V_a)+qn^+{W_d}^2-qN_D{W_d}^2}{qn^+}} \quad (5.11)$$

and $qV_{bi}\approx q\Phi_1$, which is the barrier height in M_1 contact. By taking into account the image force effects, $U(x)$ becomes

$$U(x)=\begin{cases}-\frac{qN_D}{2\varepsilon_S\varepsilon_0}x^2-\left(\frac{qn^+}{\varepsilon_S\varepsilon_0}W_d-\frac{qn^+}{\varepsilon_S\varepsilon_0}W-\frac{qN_D}{\varepsilon_S\varepsilon_0}W_d\right)x-\frac{qx}{6\pi\varepsilon_\infty\varepsilon_0} & 0\le x<W_d\\ -\frac{qn^+}{2\varepsilon_S\varepsilon_0}x^2+\frac{qn^+}{\varepsilon_S\varepsilon_0}Wx+\frac{qN_D}{2\varepsilon_S\varepsilon_0}{W_d}^2-\frac{qn^+}{2\varepsilon_S\varepsilon_0}{W_d}^2-\frac{qx}{6\pi\varepsilon_\infty\varepsilon_0} & W_d\le x<W\end{cases} \quad (5.12)$$

Where ε_∞ is the image force permittivity (4 for ZnO). The electrical field profile and barrier potential profile is determined and depicted in Figure 5.34a and b, respectively. The constants used in the calculation are: the dielectric permittivity ϵ_s =9 ϵ_0 for ZnO, doping concentration N_D

= $2x10^{17}$ cm^{-3} in the low doped region with thickness W_d = 19 nm, doping concentration n^+ = $2x10^{19}$ cm^{-3} in degenerately doped region, and Schottky barrier height $q\Phi_1$=1 eV.

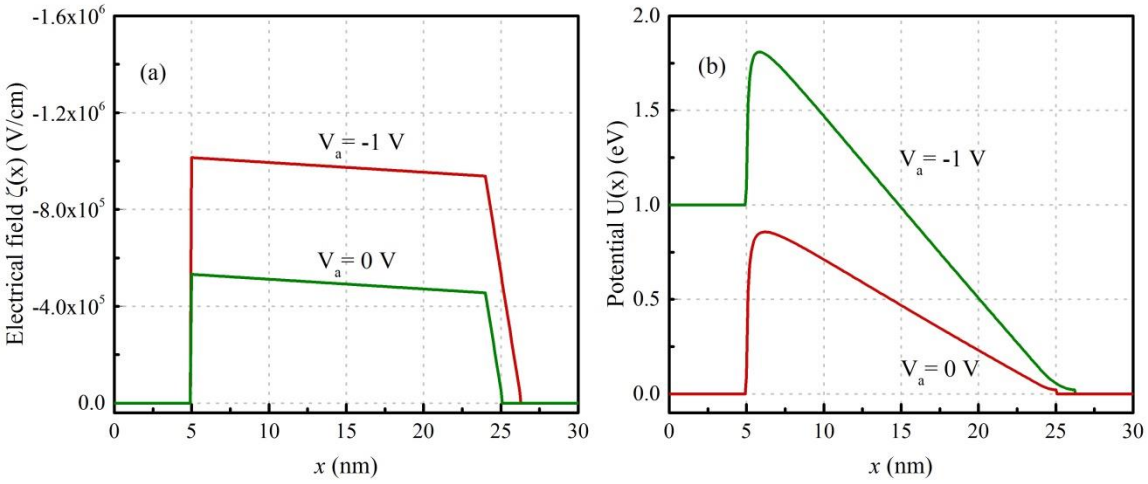

Figure 5.34. (a) The profile of electrical field distribution across the Schottky Nanodiode under an applied voltage V_a; (b) The profile of potential distribution across the Schottky nanodiode under an applied voltage V_a.

5.5.2 Calculation of Transmission Probability in Schottky Nanodiodes

At the interface of metal and semiconductor in Schottky contacts, the potential functions usually vary abruptly as can be seen in Figure 5.34b. In this case, the use of conventional Wentzel-Kramers-Brillouin (WKB) approximation to calculate the transmission probability across potential barriers leads to large inaccuracy[193]. Another method for calculating the transmission coefficient is to solve Schrodinger's equations step by step all the way across the potential barriers to get the final values of the wave function as described by Chandra and Eastman[194]. In addition, analytical calculations of the tunneling coefficient by connecting the Airy functions at two interfaces were applied by reseachers[195,196], which was showed by Lui and Fukuma[197] that this calculation was applicable to use with arbitrary piecewise linear potential barriers. However, these calculations have never been taken into account variations of electron

effective masses which are critical for resonant tunneling in quantum-well or supperlattice, and also, complicated treatment are usually encountered for these cases. In this work, accurate calculation of transmission coefficient across the Schottky barrier in the nanodiode applies a simpler method with multistep potential approximations for potential functions, effective mass functions and permittivity functions. The transmission coefficient across the Schottky diode potential barrier is calculated by connecting momentum eigenfunctions[197,198].

To begin with, the potential barrier is split up into N discrete segments where the potential energy can be regarded as a constant, e.g. an arbitrary potential function as shown in Figure 5.35. As the divisions become finer, the approximated potential function will get closer to the actual one. The potential barrier $U(x)$, the effective mass $m^*(x)$, and the permittivity $\epsilon(x)$ at the j^{th} segment are approximated as

$$U(x) = U_j = U\left[\left(x_{j-1} + x_j\right)/2\right] \qquad (5.13)$$

$$m^*(x) = m^*{}_j = m^*\left[\left(x_{j-1} + x_j\right)/2\right] \qquad (5.14)$$

$$\epsilon(x) = \epsilon_j = \epsilon\left[\left(x_{j-1} + x_j\right)/2\right] \qquad (5.15)$$

For $x_{j-1}<x<x_j$ ($j=0, 1, 2 \ldots N, N+1$).

The wave function ψ_j in the jth segment for an electron with energy E is given by

$$\psi_j(x) = A_j \exp\left(ik_j x\right) + B_j \exp\left(-ik_j x\right) \qquad (5.16)$$

where

$$k_j = \sqrt{\left[2m_j^*\left(E - U_j\right)\right]}/h/2\pi \qquad (5.17)$$

And h is the Planck's constant.

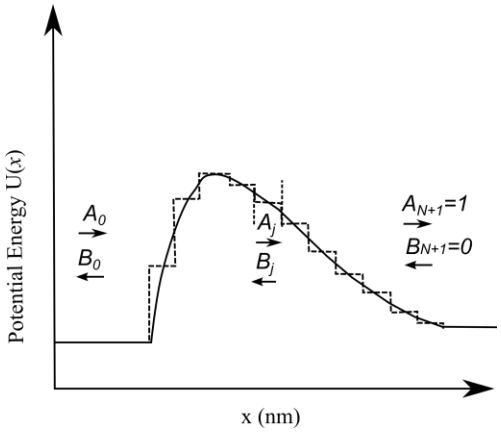

Figure 5.35. Energy band diagram (solid line) and it multistep approximation (broken line) across the potential barrier.

Since the continuity of $\psi_j(x)$ and $(1/m_j^*)$ $(d\psi_j/dx)$ at each boundary is conserved, the determination of A_j and B_j in eq 5.16 can be reduced to the multiplication of the following N+1 (2x2) matrices,

$$\begin{pmatrix} A_0 \\ B_0 \end{pmatrix} = \prod_{j-1}^{l=0} M_l \begin{pmatrix} A_j \\ B_j \end{pmatrix} \qquad (5.18)$$

Where

$$M_l = \frac{1}{2}\begin{bmatrix} (1+S_l)\exp[i(k_{l+1}-k_l)x_l] & (1-S_l)\exp[-i(k_{l+1}+k_l)x_l] \\ (1-S_l)\exp[i(k_{l+1}+k_l)x_l] & (1+S_l)\exp[-i(k_{l+1}-k_l)x_l] \end{bmatrix} \qquad (5.19)$$

And

$$S_l = \frac{m_l^*}{m_{l+1}^*}\frac{k_{l+1}}{k_l} \qquad (5.20)$$

By setting $A_{N+1} = 1$ and $B_{N+1} = 0$ in eq 5.18 for $j = N+1$, the transmission probability $D(E)$ can be calculated as[194]

$$D(E) = \frac{m_0^*}{m_{N+1}^*}\frac{k_{N+1}}{k_0}\frac{1}{|A_0|^2} \qquad (5.21)$$

Transmission probability from metal1 to metal2 is calculated for the barrier potential function calculated in last section, and depicted in Figure 5.36a for electrons with variable kinetic energy E_K and Figure 5.36(b) for electrons with fixed E_K under variable bias conditions,

respectively. The division for each discrete segment is set to be 0.1 nm in the calculation. The constants used in the calculation are: the effective mass $m^* = 0.27\ m_0$ for transport in ZnO, the dynamic dielectric permittivity $\epsilon_s = 9\epsilon_0$ for ZnO. The oscillatory behavior of the transmission coefficient in Figure 5.36b is supposed to be due to resonance through the virtual states above the barrier, which should be reduced with finer divisions[198].

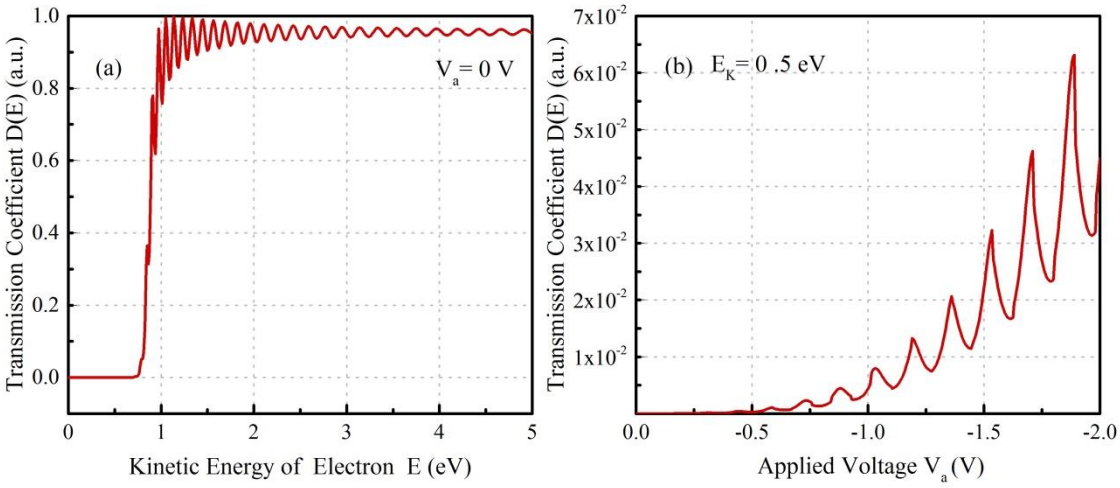

Figure 5.36. (a) Transmission probability for electrons with variable kinetic energy E_K under 0 V bias voltage; (b) Transmission probability for electrons with fixed E_K=0.5 eV under variable applied bias voltage.

5.5.3 Current Transport across Schottky Nanodiode

The carrier transport across the Schottky barrier will be considered in two parts: I. carrier traversing from semiconductor to metal corresponds to current density J_{SM}; II. Carrier traversing from metal to semiconductor corresponds to current density J_{MS}. The total current density is then obtained as the algebraic sum of these two components[199,200]:

$$J = J_{SM} - J_{MS} \qquad (5.22)$$

The expression for J_{SM} and J_{SM} is

$$J_{SM} = \frac{A^*T}{k}\int_{U_{max}}^{\infty} D(E)exp\left[\frac{-E}{kT/q}\right]dE + \frac{A^*T}{k}\int_{E_{fs}}^{U_{max}} D(E)F_S[1 - F_m(V)]dE \qquad (5.23)$$

$$J_{MS} = \frac{A^*T}{k}\int_{U_{max}}^{\infty} D(E)exp\left[\frac{-E}{kT/q}\right]dE + \frac{A^*T}{k}\int_{E_{fs}}^{U_{max}} D(E)F_m(V)[1 - F_s]dE \qquad (5.24)$$

Where U_{max} is the maximum potential in the diode barrier profile, E_{fs} is the fermi level in semiconductor. The first terms in both eq 5.23 and eq 5.24 are the thermionic component and the second terms correspond to the tunneling component. F_m and F_S are the Fermi-Dirac distribution functions in metal and semiconductor, respectively, as

$$F_S = \frac{1}{1+exp\left(\frac{E-E_{fs}}{kT/q}\right)} \qquad (5.25)$$

$$F_m(V) = \frac{1}{1+exp\left(\frac{E-V-E_{fm}}{kT/q}\right)} \qquad (5.26)$$

The calculated results of *I-V* characteristics are shown in Figure 5.37 compared to the experimental results for a P-50-Pt diode. The Richardson constant A^* = 32 A/cm^2/K^2 is used in the calculation. The calculated *I-V-T* characteristics showed good agreement with the experimental data in the reverse bias region whereas the deviation in the forward bias region at low temperature could be attributed to the series resistance, interface states charge, etc. which critically impact the ideality factor in the forward bias *I-V* characteristics. The model developed here does not take into account the effect of those imperfect factors on the forward *I-V* characteristics yet.

The agreement in the reverse bias *I-V* characteristics verifies the superposition of thermionic field emission (TFE) over thermionic emission (TE) dominating the carrier transport at low temperature. As the temperature increased, the dominating current transport mechanism transited to almost pure TE mechanism with a constant leakage current. The calculation showed

the doping concentration of degenerately doped region in ZnO thin film tended to decrease during heating, which suggested that the dopant in the degenerately doped region of the thin film can be reduced by annealing. The dopants could come from absorptions during fabrication or left over derivatives from deposition. In addition, the reduction of the doping concentration led to the lowering of transmission coefficient and reduction of the voltage dependence on the leakage current, leading to the more ideal performance of the diode.

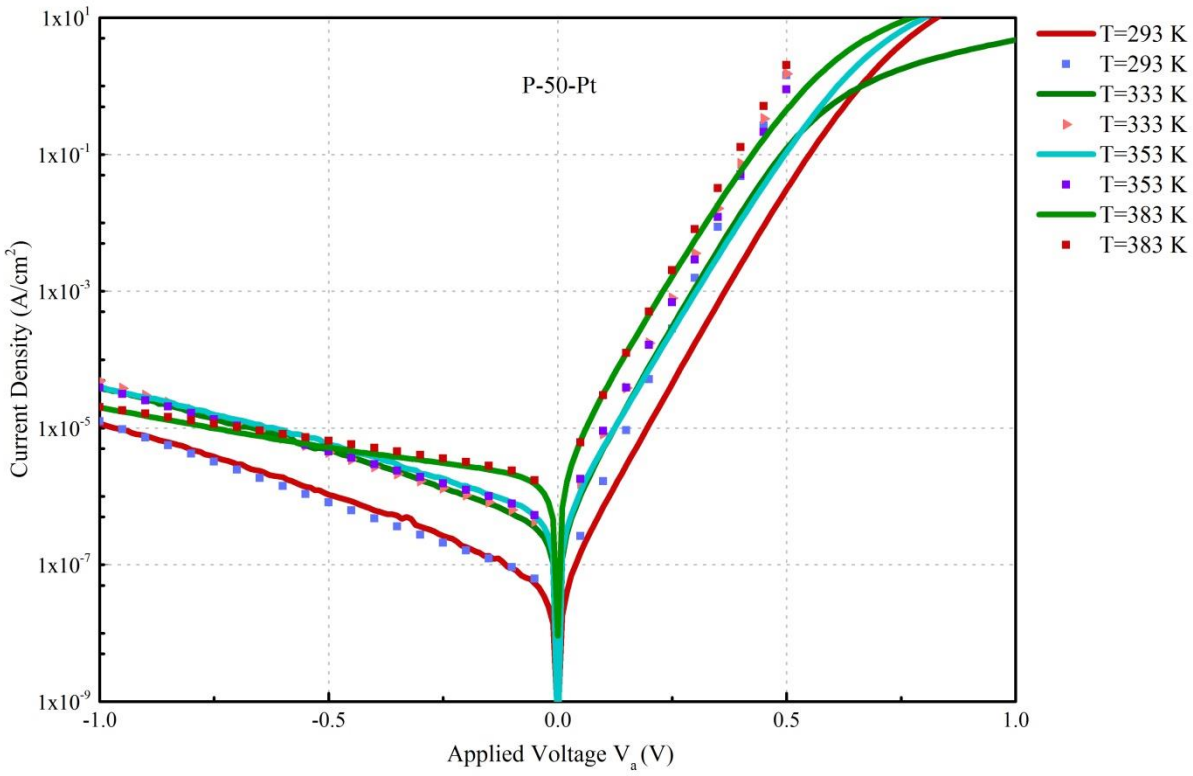

Figure 5.37. Comparison of calculated (dotted line) and empirical (solid line) *I-V-T* characteristics for a P-50-Pt diode at various measurement temperatures.

In addition to ALD fabricated nanodiodes, nanodiodes based on ZnO thin films grown by pulsed laser deposition (PLD) at a deposition temperature of 250 °C have been fabricated and characterized. The details can be found in Appendix I. Finally, the TiW Schottky contact was

applied in source gated thin film transistors (SGTFTs) based on ALD ZnO thin films. The details of the SGTFT device can be found in Appendix II.

Chapter 6

Conclusions

In this thesis project, studies are carried out for vertical Schottky nanodiodes (SNDs) consist of 30 nm thick nanocrystalline ZnO thin films with bottom Schottky electrodes, which are grown by atomic layer deposition (ALD) at 50 °C to 200 °C deposition temperatures. The relative low processing temperature and simple fabrication steps made the SNDs ideal for flexible electronics applications and hybrid integration on sensor chips. A systematic study of Schottky metallization materials on ZnO thin film was performed to explore proper contact material. The studies showed that the *I-V* characteristics of the SNDs depended on not only the Schottky barrier height but also the doping concentration of the ZnO thin films grown by ALD, because of the presence of thermionic filed emission in the carrier transport across the barrier. The doping concentration in ZnO active layer showed negative dependence on the deposition temperature of PEALD.

6.1 CONCLUSIONS FOR STUDY I

In study I, we investigated the performance of a series of metal contacts to ZnO thin films grown by P-200 (PEALD at 200 °C deposition temperature) and T-200 (TALD at 200 °C deposition temperature). All of the devices with T-200 ZnO thin film showed ohmic behavior which can be attributed to the Zn-rich interface and Zn-rich thin films. The devices with P-200 exhibited rectifying behavior with Ag, TiW, Cu, and Ni contacts but linear behavior with Au and Pt contact. The P-200 ZnO thin films had stoichiometric compositions of Zn and O. The Zn-rich non-stoichiometric composition of T-200 thin films pointed to higher doping concentration than

that of P-200 films. In addition, the high doping concentrations of ZnO layers for both P-200 and T-200 films were attributed to the hydrogen impurity in the ZnO thin films. Both the P-200-Cu and P-200-TiW samples showed an O-rich interface while the T-200-Cu showed Zn-rich interface, indicating the oxidation of the metallic layer of the substrate was more significant in PEALD than TALD. The oxidation of the metal substrates in atmosphere or during the initial deposition cycles of PEALD determined the formation of O-rich interface, which improved the stoichiometric composition, reduced the interface doping concentration, reduced the tunneling probability and consequently led to rectifying behavior across the Schottky barrier. In summary for study I, we found:

- The ease of initial oxidation of the metal substrate surface contributes significantly to the formation of O-rich interface, and subsequently the formation of rectifying contact. The oxidation of Pt and Au can rarely occur since the reaction is endothermic, while the oxidation of other candidates are driven by their exothermic free energy of formation with Ag>Cu>Ni>W>Zn>Ti. This leads to the failure of Pt and Au contacts to P-200 ZnO thin film.
- The thermal reliability of the metal substrates with ZnO is another important factor in identify good Schottky contact. The poor rectifying behavior of all the devices with P-200 ZnO could be due to their thermal reliability cannot stand the high ambient temperature of 200 °C during deposition of ZnO.
- The P-200-Cu and P-200-TiW diodes give the best rectifying behavior among this set of devices with relatively high Φ_B of 0.53 eV and 0.54 eV, respectively.
- The presence of significant effect of series resistance leads to larger inaccuracy in the extracted Schottky parameters from the *I-V* plot. The alternative $J/\{1-\exp[-qV/kT]\}-V$

approach is less sensitive to the effect of series resistance on extrapolating Schottky parameters and provides more accurate Schottky parameters. The values of Φ_B obtained by two methods are very close with an deviation of 0.1 eV while the values of n obtained by the $J/\{1\text{-}\exp[-qV/kT]\}$-$V$ approach is significantly smaller than that by I-V plot.

- The C-V technique gives the doping concentration in ZnO thin films. For the contacts without significant effect of series capacitance such as P-200 TiW and Cu contacts, the extraction of doping concentration from C-V curves is more reliable, and extracted data show P-200-TiW has larger doping concentration than P-200-Cu.
- The hydrogen impurity is detected in both P-200 Cu and TiW contacts. The difference of hydrogen impurity level provides evidence in the view of chemistry for the different doping concentration in the ZnO thin film.

6.2 CONCLUSIONS FOR STUDY II

Study II studied the optimization methods for Cu contacts to ZnO thin films deposited by PEALD at deposition temperatures of 100 °C, 130 °C and 200 °C. PEALD grown ZnO active layer with lower deposition temperature showed improvement of Schottky rectifying behavior with slightly increased Schottky barrier height and decreased ideality factor. Increase of oxygen plasma pretreatment duration on Cu substrate didn't show any beneficial impact on the device. The annealing of P-130-Cu devices showed improved rectifying behavior. In summary for study II, we found:

- Lowering ZnO PEALD deposition temperature improves the rectifying behavior of Cu/ZnO contacts with slightly increased Schottky barrier height and reduced ideality factor extracted from I-V characteristics. In the view of thermodynamics,

the lower deposition temperature reduced interfacial oxide (CuO in this case) formation. The theory of interfacial layer effect can explain the ideality factor values much larger than unity and also agrees well with the thermodynamics expectation. The doping concentration of ZnO thin films obtained from *C-V* characteristics decreases with decreased deposition temperature.

- Longer oxygen plasma pretreatment increases the series resistance which is destructive for the turn on behavior of the diode. The capacitance-voltage characteristics also show significant effect of series resistance induced by too long oxygen plasma pretreatment. Thus, the oxygen plasma pretreatment duration should be kept short enough to avoid over-oxidation of the Cu substrates.
- Good thermal stability at least 300 °C is observed by tracking the *I-V* characteristics with increased annealing temperature. The C-*V* characteristics show the doping concentration in ZnO is reduced by annealing at 300 °C. Diodes break down permanently after annealing at 400 °C for 5 mins.
- With lower doping concentration in ZnO deposited at lower temperature or annealed, the device performance is improved. This observation points to the presence of thermionic field emission (TFE) in addition to thermionic emission in the current transport in the diodes under study, since the TFE is related to the doping concentration in ZnO.

6.3 CONCLUSIONS FOR STUDY III

In study III, we found that the P-50-Pt diode behaved best with high performance and excellent uniformity across the wafer. Pt contact showed significant improved rectifying

behavior over time; Cu, Cr and Ru contacts showed good stability with slightly change over time; TiW and Ni contacts showed obvious degradation in rectifying performance over time. The significant degradation of the TiW and Ni diodes could be due to interface chemical reaction or interdiffusion between ZnO and metal contacts over time after fabrication.

The thermal stability of Pt contact and Cu contact was studied. Both Pt and Cu contacts showed decreasing ideality factor and increasing barrier height with increasing ambient temperature, indicating that the effects of other current transport mechanisms besides TE decreased at high temperature and left TE as the dominant current transport mechanism.

The calculation of transmission coefficient across the Schottky barrier potential was performed to evaluate the dominant carrier transport mechanism. The calculated *I-V* characteristics showed good agreement with the experimental data. This verified the presence of thermionic field emission (TFE) dominating the carrier transport at low temperature. While the temperature increased, the field emission portion in the current transport vanished gradually to pure TE mechanism at high operating temperature. The calculation also showed the change of doping profile across the active layer was responsible for the variation of *I-V* characteristics of the diode.

Although all the Schottky diodes in this project were fabricated on rigid Si wafer for better understanding of the effects of various processes on the device performance. The low processing temperature used in this thesis project makes it compatible for flexible substrates like plastic and hybrid integration. Different to that in conventional Schottky contact theories, the doping concentration of the semiconductor and the applied voltage affect the diode performance

due to the presence of TFE in the SNDs. Thus, relatively low doping concentration is necessary to produce high performance SNDs. In summary for study III, we found:

- The suitability of various metal electrodes as Schottky contact to ZnO thin film is identified by the rectifying behavior of the devices. Extensive aging effect studies for all SNDs show spontaneous degradation of the rectifying behavior with TiW and Ni contacts, relatively stable rectifying behavior with Cu, Cr and Ru contacts, and spontaneous improvement of the rectifying behavior with Pt contact.

- To be a good bottom Schottky electrode, the metal has to be resistive to interface chemical reaction and diffusion during and after fabrication. Au is not a good candidate due to its poor thermal stability-react with ZnO at temperature less than 100 °C. Taking into account the degradation of the devices as they age, the ranking of good Schottky candidates is Pt>Cu>Cr>Ru>TiW>Ni>Au.

- Series resistance analysis for P-50-Pt show a dynamic R_S suggests that the ohmic contact Al/Au is not the best choice for ZnO SND. The Al is easy to be oxidized and causes an interfacial layer with high resistance.
- The interface defect distribution of P-50-Pt and P-50-Cu is identified. Pt contact shows less interface defects than the Cu contact. The low interface defect density ($\sim 10^{11}$ $cm^{-2}eV^{-2}$) for both SNDs is one of the reasons for their good rectifying behavior.
- The conventional mechanisms for non-ideal behavior include the image force (IF), thermionic field emission (TFE), and barrier inhomogeneity are applied to study the insight for the Schottky performance and temperature-dependent behavior.

Conventional IF and TFE fail to explain the large ideality factor values and is attributed to the finite physical dimension of the SNDs. The barrier inhomogeneity model explains the temperature-dependent behavior of the diodes with some extent of deviations.

- The current transport model developed for the SNDs gives simulated *I-V* characteristics consistent with the measured data in the reverse bias region. The deviation in the forward bias region is attributed to the significant effect of *Rs*.
- The best SND achieved in this work P-50-Pt demonstrates remarkable room temperature performance with rectifying ratio of ~10^6, effective barrier height values of 0.76±0.014 eV, ideality factor values of 1.140±0.007, series resistance down to 90 Ω at 1V and breakdown field of at least 1.67 MV/cm.

6.4 DIRECTIONS FOR FUTURE WORK

6.4.1 Issues to Solve

The carrier transport in our Schottky contacts depends on the doping concentration produced unintentionally during the deposition process of ZnO. Contaminations or defects induced in the processing may leads to the failure of the device, especially during the top contact sputtering. A better control of the diode property could be achieved with less invasive fabrication techniques for the top contact like ALD. Furthermore, the series resistance of our diodes is still too large at present time for ultrahigh frequency RF applications. Other contact materials including nitride, such as ZrN and TiN due to its chemical stability and reasonable electrical resistivity (15 $\mu\Omega$ cm), and borides, such as W_2B_5 and CrB_2, due to its hexagonal structure and reasonable resistivity value could be better candidates as Schottky contacts. In addition, the thermal stability of the diode affects the long term diode performance. Although Pt contact has shown best performance and excellent stability over a long period of time, but Pt is costly. Further studies to find suitable thermal stable and economical materials as Schottky contacts for ZnO are still needed for low cost applications. To further improve the rectifying ratio, thin dielectric film insertion can be applied. Krajewski *et al* have recently demonstrated the tuning of the properties, mainly the rectifying ratio, of ALD-ZnO-based rectifying structures by inserting a thin dielectric film[101,102].

6.4.2 The Potential Applications of ZnO Schottky Diodes

6.4.2.1 Rectifier

Schottky diode (SD) is commonly used in the design of rectify circuits since SDs have advantages of fast switching speed and low turn on voltage, which is particularly important for application in power detection and microwave network circuits. ZnO based Schottky diodes currently are attracting increasing attention for potential application in radio frequency (RF) electronics[41,182,183,201].The Schottky nanodiodes with ultrathin ZnO films developed in this thesis can be potentially used in the design of integratable rectify circuit in RFID, diode bridge rectifier, etc. A rectifier is typically used to converts an alternating current (ac) input signal into a direct current (dc) supply voltage. A diode bridge circuit configuration is used for rectify circuit design with this ZnO SDs and shown in Figure 6.1. The rectify behavior characterization of the diode bridge is one of the interest in the development of ZnO based SDs' applications.

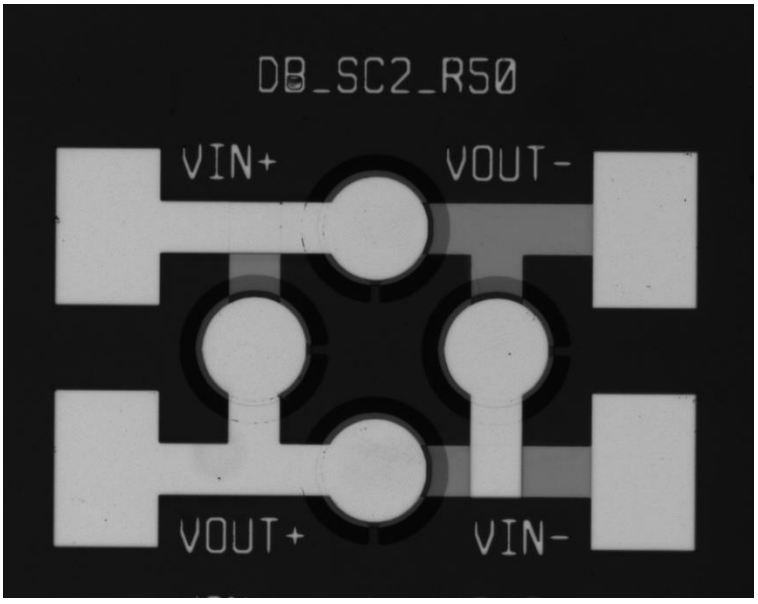

Figure 6.1. A fabricated diode bridge rectify with four Schottky nanodiodes configuration.

6.4.2.2 UV Photodiode

Optoelectronic device application, especially in the UV range, is one of the important research fields in transparent wide-gap semiconductor technology. Among various UV photodetector architectures including simple photoconductors, Schottky photodiodes, *p-n* photodiodes, MSM photodiodes, etc., the Schottky photodiode has an edge over others in the aspects of potential zero-bias operation, high UV/visible contrast, low dark current, high response speed and high quantum efficiency[130,202,203]. Transparent Schottky contacts based on ZnO with large potential barriers are promising for high performance UV photodetectors; however, the difficulty in fabricating a good Schottky contact with low leakage current on ZnO limits the performance of the ZnO Schottky photodiodes[47,93,166,204]. This Pt-50 Schottky contact developed in this work has shown large barrier height and low leakage current, which is promising to improve the photoresponsivity.

Bibliography

(1) Iwai, H. Introduction of New Materials into CMOS Devices. *ECS Trans.* **2013**, *50* (5), 13–20.

(2) Zhou, Y.; Ahyi, C.; Tin, C. C.; Williams, J.; Park, M.; Kim, D. J.; Cheng, A. J.; Wang, D.; Hanser, A.; Preble, E. A.; Williams, N. M.; Evans, K. Fabrication and Device Characteristics of Schottky-Type Bulk GaN-Based "visible-Blind" ultraviolet Photodetectors. *Appl. Phys. Lett.* **2007**, *90* (12).

(3) Yoder, M. Wide Bandgap Semiconductor Materials and Devices. *Electron Devices, IEEE Trans.* **1996**, *43* (10), 1633–1636.

(4) Agarwal, A.; Augustine, G.; Balakrishna, V.; Brandt, C. D.; Burk, A. A.; Chen, L.-S.; Clarke, R. C.; Esker, P. M.; Hobgood, H. M.; Hopkins, R. H.; Morse, A. W.; Rowland, L. B.; Seshadri, S.; Siergiej, R. R.; Smith, T. J.; Jr., Sriram, S. SiC Electronics. In *IEDM*; 1996; pp 225–230.

(5) Khan, A.; Balakrishnan, K.; Katona, T. Ultraviolet Light-Emitting Diodes Based on Group Three Nitrides. *Nat. Photonics* **2008**, 77–84.

(6) Lee, S. Y.; Park, K.-I.; Huh, C.; Koo, M.; Yoo, H. G.; Kim, S.; Ah, C. S.; Sung, G. Y.; Lee, K. J. Water-Resistant Flexible GaN LED on a Liquid Crystal Polymer Substrate for Implantable Biomedical Applications. *Nano Energy* **2012**, *1* (1), 145–151.

(7) Feng, Z. *III-Nitride: Semiconductor Materials*; 2006.

(8) King, D. S.; Nix, R. M. Thermal Stability and Reducibility of ZnO and Cu / ZnO Catalysts. **1996**, *83* (125), 76–83.

(9) Mridha, S.; Basak, D. Investigation of a P-CuO/n-ZnO Thin Film Heterojunction for H 2 Gas-Sensor Applications. *Semicond. Sci. Technol.* **2006**, *21* (7), 928–932.

(10) Minami, T. New N-Type Transparent Conducting Oxides. *MRS Bull.* **2000**, *25* (8), 38–44.

(11) Hu, W. S.; Liu, Z. G.; Wu, R. X.; Chen, Y.-F.; Ji, W.; Yu, T.; Feng, D. Preparation of Piezoelectric-Coefficient Modulated Multilayer Film ZnO/Al[sub 2]O[sub 3] and Its Ultrahigh Frequency Resonance. *Appl. Phys. Lett.* **1997**, *71* (4), 548.

(12) S. Ezhilvalavan and T. R. N. Kutty. Low-Voltage Varistors Based on Zinc Antimony Spinel Zn7Sb2O12. *Appl. Phys. Lett.* **1996**, *68* (19), 2693–2695.

(13) Feng, Z. C. *Handbook of Zinc Oxide and Related Materials: Volume Two, Devices and Nano-Engineering*; Taylor & Francis, 2012.

(14) Ohshima, E.; Ogino, H.; Niikura, I.; Maeda, K.; Sato, M.; Ito, M.; Fukuda, T. Growth of the 2-in-Size Bulk ZnO Single Crystals by the Hydrothermal Method. *J. Cryst. Growth* **2004**, *260* (1–2), 166–170.

(15) Mycielski, A.; Kowalczyk, L.; Szadkowski, A.; Chwalisz, B.; Wysmołek, A.; Stępniewski, R.; Baranowski, J. M.; Potemski, M.; Witowski, A.; Jakieła, R.; Barcz, A.; Witkowska, B.; Kaliszek, W.; Jędrzejczak, A.; Suchocki, A.; Łusakowska, E.; Kamińska, E. The Chemical Vapour Transport Growth of ZnO Single Crystals. *J. Alloys Compd.* **2004**, *371* (1–2), 150–152.

(16) Nause, J. ZnO Broadens the Spectrum. *III-Vs Rev.* **1999**, *12* (4), 28–31.

(17) Makino, T.; Segawa, Y.; Kawasaki, M.; Ohtomo, A.; Shiroki, R.; Tamura, K.; Yasuda, T.; Koinuma, H. Band Gap Engineering Based on MgxZn1−xO and CdyZn1−yO Ternary Alloy Films. *Appl. Phys. Lett.* **2001**, *78* (9), 1237.

(18) Janotti, A.; Van De Walle, C. G. Oxygen Vacancies in ZnO. *Appl. Phys. Lett.* **2005**, *87* (12), 122102.

(19) Özgür, U.; Alivov, Y. I.; Liu, C.; Teke, A.; Reshchikov, M. A.; Doğan, S.; Avrutin, V.; Cho, S. J.; Morkoç, H. A Comprehensive Review of ZnO Materials and Devices. *J. Appl. Phys.* **2005**, *98* (4), 41301.

(20) Lc, N.; Box, P. O.; Allen, G. Markets for Zinc Oxide In Electronics NanoMarkets. **2009**, No. March.

(21) Ozgür, U.; Hofstetter, D.; Morkoç, H. ZnO Devices and Applications: A Review of Current Status and Future Prospects. *Proc. IEEE* **2010**, *98* (7), 1255–1268.

(22) Fortunato, E.; Barquinha, P.; Martins, R. Oxide Semiconductor Thin-Film Transistors: A Review of Recent Advances. *Adv. Mater.* **2012**, *24* (22), 2945–2986.

(23) Godlewski, M.; Guziewicz, E.; Łuka, G.; Krajewski, T.; Łukasiewicz, M.; Wachnicki; Wachnicka, A.; Kopalko, K.; Sarem, A.; Dalati, B. ZnO Layers Grown by Atomic Layer Deposition: A New Material for Transparent Conductive Oxide. *Thin Solid Films* **2009**, *518* (4), 1145–1148.

(24) Sivaramakrishnan, K.; Alford, T. L. Metallic Conductivity and the Role of Copper in ZnO/Cu/ZnO Thin Films for Flexible Electronics. *Appl. Phys. Lett.* **2009**, *94* (5), 52104.

(25) Zhang, S. B.; Wei, S.-H.; Zunger, A. Overcoming Doping Bottlenecks in Semiconductors and Wide-Gap Materials. *Phys. B Condens. Matter* **1999**, *273–274*, 976–980.

(26) Avrutin, V.; Silversmith, D. J.; Morkoc, H. Doping Asymmetry Problem in ZnO: Current Status and Outlook. *Proc. IEEE* **2010**, *98* (7), 1269–1280.

(27) Look, D. C.; Reynolds, D. C.; Litton, C. W.; Jones, R. L.; Eason, D. B.; Cantwell, G. Characterization of Homoepitaxial P-Type ZnO Grown by Molecular Beam Epitaxy. *Appl. Phys. Lett.* **2002**, *81* (10), 1830.

(28) Zhang, S.; Wei, S.-H.; Zunger, A. Intrinsic N-Type versus P-Type Doping Asymmetry and the Defect Physics of ZnO. *Phys. Rev. B* **2001**, *63* (7), 75205.

(29) Avrutin, V.; Silversmith, D.; Morkoç, H. Doping Asymmetry Problem in ZnO: Current

Status and Outlook. *Proc. IEEE* **2010**, *98* (7), 1269–1280.

(30) Chris G. Van de Walle. Hydrogen as a Cause of Doping in Zinc Oxide. *Phys. Rev. Lett.* **2000**, *85* (5), 1012–1015.

(31) Janotti, A.; Van de Walle, C. G. Fundamentals of Zinc Oxide as a Semiconductor. *Reports Prog. Phys.* **2009**, *72* (12), 126501.

(32) Sun, Y. W.; Tsui, Y. Y. Production of Porous Nanostructured Zinc Oxide Thin Films by Pulsed Laser Deposition. *Opt. Mater. (Amst).* **2007**, *29* (8), 1111–1114.

(33) Johnson, E. Physical Limitations on Frequency and Power Parameters of Transistors. *IRE Int. Conv. Rec.* **1966**, *13*, 27–34.

(34) Keys, R. W. Figure of Merit for Semiconductors for High-Speed Switches. In *Proceedings of the IEEE*; 1972; p 225.

(35) Baliga, B. J. Semiconductors for High-Voltage, Vertical Channel Field-Effect Transistors. *J. Appl. Phys.* **1982**, *53* (3), 1759–1764.

(36) Baliga, B. J. Power Semiconductor Device Figure of Merit for High-Frequency Applications. *IEEE Electron Device Lett.* **1989**, *10* (10), 455–457.

(37) Wang, L.-M. Relationship Between Intrinsic Breakdown Field and Bandgap of Materials. In *25th International Conference on Microelectronics*; 2006.

(38) Nomura, K. Thin-Film Transistor Fabricated in Single-Crystalline Transparent Oxide Semiconductor. *Science (80-.).* **2003**, *300* (5623), 1269–1272.

(39) Ito, M.; Kon, M.; Miyazaki, C.; Ikeda, N.; Ishizaki, M.; Ugajin, Y.; Sekine, N. "Front Drive" Display Structure for Color Electronic Paper Using Fully Transparent Amorphous Oxide TFT Array. *IEICE Trans. Electron.* **2007**, *E90–C* (11), 2105–2111.

(40) Lim, S. J.; Kwon, S. J.; Kim, H.; Park, J. S. High Performance Thin Film Transistor with Low Temperature Atomic Layer Deposition Nitrogen-Doped ZnO. *Appl. Phys. Lett.* **2007**, *91* (18), 1–4.

(41) Semple, J.; Rossbauer, S.; Burgess, C. H.; Zhao, K.; Jagadamma, L. K.; Amassian, A.; McLachlan, M. A.; Anthopoulos, T. D. Radio Frequency Coplanar ZnO Schottky Nanodiodes Processed from Solution on Plastic Substrates. *Small* **2016**, *12* (15), 1993–2000.

(42) Shannon, J. M.; Balon, F. Source-Gated Thin-Film Transistors. *Solid. State. Electron.* **2008**, *52* (3), 449–454.

(43) Ma, A. M.; Gupta, M.; Afshar, A.; Shoute, G.; Tsui, Y. Y.; Cadien, K. C.; Barlage, D. W. Schottky Barrier Source-Gated ZnO Thin Film Transistors by Low Temperature Atomic Layer Deposition. *Appl. Phys. Lett.* **2013**, *103* (25), 253503.

(44) Huby, N.; Tallarida, G.; Kutrzeba, M.; Ferrari, S.; Guziewicz, E.; Wachnicki; Godlewski,

M. New Selector Based on Zinc Oxide Grown by Low Temperature Atomic Layer Deposition for Vertically Stacked Non-Volatile Memory Devices. *Microelectron. Eng.* **2008**, *85* (12), 2442–2444.

(45) Tsai, C.; Lee, C. Thermal Reliability and Performances of InGaP Schottky Contact with Cu/Au and Au/Cu-MSM Photodetectors. *J. Electron. Mater.* **2001**, *30* (2), 59–64.

(46) Jin, Y.; Wang, J.; Sun, B.; Blakesley, J. C.; Greenham, N. C. Solution-Processed Ultraviolet Photodetectors Based on Colloidal ZnO Nanoparticles. *Nano Lett.* **2008**, *8* (6), 1649–1653.

(47) Nakano, M.; Makino, T.; Tsukazaki, a.; Ueno, K.; Ohtomo, a.; Fukumura, T.; Yuji, H.; Akasaka, S.; Tamura, K.; Nakahara, K.; Tanabe, T.; Kamisawa, a.; Kawasaki, M. Transparent Polymer Schottky Contact for a High Performance Visible-Blind Ultraviolet Photodiode Based on ZnO. *Appl. Phys. Lett.* **2008**, *93* (12), 123309.

(48) Mead, C. A. Surface Barriers on ZnSe and ZnO. *Phys. Lett.* **1965**, *18* (3), 218.

(49) Fabricius, H.; Skettrup, T.; Bisgaard, P. Ultraviolet Detectors in Thin Sputtered ZnO Films. *Appl. Opt.* **1986**, *25* (16), 2764–2767.

(50) Allen, M. W.; Durbin, S. M. Influence of Oxygen Vacancies on Schottky Contacts to ZnO. *Appl. Phys. Lett.* **2008**, *92* (12), 90–93.

(51) Mosbacker, H. L.; Strzhemechny, Y. M.; White, B. D.; Smith, P. E.; Look, D. C.; Reynolds, D. C.; Litton, C. W.; Brillson, L. J. Role of near-Surface States in Ohmic-Schottky Conversion of Au Contacts to ZnO. *Appl. Phys. Lett.* **2005**, *87* (1), 78–81.

(52) Kim, S. H.; Kim, H. K.; Seong, T. Y. Effect of Hydrogen Peroxide Treatment on the Characteristics of Pt Schottky Contact on N-Type ZnO. *Appl. Phys. Lett.* **2005**, *86* (11), 112101.

(53) Schifano, R.; Monakhov, E. V; Grossner, U.; Svensson, B. G.; Schifano, R.; Monakhov, E. V; Grossner, U.; Svensson, B. G. Electrical Characteristics of Palladium Schottky Contacts to Hydrogen Peroxide Treated Hydrothermally Grown ZnO Electrical Characteristics of Palladium Schottky Contacts to Hydrogen Peroxide Treated Hydrothermally Grown ZnO. **2007**, *193507*, 19–22.

(54) Coppa, B. J.; Davis, R. F.; Nemanich, R. J. Gold Schottky Contacts on Oxygen Plasma-Treated, N-Type ZnO(000$\bar{1}$). *Appl. Phys. Lett.* **2003**, *82* (3), 400.

(55) Moormann, H.; Kohl, D.; Heiland, G. The Variation of Electron Affinity by Annealing. **1980**, *100*, 302–314.

(56) Coppa, B. J.; Fulton, C. C.; Kiesel, S. M.; Davis, R. F.; Pandarinath, C.; Burnette, J. E.; Nemanich, R. J.; Smith, D. J. Structural, Microstructural, and Electrical Properties of Gold Films and Schottky Contacts on Remote Plasma-Cleaned, N -Type ZnO{0001} Surfaces. *J. Appl. Phys.* **2005**, *97* (10), 103517.

(57) Brillson, L. J.; Mosbacker, H. L.; Hetzer, M. J.; Strzhemechny, Y.; Jessen, G. H.; Look, D. C.; Cantwell, G.; Zhang, J.; Song, J. J. Dominant Effect of near-Interface Native Point Defects on ZnO Schottky Barriers. *Appl. Phys. Lett.* **2007**, *90* (10), 102116.

(58) Kim, S. H.; Kim, H. K.; Seong, T. Y. Electrical Characteristics of Pt Schottky Contacts on Sulfide-Treated N -Type ZnO. *Appl. Phys. Lett.* **2005**, *86* (2), 22101.

(59) Polyakov, A. Y. Smirnov, N. B.; Kozhukhova, E. A. Vdovin, V. I. Ip, K. Heo, Y. W. Norton, D. P. Pearton, S. J. Electrical Characteristics of Au and Ag Schottky Contacts on N-ZnO. *Appl. Phys. Lett.* **2003**, *83* (8), 1575–1577.

(60) K. Ip, G.T. Thaler, Hyucksoo Yang, Sang Youn Han, Yuanjie Li, D.P. Norton, S.J. Pearton, Soowhan Jang, F. R. Contacts to ZnO. *J. Cryst. Growth* **2006**, *287* (1), 149–156.

(61) Frenzel, H.; Lajn, A.; Von Wenckstern, H.; Lorenz, M.; Schein, F.; Zhang, Z.; Grundmann, M. Recent Progress on ZnO-Based Metal-Semiconductor Field-Effect Transistors and Their Application in Transparent Integrated Circuits. *Adv. Mater.* **2010**, *22* (47), 5332–5349.

(62) Kim, S.; Kang, B. S.; Ren, F.; Ip, K.; Heo, Y. W.; Norton, D. P.; Pearton, S. J. Sensitivity of Pt/ZnO Schottky Diode Characteristics to Hydrogen. *Appl. Phys. Lett.* **2004**, *84* (10), 1698–1700.

(63) Ip, K.; Heo, Y. W.; Baik, K. H.; Norton, D. P.; Pearton, S. J.; Kim, S.; LaRoche, J. R.; Ren, F. Temperature-Dependent Characteristics of Pt Schottky Contacts on N-Type ZnO. *Appl. Phys. Lett.* **2004**, *84* (15), 2835–2837.

(64) Ip, K.; Gila, B. P. Onstine, A. H. Lambers, E. S. Heo, Y. W. Baik, K. H.; Norton, D. P.; Pearton, S. J. Kim, S. LaRoche, J. R.; Ren, F. Improved Pt⁄Au and W⁄Pt⁄Au Schottky Contacts on N-Type ZnO Using Ozone Cleaning. *Appl. Phys. Lett.* **2004**, *84* (25), 5133–5135.

(65) Hyland, A. M.; Makin, R. A.; Durbin, S. M.; Allen, M. W. Giant Improvement in the Rectifying Performance of Oxidized Schottky Contacts to ZnO. *J. Appl. Phys.* **2017**, *121* (2), 24501.

(66) Young, S. J.; Ji, L. W.; Chang, S. J.; Chen, Y. P.; Peng, S. M. ZnO Schottky Diodes with Iridium Contact Electrodes. *Semicond. Sci. Technol.* **2008**, *23* (8), 85016.

(67) Hwang, J. D.; Kung, C. Y.; Lin, Y. L. Non-Surface-Treated Au/ZnO Schottky Diodes Using Pre-Annealed Hydrothermal or Sol-Gel Seed Layer. *IEEE Trans. Nanotechnol.* **2013**, *12* (1), 35–39.

(68) Somvanshi, D.; Jit, S. Effect of ZnO Seed Layer on the Electrical Characteristics of Pd/ZnO Thin-Film-Based Schottky Contacts Grown on N-Si Substrates. *IEEE Trans. Nanotechnol.* **2014**, *13* (6), 1138–1144.

(69) Aydoğan, Ş.; Çinar, K.; Asil, H.; Coşkun, C.; Türüt, A. Electrical Characterization of Au/n-ZnO Schottky Contacts on N-Si. *J. Alloys Compd.* **2009**, *476* (1), 913–918.

(70) Wenckstern, H. v.; Biehne, G.; Rahman, R. A.; Hochmuth, H.; Lorenz, M.; Grundmann, M. Mean Barrier Height of Pd Schottky Contacts on ZnO Thin Films. *Appl. Phys. Lett.* **2006**, *88* (9), 92102.

(71) Lajn, A.; Wenckstern, H. v.; Zhang, Z.; Czekalla, C.; Biehne, G.; Lenzner, J.; Hochmuth, H.; Lorenz, M.; Grundmann, M.; Wickert, S.; Vogt, C.; Denecke, R. Properties of Reactively Sputtered Ag, Au, Pd, and Pt Schottky Contacts on N-Type ZnO. *J. Vac. Sci. Technol. B Microelectron. Nanom. Struct.* **2009**, *27* (3), 1769–1773.

(72) Zhang, Q.; Cicek, P.-V.; Allidina, K.; Nabki, F.; El-Gamal, M. N. E.-G. Surface-Micromachined CMUT Using Low-Temperature Deposited Silicon Carbide Membranes for Above-IC Integration. *J. Microelectromechanical Syst.* **2014**, *23* (2), 482–493.

(73) Klüpfel, F. J.; Schein, F.; Lorenz, M.; Frenzel, H.; Wenckstern, H. v.; Grundmann, M. Comparison of ZnO-Based JFET. *IEEE Trans. Electron Devices* **2013**, *60* (6), 1828–1833.

(74) Frenzel, H.; Lajn, A.; Brandt, M.; Wenckstern, H. v; Biehne, G.; Hochmuth, H.; Lorenz, M.; Grundmann, M. ZnO Metal-Semiconductor Field-Effect Transistors with Ag-Schottky Gates. *Appl. Phys. Lett.* **2008**, *92* (19), 192108.

(75) Frenzel, H.; Lajn, A.; Wenckstern, H. v.; Biehne, G.; Hochmuth, H.; Grundmann, M. ZnO-Based Metal-Semiconductor Field-Effect Transistors with Ag-, Pt-, Pd-, and Au-Schottky Gates. *Thin Solid Films* **2009**, *518* (4), 1119–1123.

(76) Klupfel, F. J.; Wenckstern, H. v.; Grundmann, M. Ring Oscillators Based on ZnO Channel JFETs and MESFETs. *Adv. Electron. Mater.* **2016**, *2* (7), 1500431.

(77) Jin, J.; Wrench, J. S.; Gibbon, J. T.; Hesp, D.; Shaw, A.; Mitrovic, I. Z.; Sedghi, N.; Phillips, L. J.; Zou, J.; Dhanak, V. R.; Chalker, P. R.; Hall, S. Schottky Diodes on ZnO Thin Films Grown by Plasma-Enhanced Atomic Layer Deposition. *IEEE Trans. Electron Devices* **2017**, *64* (3), 1225–1230.

(78) Nomura, K.; Ohta, H.; Takagi, A.; Kamiya, T.; Hirano, M.; Hosono, H. Room-Temperature Fabrication of Transparent Flexible Thin-Film Transistors Using Amorphous Oxide Semiconductors. *Nature* **2004**, *432* (7016), 488–492.

(79) *The Flexible Electronics Opportunity*; Siegel, D., Shivakumar, S., Eds.; THE NATIONAL ACADEMIES PRESS: Washington, 2014.

(80) Sun, Y.; Rogers, J. A. Inorganic Semiconductors for Flexible Electronics. *Adv. Mater.* **2007**, *19* (15), 1897–1916.

(81) Carcia, P. F.; McLean, R. S.; Reilly, M. H. Oxide Engineering of ZnO Thin-Film Transistors for Flexible Electronics. *J. Soc. Inf. Disp.* **2005**, *13* (7), 547.

(82) Li, H. U.; Jackson, T. N. Flexibility Testing Strategies and Apparatus for Flexible Electronics. *IEEE Trans. Electron Devices* **2016**, *63* (5), 1934–1939.

(83) Lin, Y. Y.; Hsu, C. C.; Tseng, M. H.; Shyue, J. J.; Tsai, F. Y. Stable and High-

Performance Flexible ZnO Thin-Film Transistors by Atomic Layer Deposition. *ACS Appl. Mater. Interfaces* **2015**, *7* (40), 22610–22617.

(84) Ji, Z.; Mao, Q.; Ke, W. Effects of Oxygen Partial Pressure on Resistive Switching Characteristics of ZnO Thin Films by DC Reactive Magnetron Sputtering. *Solid State Commun.* **2010**, *150* (39–40), 1919–1922.

(85) Wendt, R.; Ellmer, K.; Wiesemann, K. Thermal Power at a Substrate during ZnO: Al Thin Film Deposition in a Planar Magnetron Sputtering System. *J. Appl. Phys.* **1997**, *82* (5), 2115–2122.

(86) Ivanova, T.; Harizanova, A.; Koutzarova, T.; Vertruyen, B. Study of ZnO Sol – Gel Films : Effect of Annealing. **2010**, *64*, 1147–1149.

(87) Kyaw, A. K. K.; Sun, X. W.; Jiang, C. Y.; Lo, G. Q.; Zhao, D. W.; Kwong, D. L. An Inverted Organic Solar Cell Employing a Sol-Gel Derived ZnO Electron Selective Layer and Thermal Evaporated MoO3 Hole Selective Layer. *Appl. Phys. Lett.* **2008**, *93* (22), 2006–2009.

(88) Asakuma, N.; Hirashima, H.; Imai, H.; Fukui, T.; Toki, M. Crystallization and Reduction of Sol-Gel-Derived Zinc Oxide Films by Irradiation with Ultraviolet Lamp. *J. Sol-Gel Sci. Technol.* **2003**, *26* (1), 181–184.

(89) Kaidashev, E. M.; Lorenz, M.; Von Wenckstern, H.; Rahm, a.; Semmelhack, H.-C. C.; Han, K.-H. H.; Benndorf, G.; Bundesmann, C.; Hochmuth, H.; Grundmann, M. High Electron Mobility of Epitaxial ZnO Thin Films on c-Plane Sapphire Grown by Multistep Pulsed-Laser Deposition. *Appl. Phys. Lett.* **2003**, *82* (22), 3901.

(90) Matsubara, K.; Fons, P.; Iwata, K.; Yamada, A.; Sakurai, K.; Tampo, H.; Niki, S. ZnO Transparent Conducting Films Deposited by Pulsed Laser Deposition for Solar Cell Applications. *Thin Solid Films* **2003**, *431*, 369–372.

(91) Casteleiro, C.; Gomes, H. L.; Stallinga, P.; Bentes, L.; Ayouchi, R.; Schwarz, R. Study of Trap States in Zinc Oxide (ZnO) Thin Films for Electronic Applications. *J. Non. Cryst. Solids* **2008**, *354* (19–25), 2519–2522.

(92) Sun, Y. W.; Gospodyn, J.; Kursa, P.; Sit, J.; DeCorby, R. G.; Tsui, Y. Y. Dense and Porous ZnO Thin Films Produced by Pulsed Laser Deposition. *Appl. Surf. Sci.* **2005**, *248* (1–4), 392–396.

(93) Liang, S.; Sheng, H.; Liu, Y.; Huo, Z.; Lu, Y.; Shen, H. ZnO Schottky Ultraviolet Photodetectors. *J. Cryst. Growth* **2001**, *225* (2), 110–113.

(94) Kim, D. C.; Han, W. S.; Cho, H. K.; Kong, B. H.; Kim, H. S. Multidimensional ZnO Light-Emitting Diode Structures Grown by Metal Organic Chemical Vapor Deposition on P-Si. *Appl. Phys. Lett.* **2007**, *91* (23), 2005–2008.

(95) Oh, D. C.; Kim, J. J.; Makino, H.; Hanada, T.; Cho, M. W.; Yao, T.; Ko, H. J. Characteristics of Schottky Contacts to ZnO:N Layers Grown by Molecular-Beam

Epitaxy. *Appl. Phys. Lett.* **2005**, *86* (4), 1–4.

(96) Muneshwar, T.; Shoute, G.; Barlage, D.; Cadien, K. Plasma Enhanced Atomic Layer Deposition of ZnO with Diethyl Zinc and Oxygen Plasma : Effect of Precursor Decomposition Plasma Enhanced Atomic Layer Deposition of ZnO with Diethyl Zinc and Oxygen Plasma : Effect of Precursor Decomposition. *J. Vac. Sci. Technol. A Vacuum, Surfaces, Film.* **2016**, *34* (5), 50605.

(97) Guziewicz, E.; Kowalik, I. A.; Godlewski, M.; Kopalko, K.; Osinniy, V.; Wójcik, A.; Yatsunenko, S.; Łusakowska, E.; Paszkowicz, W.; Guziewicz, M. Extremely Low Temperature Growth of ZnO by Atomic Layer Deposition. *J. Appl. Phys.* **2008**, *103* (3), 33515.

(98) Afshar, A.; Cadien, K. C. Growth Mechanism of Atomic Layer Deposition of Zinc Oxide: A Density Functional Theory Approach. *Appl. Phys. Lett.* **2013**, *103* (25), 251906.

(99) Guziewicz, E.; Godlewski, M.; Wachnicki, L.; Krajewski, T. A.; Luka, G.; Gieraltowska, S.; Jakiela, R.; Stonert, A.; Lisowski, W.; Krawczyk, M.; Sobczak, J. W.; Jablonski, A. ALD Grown Zinc Oxide with Controllable Electrical Properties. *Semicond. Sci. Technol.* **2012**, *27* (7), 74011.

(100) Orak, I.; Kocyigit, A.; Turut, A. The Surface Morphology Properties and Respond Illumination Impact of ZnO/n-Si Photodiode by Prepared Atomic Layer Deposition Technique. *J. Alloys Compd.* **2017**, *691*, 873–879.

(101) Kim, H.; Kim, D. H.; Ryu, S.; Choi, B. J. Metal/nonpolar M-Plane ZnO Contacts with and without Thin Al2O3 Interlayer Deposited by Atomic Layer Deposition. *J. Mater. Sci. Mater. Electron.* **2017**, 1–7.

(102) Krajewski, T. A.; Smertenko, P. S.; Luka, G.; Snigurenko, D.; Kopalko, K.; Lusakowska, E.; Jakiela, R.; Guziewicz, E. Tuning the Properties of ALD-ZnO-Based Rectifying Structures by Thin Dielectric Film Insertion – Modeling and Experimental Studies. *J. Alloys Compd.* **2017**, *693*, 1164–1173.

(103) Kocyigit, A.; Orak, I.; Çaldıran, Z.; Turut, A. Current–voltage Characteristics of Au/ZnO/n-Si Device in a Wide Range Temperature. *J. Mater. Sci. Mater. Electron.* **2017**, *0* (0), 1–8.

(104) Orak, İ. The Performances Photodiode and Diode of ZnO Thin Film by Atomic Layer Deposition Technique. *Solid State Commun.* **2016**, *247*, 17–22.

(105) Afshar, A. Materials Characterization and Growth Mechanisms of ZnO, ZrO2, and HfO2 Deposited by Atomic Layer Deposition, 2014.

(106) Weng, B.; Wang, J.; Larson, P.; Liu, Y. Growth Process Optimization of ZnO Thin Film Using Atomic Layer Deposition This. *Mater. Res. express* **2016**, *3*, 126402.

(107) Warren, B. E. *X-Ray Diffraction*; Courier Corporation, 1969.

(108) Juraić, K.; Gracin, D.; Djerdj, I.; Lausi, A.; Čeh, M.; Balzar, D. Structural Analysis of Amorphous-Nanocrystalline Silicon Thin Films by Grazing Incidence X-Ray Diffraction. *Nucl. Instruments Methods Phys. Res. Sect. B Beam Interact. with Mater. Atoms* **2012**, *284*, 78–82.

(109) Gupta, M.; Chowdhury, F. R.; Barlage, D.; Tsui, Y. Y. Optimization of Pulsed Laser Deposited ZnO Thin-Film Growth Parameters for Thin-Film Transistors (TFT) Application. *Appl. Phys. A* **2012**, *110* (4), 793–798.

(110) Boichot, R.; Tian, L.; Richard, M. I.; Crisci, A.; Chaker, A.; Cantelli, V.; Coindeau, S.; Lay, S.; Ouled, T.; Guichet, C.; Chu, M. H.; Aubert, N.; Ciatto, G.; Blanquet, E.; Thomas, O.; Deschanvres, J. L.; Fong, D. D.; Renevier, H. Evolution of Crystal Structure during the Initial Stages of ZnO Atomic Layer Deposition. *Chem. Mater.* **2016**, *28* (2), 592–600.

(111) Kohan, A. F.; Ceder, G.; Morgan, D.; Van De Walle, C. G. First-Principles Study of Native Point Defects in ZnO. *Phys. Rev. B - Condens. Matter Mater. Phys.* **2000**, *61* (22), 15019–15027.

(112) Van De Walle, C. G. Defect Analysis and Engineering in ZnO. *Phys. B Condens. Matter* **2001**, *308*, 899–903.

(113) Erhart, P.; Albe, K.; Klein, A. First-Principles Study of Intrinsic Point Defects in ZnO: Role of Band Structure, Volume Relaxation, and Finite-Size Effects. *Phys. Rev. B - Condens. Matter Mater. Phys.* **2006**, *73* (20), 205203.

(114) Krajewski, T. A.; Terziyska, P.; Luka, G.; Lusakowska, E.; Jakiela, R.; Vlakhov, E. S.; Guziewicz, E. Diversity of Contributions Leading to the Nominally N–type Behavior of ZnO Films Obtained by Low Temperature Atomic Layer Deposition. *J. Alloys Compd.* **2017**.

(115) Simpson, J. C.; Cordaro, J. F. Characterization of Deep Levels in Zinc Oxide. *J. Appl. Phys.* **1988**, *63* (5), 1781–1783.

(116) Donoval, D.; Barus, M.; Zdimal, M. Analysis of I–V Measurements on PtSi-Si Schottky Structures in a Wide Temperature Range. *Solid State Electron.* **1991**, *34* (12), 1365–1373.

(117) Biesinger, M. C.; Lau, L. W.; Gerson, A. R.; Smart, R. S. C. Resolving Surface Chemical States in XPS Analysis of First Row Transition Metals, Oxides and Hydroxides: Sc, Ti, V, Cu and Zn. *Appl. Surf. Sci.* **2010**, *257* (3), 887–898.

(118) Monakhov, E. V; Kuznetsov, a Y.; Svensson, B. G. Zinc Oxide: Bulk Growth, Role of Hydrogen and Schottky Diodes. *J. Phys. D. Appl. Phys.* **2009**, *42* (15), 153001.

(119) Pearton, S. J.; Norton, D. P.; Ip, K.; Heo, Y. W.; Steiner, T. Recent Progress in Processing and Properties of ZnO. *Superlattices Microstruct.* **2003**, *34* (1–2), 3–32.

(120) Braun, K. F. Uber Die Stromleitung Durch Schwefelmetalic. *Ann. der Phys. Chemie* **1874**, *153* (4), 556–563.

(121) Schottky, W. Semiconductor Theory in Barrier Layers. *Naturwissenschaften* **1938**, *26* (843), 280.

(122) Mott, N. F. Note On The Contact Between A Metal And An Insulator Or Semi-Conductor. *Math. Proc. Cambridge Philos. Soc.* **1938**, *4* (34), 568–572.

(123) Lee, S. K.; Zetterling, C. M.; Östling, M. Schottky Barrier Height Dependence on the Metal Work Function for P-Type 4H-Silicon Carbide. *J. Electron. Mater.* **2001**, *30* (3), 242–246.

(124) Tung, R. T. Formation of an Electric Dipole at Metal-Semiconductor Interfaces. *Phys. Rev. B* **2001**, *64* (20), 205310.

(125) Tung, R. T. The Physics and Chemistry of the Schottky Barrier Height. *Appl. Phys. Rev.* **2014**, *1* (1), 11304.

(126) Heine, V. Theory of Surface States. *Phys. Rev.* **1965**, *138* (6A), A1689–A1696.

(127) Tung, R. T. Chemical Bonding and Fermi Level Pinning at Metal-Semiconductor Interfaces. *Phys. Rev. Lett.* **2000**, *84* (26), 6078–6081.

(128) Schroder, D. K. *Semiconductor Material and Device Characterization*, 3rd ed.; 2006.

(129) Bethe, H. A. *Theory of the Boundary Layer of Crystal Rectifiers*; Radiation Laboratory, Massachusetts Institute of Technology, Cambridge, MA, 1942.

(130) Sze, S. M.; Ng, K. K. *Physics of Semiconductor Devices*; John wiley & sons, 2006.

(131) Rhoderick, E. H. ， R. H. W. Metal-Semiconductor Contacts. *Phys. Technol.* **1988**, *5* (4), 223–223.

(132) Norde, H. A Modified Forward I-V Plot for Schottky Diodes with High Series Resistance. *J. Appl. Phys.* **1979**, *50* (7), 5052–5053.

(133) Sato, K.; Yasumura, Y. Study of Forward I-V Plot for Schottky Diodes with High Series Resistance. *J. Appl. Phys.* **1985**, *58* (9), 3655–3657.

(134) Cheung, S. K.; Cheung, N. W. Extraction of Schottky Diode Parameters from Forward Current-Voltage Characteristics. *Appl. Phys. Lett.* **1986**, *49* (2), 85–87.

(135) REUBEN HACKAM AND PETER PIARROP. Electrical Properties of Nickel-LowcDoped N-Type Gallium Arsenide Schottky-Barrier Diodes. *IIEEE Trans. ELECTRON DEVICES* **1972**, *ED-19* (12), 1231–1238.

(136) Bhuiyan, A. S.; Martinez, A.; Esteve, D. A New Richardson Plot for Non-Ideal Schottky Diodes. *Thin Solid Films* **1988**, *161* (C), 93–100.

(137) Ambacher, O.; Smart, J. Two-Dimensional Electron Gases Induced by Spontaneous and Piezoelectric Polarization Charges in N-and Ga-Face AlGaN/GaN Heterostructures. *J. Appl. Phys.* **1999**, *85* (6), 3222.

(138) Hussain, I.; Soomro, M. Y.; Bano, N.; Nur, O.; Willander, M. Interface Trap Characterization and Electrical Properties of Au-ZnO Nanorod Schottky Diodes by Conductance and Capacitance Methods. *J. Appl. Phys.* **2012**, *112* (6), 64506.

(139) Hermans, M. H. E. Origin of Capacitance Excess at Intimate Schottky Contacts. *Phys. Rev. Lett.* **1988**, *60* (1), 53–56.

(140) Telia, A.; Meziani, A. Analysis of Trap States Effects on the Frequency- Dependent Capacitance and Conductance of an AlGaN / GaN Heterostructure. In *International Conference on Signals, Circuits and Systems*; 2008; pp 2–6.

(141) Vogel, E. M.; Kirklen Henson, W.; Richter, C. A.; Suehle, J. S. Limitations of Conductance to the Measurement of the Interface State Density of MOS Capacitors with Tunneling Gate Dielectrics. *IEEE Trans. Electron Devices* **2000**, *47* (3), 601–608.

(142) Aydogan, S.; Saglam, M.; Turut, A. Characterization of Capacitance-Frequency Features of Sn/polypyrrole/n-Si Structure as a Function of Temperature. *Polymer (Guildf).* **2005**, *46* (16), 6148–6153.

(143) Sze, S. M.; Crowell, C. R.; Kahng, D. Photoelectric Determination of the Image Force Dielectric Constant for Hot Electrons in Schottky Barriers. *J. Appl. Phys.* **1964**, *35* (8), 2534–2536.

(144) Padovani, F. A.; Stratton, R. Field and Thermionic-Field Emission in Schottky Barriers. *Solid. State. Electron.* **1966**, *9* (7), 695–707.

(145) Tung, R. T. Electron Transport of Inhomogeneous Schottky Barriers. **1991**, *56* (24), 2821–2823.

(146) Tanabe, A.; Konuma, K.; Teranishi, N.; Tohyama, S.; Masubuchi, K. Influence of Fermi-Level Pinning on Barrier Height Inhomogeneity in PtSi / P-Si Schottky Contacts L-. **1991**, *850* (May 2007), 850–853.

(147) Okumura, T.; Tu, K. N. Analysis of Parallel Schottky Contacts by Differential Internal Photoemission Spectroscopy. *J. Appl. Phys.* **1983**, *54* (2), 922–927.

(148) Engstrom, O.; Pettersson, H.; Sernelius, B. Photoelectric Yield Spectra of Metal-Semiconductor Structures. *Phys. Status Solidi* **1986**, *95* (2), 691–701.

(149) Bell, L. D.; Kaiser, W. J. Observation of Interface Band Structure by Ballistic-Electron-Emission Microscopy. *Phys. Rev. Lett.* **1988**, *61* (20), 2368–2371.

(150) Hecht, M. H.; Bell, L. D.; Kaiser, W. J.; Grunthaner, F. J. Ballistic-Electron-Emission Microscopy Investigation of Schottky Barrier Interface Formation. *Appl. Phys. Lett.* **1989**, *55* (8), 780–782.

(151) Song, Y. P.; Van Meirhaeghe, R. L.; Laflere, W. H.; Cardon, F. On the Difference in Apparent Barrier Height as Obtained from Capacitance-Voltage and Current-Voltage-Temperature Measurements on Al/p-InP Schottky Barriers. *Solid State Electron.* **1986**, *29*

(6), 633–638.

(152) Aydoğan, Ş.; Sağlam, M.; Türüt, A. On the Barrier Inhomogeneities of Polyaniline/p-Si/Al Structure at Low Temperature. *Appl. Surf. Sci.* **2005**, *250* (1–4), 43–49.

(153) Werner, J. H.; Güttler, H. H. Barrier Inhomogeneities at Schottky Contacts. *J. Appl. Phys.* **1991**, *69* (3), 1522–1533.

(154) Mtangi, W.; Auret, F. D.; Nyamhere, C.; Janse van Rensburg, P. J.; Chawanda, M. Diale, A. Analysis of Temperature Dependent I - V Measurements on Pd/ZnO Schottky Barrier Diodes and the Determination of the Richardson Constant. *Phys. B Condens. Matter* **2009**, *404* (8), 1092–1096.

(155) Yuan, G.; Ye, Z.; Zhu, L.; Huang, J.; Qian, Q.; Zhao, B. Gold Schottky Contacts on N-Type ZnO Thin Films with an Al/Si(100) Substrates. *J. Cryst. Growth* **2004**, *268* (1–2), 169–173.

(156) Nakano, M.; Tsukazaki, a.; Gunji, R. Y.; Ueno, K.; Ohtomo, a.; Fukumura, T.; Kawasaki, M. Schottky Contact on a ZnO (0001) Single Crystal with Conducting Polymer. *Appl. Phys. Lett.* **2007**, *91* (14), 142113.

(157) Somvanshi, D.; Jit, S.; Member, S. Mean Barrier Height and Richardson Constant for Pd / ZnO Thin Film-Based Schottky Diodes Grown on N-Si Substrates by Thermal Evaporation Method. *IEEE Electron Device Lett.* **2013**, *34* (10), 1238–1240.

(158) Yadav, A. B.; Pandey, A.; Jit, S. Pd Schottky Contacts on Sol-Gel Derived ZnO Thin Films with Nearly Ideal Richardson Constant. *IEEE Electron Device Lett.* **2014**, *35* (7), 729–731.

(159) Lien, Y.-C.; Chang, E. Y.; Chen, S.-H.; Chu, L.-H.; Chen, P.-C.; Hsieh, Y.-C. Thermal Stability of Ti/Pt/Cu Schottky Contact on InAlAs Layer. *Appl. Phys. Lett.* **2006**, *89* (8), 83517-083517–3.

(160) Hyland, A. M.; Reeves, R. J.; Makin, R. A.; Durbin, S. M.; Allen, M. W. Thermal Stability of Oxidized Noble Metal Schottky Contacts to ZnO. In *Materials Science in Semiconductor Processing*; Elsevier, 2017; pp 1–4.

(161) Allen, M. W.; Weng, X.; Redwing, J. M.; Sarpatwari, K.; Mohney, S. E.; von Wenckstern, H.; Grundmann, M.; Durbin, S. M. Temperature-Dependent Properties of Nearly Ideal ZnO Schottky Diodes. *IEEE Trans. Electron Devices* **2009**, *56* (9), 2160–2164.

(162) Auret, F. D.; Goodman, S. A.; Hayes, M.; Legodi, M. J.; Van Laarhoven, H. A.; Look, D. C. Electrical Characterization of 1.8 MeV Proton-Bombarded ZnO. *Appl. Phys. Lett.* **2001**, *79* (19), 3074–3076.

(163) Ohashi, N.; Tanaka, J.; Ohgaki, T.; Haneda, H.; Ozawa, M.; Tsurumi, T. Isothermal Capacitance Transient Spectroscopy for Deep Levels in Co- and Mn-Doped ZnO Single Crystals. *J. Mater. Res.* **2002**, *17* (6), 1529–1535.

(164) Neville, R. C.; Mead, C. A. Surface Barriers on Zinc Oxide. *J. Appl. Phys.* **1970**, *41* (9), 3795–3800.

(165) Shen, M.; Afshar, A.; Gupta, M.; Shoute, G.; Cadien, K.; Tsui, Y. Y.; Barlage, D. Electrical Characteristics of TiW/ZnO Schottky Contact with ALD and PLD. *Mater. Res. Soc. Symp. Proc.* **2014**, *1635*, 127–132.

(166) Endo, H.; Sugibuchi, M.; Takahashi, K.; Goto, S.; Sugimura, S.; Hane, K.; Kashiwaba, Y. Schottky Ultraviolet Photodiode Using a ZnO Hydrothermally Grown Single Crystal Substrate. *Appl. Phys. Lett.* **2007**, *90* (12), 1–4.

(167) Klason, P.; Nur, O.; Willander, M. Electrical Characteristics and Stability of Gold and Palladium Schottky Contacts on ZnO Nanorods. *Nanotechnology* **2008**, *19* (47), 475202.

(168) Shen, M.; Afshar, A.; Tsui, Y. Y.; Member, S.; Cadien, K. C.; Barlage, D. W. Performance of Nanocrystal ZnO Thin-Film Schottky Contacts on Cu by Atomic Layer Deposition. **2017**, *16* (1), 135–139.

(169) Baliga, B. J. *Fundamentals of Power Semiconductor Devices*; Springer, 2010.

(170) Han, D.; Kim, Y.; Shim, J.; Shin, D. Forward-Capacitance Measurement on Wide-Bandgap Light-Emitting Diodes. *IEEE Photonics Technol. Lett.* **2016**, *28* (21), 2407–2410.

(171) Kim, H.-K.; Han, S.-H.; Seong, T.-Y.; Choi, W.-K. Electrical and Structural Properties of Ti/Au Ohmic Contacts to N-ZnO. *J. Electrochem. Soc.* **2001**, *148* (3), G114–G117.

(172) Chyan, O.; Arunagiri, T. N.; Ponnuswamy, T. Electrodeposition of Copper Thin Film on Ruthenium a Potential Diffusion Barrier for Cu Interconnects. *J. Electrochem. Soc.* **2003**, *150* (5), C347–C350.

(173) Poulston, S.; Parlett, P. M.; Stone, P.; Bowker, M. Surface Oxidation and Reduction of CuO and Cu2O Studied Using XPS and XAES. *Surf. Interface Anal.* **1996**, *24* (12), 811–820.

(174) Tobin, J. P.; Hirschwald, W.; Cunningham, J. XPS and XAES Studies of Transient Enhancement of Cu1 at CuO Surfaces during Vacuum Outgassing. *Appl. Surf. Sci.* **1983**, *16* (3), 441–452.

(175) Siol, S.; Hellmann, J. C.; Tilley, S. D.; Graetzel, M.; Morasch, J.; Deuermeier, J.; Jaegermann, W.; Klein, A. Band Alignment Engineering at Cu2O/ZnO Heterointerfaces. *ACS Appl. Mater. Interfaces* **2016**, *8* (33), 21824–21831.

(176) Speight, J. G. *Lange's Handbook of Chemistry*; McGraw-Hill New York, 2005; Vol. 1.

(177) Alay, J. L.; Bender, H.; Brijs, G.; Demesmaeker, A.; Vandervorst, W. Quantitative Analysis of W(N), TiW and TiW(N) Matrices Using XPS, AES, RBS, EPMA and XRD. *Surf. Interface Anal.* **1991**, *17* (6), 373–382.

(178) Crowell, C.; Sze, S. M. Current Transport in Metal-Semiconductor Barriers. *Solid. State.*

Electron. **1966**, *9*, 1035–1048.

(179) Crowell, C. R.; Shore, H. B.; LaBate, E. E. Surface-State and Interface Effects in Schottky Barriers at N-Type Silicon Surfaces. *J. Appl. Phys.* **1965**, *36* (12), 3843–3850.

(180) Zheng, X. G.; Sakurai, Y.; Okayama, Y.; Yang, T. Q.; Zhang, L. Y.; Yao, X.; Nonaka, K.; Xu, C. N. Dielectric Measurement to Probe Electron Ordering and Electron-Spin Interaction. *J. Appl. Phys.* **2002**, *92* (5), 2703–2708.

(181) Allen, M. W.; Alkaisi, M. M.; Durbin, S. M. Metal Schottky Diodes on Zn-Polar and O-Polar Bulk ZnO. *Appl. Phys. Lett.* **2006**, *89* (10), 103520.

(182) Zhang, J.; Wang, H.; Wilson, J.; Ma, X.; Jin, J.; Song, A. Room Temperature Processed Ultrahigh-Frequency Indium-Gallium-Zinc-Oxide Schottky Diode. *IEEE Electron Device Lett.* **2016**, *37* (4), 389–392.

(183) Semple, J.; Rossbauer, S.; Anthopoulos, T. D. Analysis of Schottky Contact Formation in Coplanar Au/ZnO/Al Nanogap Radio Frequency Diodes Processed from Solution at Low Temperature. *ACS Appl. Mater. Interfaces* **2016**, *8* (35), 23167–23174.

(184) Scharfetter, D. L. Minority Carrier Injection and Charge Storage in Epitaxial Schottky Barrier Diodes. *Solid. State. Electron.* **1965**, *8* (3), 299–311.

(185) Yu, A. Y. C.; Snow, E. H.; Alto, P. Injection Contacts of Metal-Silicon. *Solid. State. Electron.* **1969**, *12*.

(186) Green, M. A.; Shewchun, J. Minority Carrier Effects upon the Small Signal and Steady-State Properties of Schottky Diodes. *Solid State Electron.* **1973**, *16* (10), 1141–1150.

(187) Rose, A. Space-Charge-Limited Currents in Solids. *Phys. Rev.* **1955**, *97* (6), 1538–1544.

(188) Gao, Y.; Marín, L.; Mattson, E. C.; Cure, J.; Nanayakkara, C. E.; Veyan, J. F.; Lucero, A. T.; Kim, J.; Rossi, C.; Estève, A.; Chabal, Y. J. Basic Mechanisms of Al Interaction with the ZnO Surface. *J. Phys. Chem. C* **2017**, *121* (23), 12780–12788.

(189) Ozbek, a. M.; Baliga, B. J. Tunneling Coefficient for GaN Schottky Barrier Diodes. *Solid. State. Electron.* **2011**, *62* (1), 1–4.

(190) Stratton, R. Tunneling in Schottky Barrier Rectifiers. In *Tunneling Phenomena in Solids*; Elias Burstein, S. L., Ed.; Springer US, 1969; pp 105–125.

(191) Duke, C. B. Theory of Metal-Barrier-Metal Tunneling. In *Tunneling Phenomena in Solids*; Elias Burstein, S. L., Ed.; Springer US, 1969; pp 31–46.

(192) Chu, J. L.; Persky, G.; Sze, S. M. Thermionic Injection and Space-Charge-Limited Current in Reach-through P+np+ Structures. *J. Appl. Phys.* **1972**, *43* (8), 3510–3515.

(193) Messiah, A. *Quantum Mechanics*; Dover books on physics; Dover Publications, 1961.

(194) Chandra, A.; Eastman, L. F. Quantum Mechanical Reflection at Triangular “planar-

Doped" potential Barriers for Transistors. *J. Appl. Phys.* **1982**, *53* (12), 9165–9169.

(195) Gundlach, K. H. Zur Berechnung Des Tunnelstroms Durch Eine Trapezförmige Potentialstufe. *Solid. State. Electron.* **1966**, *9* (10), 949–957.

(196) Gain, J.; Sarkar, M.; Kundu, S. Energy and Effective Mass Dependence of Electron Tunnelling Through Multiple Quantum Barriers in Different Heterostructures. *arXiv Prepr. arXiv1002.1931* **2010**, 8.

(197) Lui, W. W.; Fukuma, M. Exact Solution of the Schrodinger Equation across an Arbitrary One-Dimensional Piecewise-Linear Potential Barrier. *J. Appl. Phys.* **1986**, *60* (5), 1555–1559.

(198) Ando, Y.; Itoh, T. Calculation of Transmission Tunneling Current across Arbitrary Potential Barriers. *J. Appl. Phys.* **1987**, *61* (4), 1497–1502.

(199) Chang, C. Y.; Sze, S. M. Carrier Transport across Metal-Semiconductor Barriers. *Solid. State. Electron.* **1970**, *13*, 727–740.

(200) Crowell, C. R. Richardson Constant And Tunneling Effective Mass For Thermionic And Thermionic-Field Emission In Schottky Barrier Diodes. *Solid. State. Electron.* **1969**, *12* (1), 55–59.

(201) Chasin, A.; Nag, M.; Bhoolokam, A.; Myny, K.; Steudel, S.; Schols, S.; Genoe, J.; Gielen, G.; Heremans, P. Gigahertz Operation of a-IGZO Schottky Diodes. *IEEE Trans. Electron Devices* **2013**, *60* (10), 3407–3412.

(202) *Metal-Semiconductor Schottky Barrier Junctions and Their Applications*; Sharma, B. L., Ed.; Springer Science & Business Media, 2013.

(203) Razeghi, M.; Rogalski, A. Semiconductor Ultraviolet Detectors. *J. Appl. Phys.* **1996**, *79* (10), 7433–7473.

(204) Newton, M. C.; Firth, S.; Warburton, P. a. Photoresponse of ZnO Tetrapod Nanocrystal Schottky Diodes. *IEEE Trans. Nanotechnol.* **2008**, *7* (1), 20–23.

(205) Oh, M.; Kim, S.; Seong, T.; Oh, M.; Kim, S.; Seong, T. Growth of Nominally Undoped P-Type ZnO on Si by Pulsed-Laser Deposition. *Appl. Phys. Lett.* **2005**, *87* (12), 122103.

(206) Norton, D. P. Synthesis and Properties of Epitaxial Electronic Oxide Thin-Film Materials. *Mater. Sci. Eng. R Reports* **2004**, *43* (5), 139–247.

(207) Ma, A. M.; Gupta, M.; Chowdhury, F. R.; Shen, M.; Bothe, K.; Shankar, K.; Tsui, Y.; Barlage, D. W. Zinc Oxide Thin Film Transistors with Schottky Source Barriers. *Solid. State. Electron.* **2012**, *76*, 104–108.

(208) Ma, A. M.; Shen, M.; Afshar, A.; Tsui, Y. Y.; Cadien, K. C.; Barlage, D. W. Interfacial Contact Effects in Top Gated Zinc Oxide Thin Film Transistors Grown by Atomic Layer Deposition. *IEEE Trans. Electron Devices* **2016**, *63* (9), 3540–3546.

(209) Albrecht, J.; Ruden, P. High Field Electron Transport Properties of Bulk ZnO. *J. Appl. Phys.* **1999**, *86* (12), 6864.

(210) Glassbrenner, C. J.; Slack, G. A. Thermal Conductivity of Silicon and Germanium from 3 K to the Melting Point. *Phys. Rev.* **1964**, *134*, A1058–A1069.

(211) Jacoboni, C.; Canali, C.; Otiaviani, G.; Quaranta, A. A. A Review of Some Charge Transport Properties of Silicon. *Solid. State. Electron.* **1977**, *20* (2), 77–89.

(212) Mion, C.; Muth, J. F.; Preble, E. a.; Hanser, D. Thermal Conductivity, Dislocation Density and GaN Device Design. *Superlattices Microstruct.* **2006**, *40* (4–6), 338–342.

(213) Tsukazaki, A.; Ohtomo, A.; Kawasaki, M. High-Mobility Electronic Transport in ZnO Thin Films. *Appl. Phys. Lett.* **2006**, *88* (15), 1–4.

(214) Michaelson, H. B. The Work Function of the Elements and Its Periodicity. *J. Appl. Phys.* **1977**, *48* (11), 4729–4733.

Appendix I. Schottky Diodes with ZnO Grown by PLD

Pulsed laser deposition (PLD) is one of the most widely used techniques for oxide thin film deposition with attractive features like generation of energetic species, hyperthermal reaction of the ablated cations with the oxygen molecular from the environment, stoichiometric transfer of target material composition, compatibility with a wide range of background pressures from ultra-high vacuum to 0.1 torr[19,205,206]. The PLD system is shown schematically in Figure Appx. I. 1 including a vacuum chamber equipped with pumps, a target holder and rotator, laser source, and substrate holder with an embedded heater underneath. The substrate is aligned normal to the target for the deposition of ZnO. The chamber is equipped with gauges to monitor ambient pressure and gas lines to control the background environment. In PLD processing, the pulsed laser beam is directed to the target surface with adjustable laser beam size assisted by a movable focusing lens. Plasma plume is then ejected which consists of atoms, ions, and molecules from the ablation. The energetic particles travel toward the substrates with a strong forward-directed velocity normal to the target surface, and condense onto the substrate placed opposite to the target.

Based on a previous study on ZnO growth by PLD in our group[109], the optimized growth conditions used are: the substrate surface was 3 cm away from the ZnO target surface with two surfaces oriented parallel to each other, the substrate was heated to 250 °C in a vacuum chamber with a background pressure of 10^{-5} torr which is backfilled with oxygen to a pressure maintained at 0.1 torr. The ZnO thin films were deposited by ablating a 99.9 % pure ceramic ZnO target using a KrF laser (248 nm, 15 ns, 20 Hz) with typical pulse energy of 50 mJ and laser fluence of 2.5 J/cm^2. High quality ZnO thin film with Hall mobility of 8 cm^{2}V^{-1}s^{-1} can be achieved on a

SiO_2 substrate. Typically, as-grown ZnO is intrinsically n-type conductivity due to the nature defects such as oxygen vacancies, zinc and hydrogen interstitials[28].

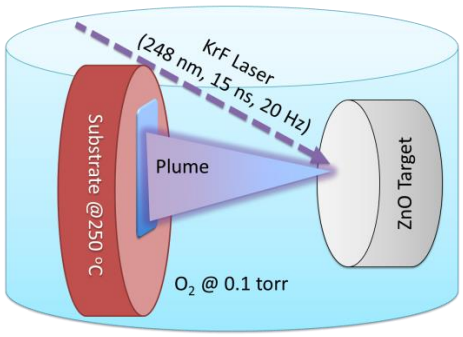

Figure Appx. I. 1. A schematic diagram of the alignment in PLD chamber.

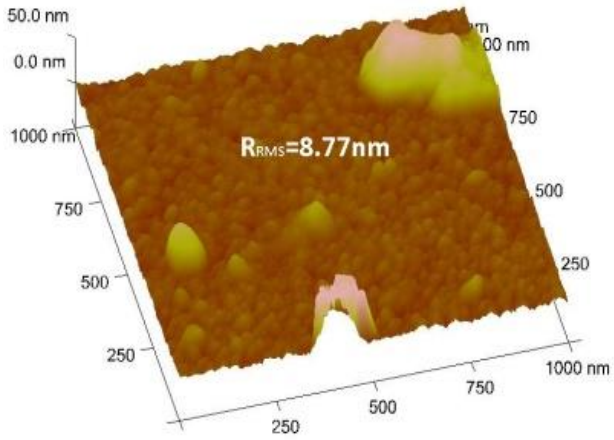

Figure Appx. I. 2. The AFM image for the PLD grown ZnO thin film.

The thickness of the film is targeted to be 30 nm although uniformity control is poor in our system. The deposited ZnO thin film surface morphology is characterized by AFM as shown in Figure Appx. I. 2. The root mean squared (RMS) roughness of 1 μm^2 area is 8.8 nm mainly due to the presence of debris particles in the film. A significantly smaller RMS roughness of 1.7 nm is achieved from a debris-free region of 0.25 μm^2 area of the same image. The PLD grown

ZnO shows larger size surface feature compared to those grown by ALD discussed above attributed to higher deposition temperature and energetic species in the deposition plume.

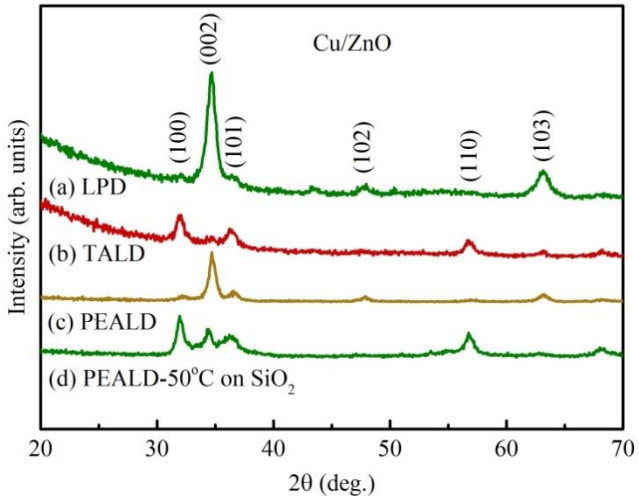

Figure Appx. I. 3. GAXRD profiles with ω=0.2°C of (a) 250°C PLD-ZnO film, (b) 200°C TALD-ZnO and (c) 200°C PEALD-ZnO film on Cu Substrates. (d) The GAXRD profile with ω=0.5°C for 50°C PEALD-ZnO film.

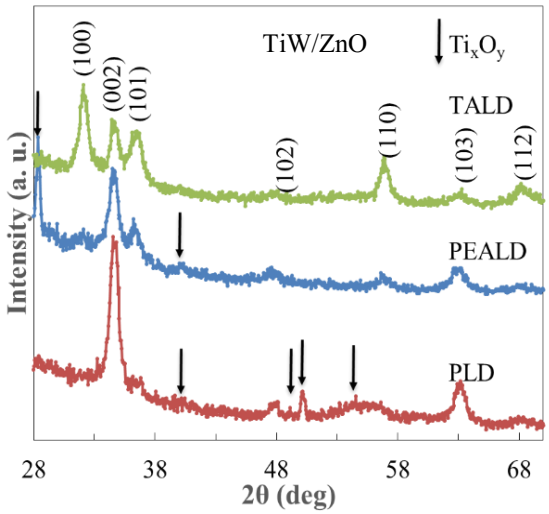

Figure Appx. I. 4. GAXRD profiles of ZnO thin film synthesized by TALD at 200 °C, PEALD at 200°C and PLD at 250°C. Titanium oxide (Ti_xO_y) phases were detected in both PLD-ZnO and PEALD-ZnO.

The PLD grown ZnO structural property is characterized by GAXRD as shown in Figure Appx. I. 3 and Figure Appx. I. 4 for PLD-Cu and PLD-TiW, respectively, compared to other

films discussed above. The peaks detected matches well with ZnO XRD profiles in the literature for all the samples, except some anonymous peaks from thin films on TiW substrates due to titanium oxide. The PLD film shows a strong dominating orientation of (002). It is noted that the Ti diffusion is enhanced significantly in ZnO growth at higher temperature.

The ZnO thin film composition is studied by XPS depth profile as shown in Figure Appx. I. 5. The PLD grown ZnO thin film shows a Zn-rich composition suggesting a high doping concentration in the film. The Cu substrate is less oxidized compared to that resultant from ALD processing. The high resolution oxygen XPS profile in ZnO thin film is also used to evaluate hydroxyl defects in the thin film. As shown in Figure Appx. I. 6, the hydroxyl component in PLD-ZnO is the same as that of PEALD.

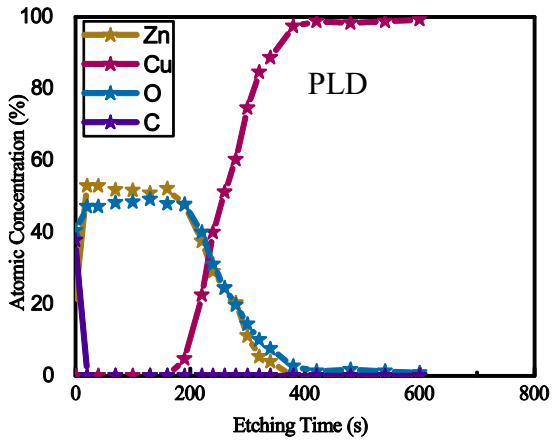

Figure Appx. I. 5. XPS depth profile of the ZnO thin film composition.

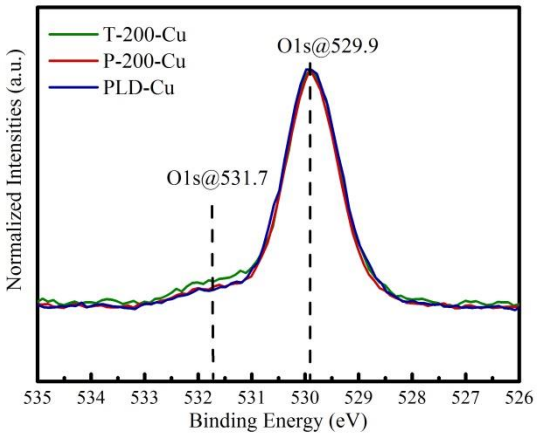

Figure Appx. I. 6. High resolution oxygen XPS profile in ZnO thin film.

After top electrode fabrication, primary results for Schottky nanodiode (SND) with PLD-ZnO are obtained and summarized in Table Appx. I. 1. The SNDs with bottom electrodes including Au, Ag, and Pt all exhibit linear *I-V* characteristics while TiW device show Schottky behavior but poor rectifying ratio as shown in Figure Appx. I. 7a compared to PEALD device with the same electrodes materials. The failure of Schottky barrier formation may be due to high deposition temperature and too thin active layers. Chemical reaction between the electrode and ZnO is promoted at high temperature. As to the thickness control, the deposition rate is hard to control due to some practical issues of the system. From the XPS depth profile, it is noticed that the PLD-ZnO on Cu is etched away faster than the ALD ones, indicating the film is much thinner leading to a high reverse current. As the *C-V* turns into negative quickly due to the low impedance of the device as shown in Figure Appx. I. 7b, the extraction of doping concentration from *C-V* becomes difficult. The results for PLD-ZnO on Cu and Ni electrode were inconclusive as fabrication failure occurred when underlying Cu layer was easy to be etched away with Al etchant quickly.

Table Appx. I. 1. Primary results for Schottky nanodiode with PLD-ZnO

Metal	PLD ZnO
Au	ohmic
Ag	ohmic
Pt	ohmic
TiW	Schottky
Cu	process failure
Ni	process failure

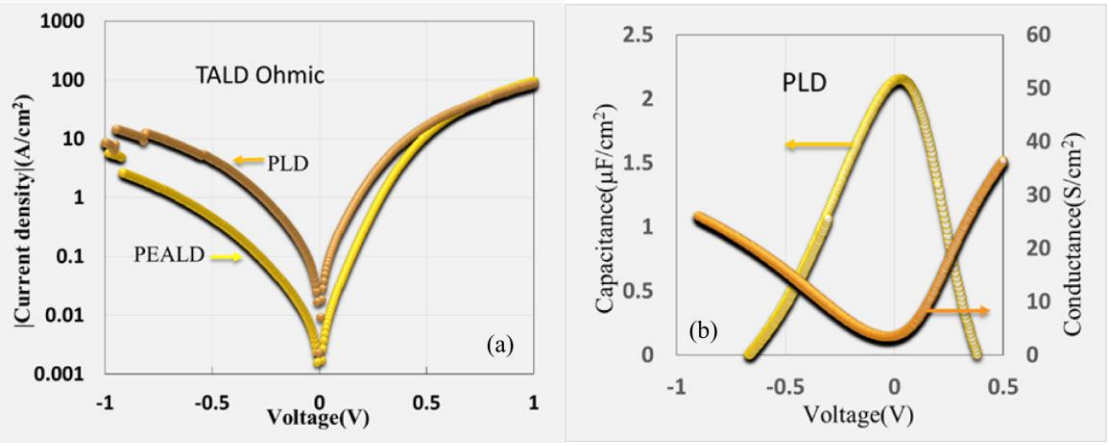

Figure Appx. I. 7. (a) Typical *I-V* characteristics of PEALD-ZnO and PLD-ZnO diodes with TiW bottom electrode. (b) Typical *C-V* characteristics for PLD-ZnO diode.

Appendix II. Utilization of Schottky Contact in SGTFT

ZnO based transparent thin film transistor (TFT) has attracted intensive research interests. A particular application of Schottky contact (SC) is to be a buried source contact in TALD ZnO based source-gated TFTs (SGTFTs)[207,208]. A schematic diagram of the SGTFT with T-130 ZnO thin films active layer is depicted in Figure Appx. II.1. The operating principle of the SGTFTs is that the carrier transport in the transistor is dominated by the electrostatics of the gate-controlled potential barrier at the source rather than by the carrier density of the channel between the source and drain like in conventional transistors. This SGTFT architecture has shown being less sensitivity to the crystalline quality of the ZnO thin film[43,207], which makes it compatible with low temperature ZnO grown and particularly attractive for building TFT back panel matrix for transparent and flexible electronics.

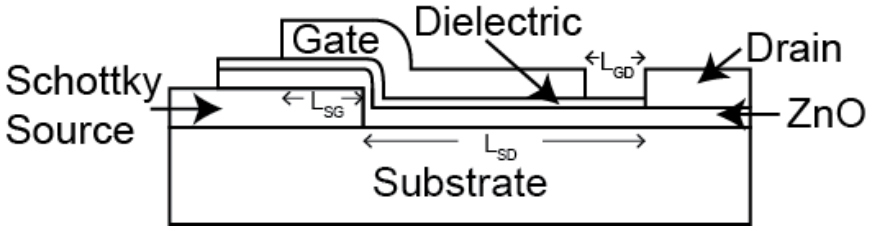

Figure Appx. II. 1. A schematic diagram of the SGTFT.

The Studies of SGTFTs carried out in our group has shown that the formation of SC with source metal electrodes plays significant roles in the *I-V* characteristics of the SGTFTs[207,208]. The family curves of the SGTFT with TiW SC are shown in Figure Appx. II. 2, compared to that of a SGTFT having ZnO active layer grown under same deposition condition but without SC. The former one shows better control of current transport in the TFT than the latter one, indicating the important role of SC in realization of current control in TFTs with poor crystalline ZnO active layer.

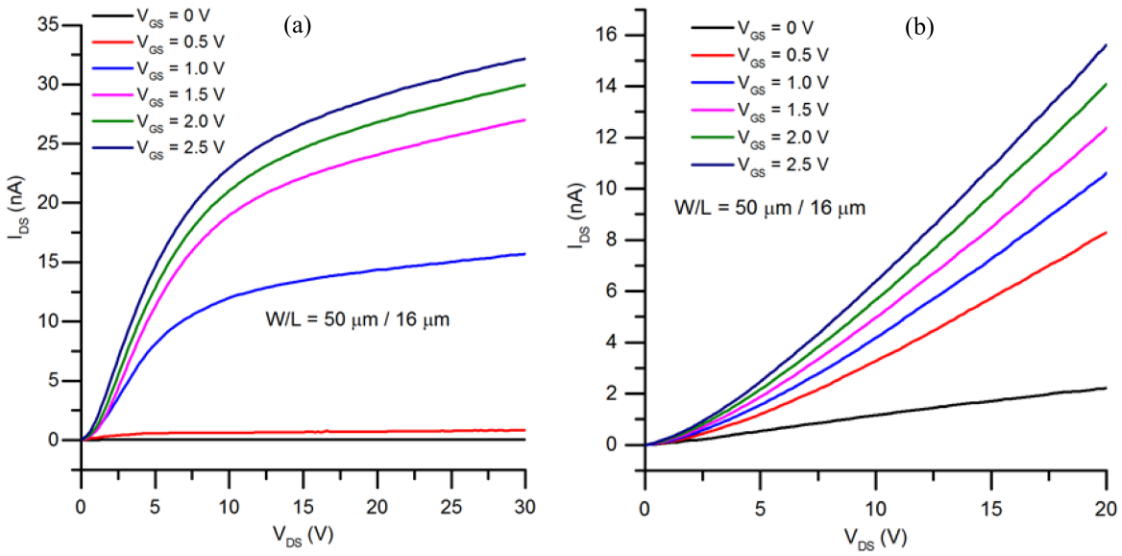

Figure Appx. II. 2. (a) Output characteristics of SGTFT with TiW SC; (b) Output characteristics of SGTFT without SC.